Investigation of Reactive Transport and Coupled THMC Processes in the EBS: FY13 Report

Fuel Cycle Research & Development

Prepared for
U.S. Department of Energy
Used Fuel Disposition
James Davis, Jonny Rutqvist,
Carl Steefel, Ruth Tinnacher,
Victor Vilarrasa, Liange Zheng,
Ian Bourg, Hui-Hai Liu, Jens Birkholzer
Lawrence Berkeley National Laboratory

July 2013
FCRD-UFD-2013-000216

DISCLAIMER

This information was prepared as an account of work sponsored by an agency of the U.S. Government. Neither the U.S. Government nor any agency thereof, nor any of their employees, makes any warranty, expressed or implied, or assumes any legal liability or responsibility for the accuracy, completeness, or usefulness, of any information, apparatus, product, or process disclosed, or represents that its use would not infringe privately owned rights. References herein to any specific commercial product, process, or service by trade name, trade mark, manufacturer, or otherwise, does not necessarily constitute or imply its endorsement, recommendation, or favoring by the U.S. Government or any agency thereof. The views and opinions of authors expressed herein do not necessarily state or reflect those of the U.S. Government or any agency thereof.

Revision 2
12/20/2012

APPENDIX E

FCT DOCUMENT COVER SHEET [1]

Name/Title of Deliverable/Milestone/Revision No.	Investigation of reactive transport and coupled THMC processes in EBS: FY13 report
Work Package Title and Number	DR Generic Engineered Barrier Systems Evaluations – LBNL FT-13LB080604
Work Package WBS Number	1.02.08.06
Responsible Work Package Manager	Hui-Hai Liu (Name/Signature)

Date Submitted 7/16/2013

Quality Rigor Level for Deliverable/Milestone[2]	☐ QRL-3	☐ QRL-2	☐ QRL-1 ☐ Nuclear Data	☒ Lab/Participant QA Program (no additional FCT QA requirements)

This deliverable was prepared in accordance with Lawrence Berkeley National Laboratory
(Participant/National Laboratory Name)

QA program which meets the requirements of
☒ DOE Order 414.1 ☐ NQA-1-2000 ☐ Other

This Deliverable was subjected to:

☐ Technical Review ☐ Peer Review

Technical Review (TR)

Review Documentation Provided

☐ Signed TR Report or,
☐ Signed TR Concurrence Sheet or,
☐ Signature of TR Reviewer(s) below

Peer Review (PR)

Review Documentation Provided

☐ Signed PR Report or,
☐ Signed PR Concurrence Sheet or,
☐ Signature of PR Reviewer(s) below

Name and Signature of Reviewers

NOTE 1: *Appendix E should be filled out and submitted with the deliverable. Or, if the PICS:NE system permits, completely enter all applicable information in the PICS:NE Deliverable Form. The requirement is to ensure that all applicable information is entered either in the PICS:NE system or by using the FCT Document Cover Sheet.*

NOTE 2: *In some cases there may be a milestone where an item is being fabricated, maintenance is being performed on a facility, or a document is being issued through a formal document control process where it specifically calls out a formal review of the document. In these cases, documentation (e.g., inspection report, maintenance request, work planning package documentation or the documented review of the issued document through the document control process) of the completion of the activity along with the Document Cover Sheet is sufficient to demonstrate achieving the milestone. If QRL 1, 2, or 3 is not assigned, then the Lab/Participant QA Program (no additional FCT QA requirements box must be checked, and the work is understood to be performed, and any deliverable developed, in conformance with the respective National Laboratory/Participant, DOE- or NNSA-approved QA Program..*

This page is intentionally blank.

CONTENTS

ACRONYMS xi

1. INTRODUCTION 1

2. MODELING COUPLED THMC PROCESSES IN THE EBS 1
   - 2.1 Implementation and testing of a Dual-Structure Bentonite Model into TOUGH-FLAC 3
     - 2.1.1 The dual-structure approach and Barcelona Expansive Model 3
     - 2.1.2 Implementation of BExM into TOUGH-FLAC 9
     - 2.1.3 Testing and verification of implementation 10
   - 2.2 Linking dual-structure model to chemistry and testing 14
   - 2.3 Summary 17

3. MODELING REACTIVE DIFFUSIVE TRANSPORT 17
   - 3.1 Mean Electrostatic Model for Diffusive Transport in the EBS 20
     - 3.1.1 Derivation from Poisson-Boltzmann Equation 20
     - 3.1.2 Dynamic Calculation of Electrical Double Layer Thickness 23
     - 3.1.3 Testing of EDL Model using the DR-A Experiment at Mont Terri, Switzerland 25
     - 3.1.4 Development of a CrunchEDL-Comsol Coupling for Flow and Transport in Charged Porous Media 27
   - 3.2 Molecular scale predictions of diffusion in the EBS 28
     - 3.2.1 Temperature Dependence of Water and Solute Diffusion in the EBS 28
     - 3.2.2 Methodology 30
     - 3.2.3 Results and Discussion 32
     - 3.2.4 Summary 40

4. EXPERIMENTAL STUDIES ON REACTIVE DIFFUSIVE TRANSPORT 41
   - 4.1 Background 41
     - 4.1.1 Relevance 41
     - 4.1.2 Effects of Chemical Solution Conditions on U(VI) Diffusion Coefficients 42
     - 4.1.3 Influence of Solution Chemistry on Clay (Surface) Properties 45
   - 4.2 Materials and Methods 47
     - 4.2.1 Overview of Materials 48
     - 4.2.2 Batch Sorption Equilibrium Experiments 48
     - 4.2.3 Modeling Setup for Surface Complexation Models 49
     - 4.2.4 Design of Diffusion Cell and Clay Packing Device 49
     - 4.2.5 Clay Pretreatment Specific to Diffusion Experiments 52
     - 4.2.6 Diffusion Experiment: Calcium Bromide Diffusion in Na-Montmorillonite 53
     - 4.2.7 Predictive Modeling of Uranium(VI) Diffusion in Lab-Scale Experiments 54
   - 4.3 Results and Discussion 57
     - 4.3.1 Batch sorption equilibrium experiments and surface complexation modeling 57
     - 4.3.2 Calcium Bromide Diffusion in Na-Montmorillonite 63
     - 4.3.3 Predictive Modeling of Uranium(VI) Diffusion in Lab-Scale Experiments 70

4.4 Summary 74

5. OVERALL SUMMARY 74
5.1 THMC Process Modeling in Bentonite 74
5.2 Modeling Reactive-Diffusive Transport in Bentonite 75
5.3 Experimental Study on Reactive-Diffusive Transport 76

6. REFERENCES 78

FIGURES

Figure 2.1. Schematic representation of the two structural levels considered (Sánchez et al., 2005). 3

Figure 2.2. Three-dimensional representation of the yield surface in the BBM (Gens et al. 2006). 5

Figure 2.3. Microstructural and macrostructural elastoplastic responses in a double-structure model equivalent to the Barcelona Expansive Model. 6

Figure 2.4. Summary of micro–macropore interaction mechanisms. 7

Figure 2.5. Reference pressure and plastic flow direction (Sánchez et al. 2005). 9

Figure 2.6. Strain evolution during suction cycles for a low confining pressure. 11

Figure 2.7. Evolution of the interaction functions for a low confining pressure. 11

Figure 2.8. Evolution of the plastic strain due to the interaction between the microstructure and the macrostructure for a low confining pressure. 12

Figure 2.9. Void ratio evolution of the microstructure during suction changes for a low confining pressure. 12

Figure 2.10. Void ratio evolution of the macrostructure during suction changes for a low confining pressure. 12

Figure 2.11. Strain evolution during suction cycles for a high confining pressure. 13

Figure 2.12. Volumetric deformation upon suction cycles reported by Pousada (1984) in an oedometric test under a vertical stress of 0.1 MPa. 13

Figure 2.13. Volumetric deformation upon suction cycles mimicking the test of Pousada (1984). 13

Figure 2.14. Changes in water saturation in the middle of the sample (sample is hydrated from the bottom). 16

Figure 2.15. Changes in equivalent fraction of each cation in the middle of the sample when the sample is saturated with 1M $CaCl_2$ solution. 16

Figure 2.16. Changes in equivalent fraction of each cation in the middle of the sample when the sample is saturated with 1M NaCl solution. 16

Figure 2.17. Volumetric deformation in the middle of the sample for the case with 1 M NaCl and $CaCl_2$ solution. 17

Figure 3.1. Schematic illustration of the Gouy-Chapman-Stern model of the solid-electrolyte interface, with the potential distribution $\psi(z)$ versus distance from the charged solid surface. The solid is illustrated with a negative surface potential ψ_s, described by three

layers in solution. The inner Helmholtz plane layer ψ_i consists of nonhydrated co-ions and counterions (inner sphere complexes), whereas the outer Helmholtz plane layer ψ_d is built up of only hydrated counterions (outer sphere complexes). The diffuse layer is defined beyond the outer Helmholtz plane (from Schoch et al., 2008). 21

Figure 3.2. Schematic representation of the potential distribution in a nanochannel with height *h* in direction *z* when the EDLs overlap (solid line), compared to the EDL potentials if the opposite wall is not present (dashed line). From Schoch et al. (2008). 23

Figure 3.3. Results of dynamic EDL porosity calculations after 5 days of diffusion. Left panel: A high ionic strength front (I=0.45M) diffuses front left to right through the domain that is initially lower ionic strength (I=0.045M). The left boundary is a Dirichlet boundary condition, while the right boundary is no-flux. Right panel: Spatial profiles for bulk porosity and EDL porosity for the case of a constant total porosity of 4%. 24

Figure 3.4. Stratigraphic section of the Jura Mountains in which the Mont Terri rock laboratory is located. 25

Figure 3.5. Schematic of the experimental setup from the DI-A test, similar in concept to the DR-A test. 26

Figure 3.6. Fit of borehole HTO concentration versus time using a capacity factor of 2.175. This is solved in radially symmetric cylindrical coordinates using CrunchEDL. 27

Figure 3.7. Anion concentration versus time in the borehole for the first DR-A test. 27

Figure 3.8. Illustration of the coupling scheme between Comsol and CrunchEDL. 28

Figure 3.9. *D* values of Na^+ (top) and water (bottom) as a function of inverse simulation cell size (for simulations with 512, 8334, or 22224 water molecules) at different temperatures. The size-corrected diffusion coefficient $D_{0,s}$ is determined by linear regression (black line) to $1/L = 0$. The dashed line shows the best fit obtained with Eq. (3.17) using the viscosity of SPC/E water. 33

Figure 3.10. Comparison of the shear viscosity of the SPC/E water model, from this study (white circles) and from Medina et al. (2011) (gray circles), with the experimental viscosity of water (Lide, 2012) (black line). Right hand axis indicates our simulated (white squares) and the experimental (gray line) water density, respectively. 33

Figure 3.11. Basal spacing d_{001} (open circles) and interlayer water density (filled circles) as a function of the number of water molecules per unit cell (UC) in a MD simulation where the number of water molecules was slowly decreased by removing one water molecule every 40 ps (NP_zT ensemble). Experimental data on the d_{001}-values of the 1W, 2W, 3W, and 4W hydrate states of montmorillonite (Holmboe et al., 2012) are shown as black horizontal arrows. The precision of predicted d_{001} values is roughly 0.1 Å. Black crosses show the d_{001} values predicted from NP_zT ensemble simulations with 12, 15, or 18 water molecules per unit cell at $T = 278$ to 353 K. 35

Figure 3.12. MD simulation snapshots showing the four different simulation cells that were used to study the 3W hydrate of montmorillonite. From left to right, the systems contained 61680, 16962, 7710 and 1285 atoms and {18×10×4}, {11×6×3}, {9×5×2} and {5×3×1} unit cells in the {*a*×*b*×*c*} directions, respectively. 36

Figure 3.13. *D* values of Na^+ (top) and water (bottom) as a function of temperature and the mean inverse simulation cell size $1/L$. 36

Figure 3.14. MD simulation snapshots showing the 1W, 2W, 3W and the 10W hydration states (with d_{001} = 12.4, 15.6, 18.8, and 40.7 Å, respectively) at 298 K and the corresponding atomic density profiles along z-direction for Na^+ (blue), H_{water} (light gray), O_{water} (red) and montmorillonite (black). 38

Figure 3.15. Normalized self-diffusion coefficients of Na^+ (left) and water (right) as a function of clay layer rigidity and hydration state (1W, 2W, 3W, or 10W) at 298 K. The normalization of D was made with regard to the corresponding size corrected $D_{0,s}$ value from Table 3.2. The clay layer rigidity was varied from fully rigid (red squares) to fully flexible (yellow circles). In the two semi-flexible states, either all structural clay atoms were kept fixed except the bonded hydroxyl hydrogen (green diamonds) or vice versa (blue triangles). 38

Figure 4.1. Expected gradients across the EBS. 42

Figure 4.2. Visualization of constrictivity and tortuosity (Van Loon and Soler, 2004). 44

Figure 4.3. Overview of chemical solution effects on clay (surface) characteristics and diffusion rates. 46

Figure 4.4. Visualization of anion exclusion effects (Van Loon & Soler, 2004). 47

Figure 4.5. Diffusion cell design. 51

Figure 4.6. Design for clay packing device. 51

Figure 4.7. Diffusion cell and clay packing device. 52

Figure 4.8. Schematic of setup for diffusion experiment (Courtesy of M. Holmboe; modified). 53

Figure 4.9. Schematic of diffusion cell, containing a clay packing sandwiched between two filter plates, used in ANADIFF simulations (Eriksen and Jansson, 1996). 55

Figure 4.10. U(VI) adsorption onto Na-montmorillonite at varying chemical solution conditions. 58

Figure 4.11. K_d values for U(VI) sorption to Na-montmorillonite at varying chem. solution conditions. 59

Figure 4.12. Total, measured Ca concentrations in solution for batch sorption equilibrium experiments. 60

Figure 4.15. Modeling results for U(VI) sorption onto Na-montmorillonite over the whole pH range. 62

Figure 4.16. Detailed modeling results for U(VI) sorption onto Na-montmorillonite between pH values of 5.5 and 8.5. 62

Figure 4.17. Results for monitoring of solution pH in low-concentration reservoir solutions during $CaBr_2$ diffusion experiment. 63

Figure 4.18. Results for monitoring of Ca and Br concentrations in high-concentration reservoir solution during $CaBr_2$ diffusion experiment. Error bars for Ca data represent standard deviations of replicate ICP-MS analysis of the same samples; error bars for Br data are standard deviations for replicate injections during ICP-MS analysis of the same samples. 64

Figure 4.19. Diffusive flux of Ca through pretreated Na-montmorillonite as a function of time in $CaBr_2$ through-diffusion experiment at 1 mM $CaBr_2$, I=0.1 M NaCl and pH~7. Steady-state conditions are approximately reached at 32.97 days. 66

Figure 4.20. Cumulative mass of Ca as a function of time in $CaBr_2$ through-diffusion experiment in pretreated Na-montmorillonite at 1 mM $CaBr_2$, I=0.1 M NaCl and pH~7. Data points shown as dots are assumed to be under steady-state conditions and are used for the fitting of the asymptote to calculate diffusion parameters (see text for details). 66

Figure 4.21. Diffusive flux of Br through pretreated Na-montmorillonite as a function of time in $CaBr_2$ through-diffusion experiment at 1 mM $CaBr_2$, I=0.1 M NaCl and pH~7. Steady-state conditions are most likely reached after a few days. 67

Figure 4.22. Cumulative mass of Br as a function of time in $CaBr_2$ through-diffusion experiment in pretreated Na-montmorillonite at 1 mM $CaBr_2$, I=0.1 M NaCl and pH~7. Data points shown as dots are assumed to be under steady-state conditions and are used for the fitting of the asymptote to calculate diffusion parameters (see text for details). 67

Figure 4.23. Diffusive flux of tritium through pretreated Na-montmorillonite as a function of time in $CaBr_2$ through-diffusion experiment at I=0.1 M NaCl and pH~7. Steady-state conditions are most likely reached after 1-2 days. 68

Figure 4.24. Cumulative activity of tritium as a function of time in $CaBr_2$ through-diffusion experiment in pretreated Na-montmorillonite at I=0.1 M NaCl and pH~7. Data points shown as dots are assumed to be under steady-state conditions and are used for the fitting of the asymptote to calculate diffusion parameters (see text for details). Tracer experiment is currently still ongoing in order to collect a larger number of data points under steady state conditions. 68

Figure 4.25. Simulated diffusion profiles: Total U(VI) conc. along a clay packing as a function of Total Inorganic Carbon (TIC) conc. and time. 72

Figure 4.26. Simulated diffusion profiles: Total U(VI) concentrations along a clay packing as a function of solution pH and time. 72

Figure 4.27. Simulated relative U(VI) solution concentrations as a function of Total Inorganic Carbon (TIC) concentrations and pH after a 360-day experiment. 73

TABLES

Table 2.1. Parameters used to reproduce the suction cycles test of Pousada (1984). 14

Table 3.1. Parameters for DR-A test 26

Table 3.2. Shear viscosity of water and self-diffusion coefficients of Na^+ and water in bulk liquid water. Predicted D values are shown for simulations with 512 water molecules (D), after correction for the finite-size effect ($D_{0,s}$), and after correction for both size and viscosity ($D_{0,sv}$). The subscript 'exp' denotes experimental values (Talekar, 1977; Holz et al., 2000). 34

Table 3.3. Two-dimensional self-diffusion coefficients of Na^+ and water in clay interlayer nanopores in systems with fully flexible clay sheets and five H_2O molecules per unit cell per hydrate layer. The last column shows the correction factor that can be applied to account for the discrepancy between measured and predicted diffusion coefficients in bulk liquid water. The last row shows the E_a values of Na^+ and water in the clay interlayer nanopores at different hydration states, corrected for the difference in E_a values between bulk liquid SPC/E water and real water. 39

Table 4.1. Effects of solution chemistry on diffusion coefficients 43

Table 4.2. Overview of variable model input parameters 57
Table 4.3. Constant model input parameters 57
Table 4.4. Summary of U(VI) adsorption data in batch sorption envelope experiments 59
Table 4.5. Overview of uranium(VI) surface reactions in surface complexation model 61
Table 4.6. Parameters determined in $CaBr_2$ diffusion experiment 70

ACRONYMS

BBM	Barcelona Basic Model
BExM	Barcelona Expansive Model
CEC	cation exchange capacity
EBS	engineered barrier system
EDZ	Excavation Disturbed Zone
EDL	electrical double layer
FEPs	Features, Events and Processes
HLRW	high-level radioactive waste
LC	loading-collapse
MC	microstructural contraction
MD	molecular dynamics
NBS	natural barrier system
NL	Neutral Line
PA	performance assessment
PB	Poisson-Boltzmann
SCMs	surface complexation models
THMC	thermal-hydrological-mechanical-chemical
TIC	Total Inorganic Carbon
UFD	Used Fuel Disposition
UDM	User Defined constitutive Model

This page is intentionally blank.

1. INTRODUCTION

Geological repositories for disposal of high-level nuclear waste generally rely on a multibarrier system to isolate radioactive waste from the biosphere. The multi-barrier system typically consists of the natural barrier system (NBS), which includes the repository host rock and its surrounding subsurface environment, and the engineered barrier system (EBS). The EBS represents the man-made, engineered materials placed within a repository, including the waste form, waste canisters, buffer materials, backfill, and seals (OECD, 2003). The EBS plays a significant role in the containment and long-term retardation of radionuclide release.

During the lifespan of a geologic repository, the performance of the EBS is affected by complex thermal, hydrogeological, mechanical, chemical and biological processes, such as heat release due to radionuclide decay, multiphase flow (including gas release due to canister corrosion), swelling of buffer materials, radionuclide diffusive transport, waste dissolution, and chemical reactions. All these processes are related to each other. An in-depth understanding of these coupled processes is critical for the performance assessment (PA) of an EBS and the entire repository. Within the EBS work package of the Used Fuel Disposition (UFD) Campaign, LBNL's research is currently focused on two relevant areas, namely (1) the thermal-hydrological-mechanical-chemical (THMC) processes in buffer materials (bentonite), and (2) the diffusive transport in the EBS associated with clay host rock, with the long-term goal of developing a full understanding of (and verified modeling capabilities to simulate) the impact of coupled processes on radionuclide transport in different components of the EBS, as well as the interaction between the EBS components and the near-field host rock (e.g., clay/shale)—and how these processes affect radionuclide release.

LBNL's focus areas address key Features, Events and Processes (FEPs), which have been ranked in importance from medium to high, as listed in Tables 7 and 8 of the *Used Fuel Disposition Campaign Disposal Research and Development Roadmap* (FCR&D-USED-2011-000065 REV0) (Nutt, 2011). Specifically, they address FEP 2.2.01, Excavation Disturbed Zone (EDZ) for shale by investigating the effects of coupled processes on interactions between shale (clay) disposal formations and the EBS; FEP 2.1.04.01, Buffer/Backfill; FEPs 2.1.07.02, 03, 04, 09, Mechanical Processes; FEPs 2.1.08.03, 07, 08, Hydrologic Processes; and FEP 2.1.11.04, Thermal Processes, by studying coupled processes in the EBS; and FEPs 2.1.09.52, 53, 54, Chemical Processes—Transport, by investigating reactive-diffusive radionuclide transport in bentonite.

This report documents the progress that LBNL has made in its two R&D focus areas in FY13. Section 2 presents the modeling results of THMC processes within bentonite and the interaction between the EBS and a clay disposal formation in the near field. Section 3 documents the development of reactive-diffusive transport modeling approaches for radionuclide migration in bentonite. Section 4 reports on experimental studies of reactive diffusive transport of U(VI) in bentonite. Work activities in the remaining months of FY13 and proposed activities in FY14 are presented in Section 5.

2. MODELING COUPLED THMC PROCESSES IN THE EBS

The long-term chemical and mechanical stability of protective bentonite buffers and tunnel backfill is a key issue in the long-term performance of backfilled, multiple barrier nuclear waste repositories. For example, a certain swelling pressure should be maintained to keep the buffer homogenous, to prevent canister sinking, to prevent the adverse effect of external rock shear movements, to limit colloid transport, and to prevent the buffer from being a preferred pathway of radionuclide transport. The long-term stability of the buffer is governed by coupled thermal-hydrological-mechanical and chemical (THMC) processes. These coupled THMC processes can be simulated by numerical modeling, e.g., by a coupling of LBNL's TOUGHREACT reactive transport simulator to a geomechanical code such as FLAC3D.

However, this requires appropriate constitutive models describing couplings between the different processes.

In this section, we describe our ongoing work on developing and applications of such models for the analysis of EBS coupled processes. As part of the UFD Campaign, we have previously implemented the Barcelona Basic Model (BBM) into the TOUGH-FLAC simulator and we have conducted model simulations related to a generic repository involving a bentonite-backfilled repository tunnel hosted in a clay formation, with properties corresponding to the Opalinus Clay. We also recently coupled TOUGHREACT and FLAC3D for the modeling of coupled THMC processes in the EBS, using a simplified approach for the modeling of mechanical-chemical (MC) coupling in bentonite. This development and the results were summarized in a peer-reviewed journal article entitled "Modeling of Coupled Thermo-Hydro-Mechanical Processes with Links to Geochemistry Associated with Bentonite-Backfilled Repository Tunnels in Clay Formations", which was published online in Rock Mechanics and Rock Engineering in March 2013 (Rutqvist et al. 2013).

The THM modeling results summarized in the paper showed strong THM-driven interactions between the bentonite buffer and the low-permeability host rock. It was shown that the resaturation of the buffer is delayed as a result of the low rock permeability, and the fluid pressure in the host rock is strongly coupled with the temperature changes, which under certain circumstances could result in a significant increase in pore pressure. Moreover, using the BBM, the bentonite buffer was found to have a rather complex geomechanical behavior that eventually leads to a slightly non-uniform density distribution. Nevertheless, the simulation showed that the swelling of the buffer is functioning to provide an adequate increase in confining stress on the tunnel wall, leading to a stabilization of any failure that may occur during the tunnel excavation. Finally, we described the application of a possible approach for linking THM processes with chemistry, focusing on the evolution of primary and secondary swelling, in which the secondary swelling is caused by changes in ionic concentration, which in turn is evaluated using a transport simulation model. This is a simplified approach for modeling of the MC coupling related to benonite swelling and we applied this approach for simulating the effects of salt concentration on the swelling stress.

In FY2013, we have made significant progress in the implementation and testing of a dual-structure model for expansive clay into TOUGH-FLAC, and we have made the first link of this model to reactive chemistry through TOUGHREACT-FLAC coupling. In a dual-structure model, the material consists of two structural levels: a microstructure in which the interactions occur at the particle level, and a macrostructure that accounts for the overall fabric arrangement of the material comprising aggregates and macropores (Figure 2.1) (Gens et al., 2006, Sánchez et al., 2005, Gens and Alonso, 1992). A dual-structure model has important features for modeling the mechanical behavior of a bentonite buffer, such as irreversible strain during suction cycles. However, most importantly, a dual-structure model provides the necessary link between chemistry and mechanics, enabling us to develop a fully coupled THMC model for the analysis of long-term EBS behavior. The dual-structure (or double-structure) model approach is especially useful when trying to incorporate the effects of chemical variables on the mechanical behavior of expansive clays. Because they contain large amounts of active clay minerals, those materials are especially susceptible to changes in the geochemical environment. Thus, the double structure model can provided the link between mechanical and chemical processes modeling, which enables mechanistic modeling of processes important for long-term buffer stability, including effects of pore water salinity on swelling (loss of swelling), conversion of smectite to non-expansive mineral forms (loss of swelling), and swelling pressure vs exchangeable cations. We first linked chemistry to the bentonite mechanics through the dual-structure model using an approach suggested by Gens (2010), in which some of the parameters related to the swelling micro-structure depend on the concentration of each exchangeable cation, and demonstrated this approach by modeling a swelling experiment. Moreover, we are currently working on a second more rigorous approach, linking chemistry to mechanics through the micro-structure strain, where the micro-structural strain is calculated using diffuse-double layer theory.

2.1 Implementation and testing of a Dual-Structure Bentonite Model into TOUGH-FLAC

In this section, we present the development and implementation of a dual-structure material model of expansive clay into TOUGH-FLAC. We first present an overview of the basic equations in the dual-structure model following (in part) the developments by Alonso et al. (1999) and Sánchez et al. (2005). We then summarize the implementation of this model into TOUGH-FLAC.

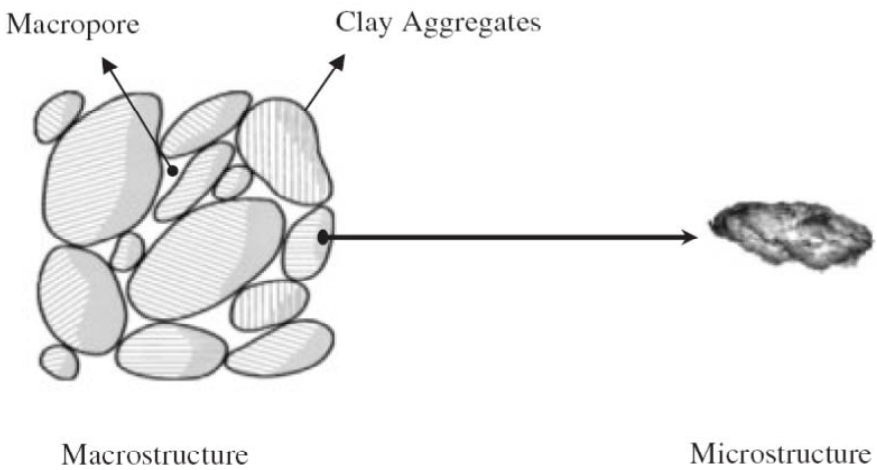

Figure 2.1. Schematic representation of the two structural levels considered (Sánchez et al., 2005).

2.1.1 The dual-structure approach and Barcelona Expansive Model

Sections 2.1.1 and 2.1.2 have been updated from the corresponding sections of last year's report (Rutqvist et al. 2012). These sections have been included here to explain the progress made in the implementation of the Barcelona Expansive Model (BExM) and because the information is needed to understand the subsequent material that follows in Sections 2.1.3 and 2.2. Alonso et al. (1999), in their presentation of the BExM, provide a suitable mathematical formulation for implementation of a dual-structure model into TOUGH-FLAC. Sánchez et al. (2005) provide another comprehensive description and mathematical formulation in terms of generalized elastoplasticity and implementation into a finite element code. The implementation of the BExM into TOUGH-FLAC is done as an extension of the existing TOUGH-FLAC implementation of the BBM, adding the microstructural level. The BBM model can describe many typical features of unsaturated-soil mechanical behavior, including wetting-induced swelling or collapse strains, depending on the magnitude of applied stress, as well as the increase in shear strength and apparent preconsolidation stress with suction (Gens et al., 2006). The extension to dual-structure behavior enables modeling of more expansive soils, including dependency of swelling strains and swelling pressures on the initial state and on the stress path, strain accumulation upon suction cycles, as well as secondary swelling. It is believed that such behavioral features are mainly related to the existence of coupled chemo-hydro-mechanical phenomena between distinct levels of structure within the material (Alonso et al., 1999).

Conceptually, in a dual-structure model, as described by Alonso et al. (1999) and Sánchez et al. (2005), the total volume, V, of the material consists of the solid phase, V_s, the microstructural voids V_{vm}, and the macrostructure voids V_{vM}:

$$V = V_s + V_{vm} + V_{vM} = V_m + V_{vM} \tag{2.1}$$

with the total void ratio and porosity being the sum of microstructural and macrostructural components according to

$$e = \frac{V_v}{V_s} = \frac{V_{vM}}{V_s} + \frac{V_{vm}}{V_s} = e_M + e_m, \tag{2.2}$$

$$\phi = \frac{V_v}{V} = \frac{V_{vM}}{V} + \frac{V_{vm}}{V} = \phi_M + \phi_m. \tag{2.3}$$

The microstructure can swell to invade the macroporosity, depending on the mechanical confinement and load level. This is relevant when considering permeability changes during bentonite swelling, because fluid movement takes place through the macroporosity, which is not proportional to the total strain and deformation of the bentonite.

Macrostructural level

The macrostructural behavior is modeled based on the BBM, in which the mechanical behavior depends on a three-dimensional yield surface in *p*-*q*-*s* space (Figure 2.2), where *p* is net mean stress (i.e., total stress minus gas-phase pressure), *q* is deviatoric stress (or shear stress), and *s* is suction. The size of the elastic domain increases as suction increases. The rate of increase, represented by the loading-collapse (LC) curve, is one of the fundamental characteristics of the BBM (Gens et al., 2006).

The suction-dependent loading collapse (LC) yield surface (Figure 2.2) bounds the elastic region according to

$$f_{LC} = \frac{q^2}{g_y(\theta)^2} - \frac{M^2}{g_y(\theta = 0)^2}(p + p_s)(p_0 - p) = 0 \tag{2.4}$$

where θ is the Lode's angle and the function $g_y(\theta)$ describes the shape of the yield surface in the deviatoric plane, M is the constant slope of the critical state line (Figure 2.2), whereas p_s represents the increase in cohesion with suction and the function

$$p_0 = p^c \left(\frac{p_0^*}{p^c} \right)^{[\lambda_{Ps0} - \kappa_{Ps0}]/[\lambda_{Ps} - \kappa_{Ps0}]} \tag{2.5}$$

is the net mean yield stress (or apparent pre-consolidation stress) at current suction, where p_0^* is the net mean yield stress (or pre-consolidation stress) at full saturation, where p^c is a reference stress, λ_{Ps0} is a compressibility parameter in virgin soil states at zero suction, $\lambda_{Ps} = \lambda_{Ps0}[(1-r)\exp(-\xi s) + r]$ is a compressibility parameter in virgin soil states at suction s, r is a constant related to the maximum stiffness of the soil (for an infinite suction), ξ is a parameter that controls the rate of increase of soil stiffness with suction and κ_{Ps0} is the elastic stiffness parameter for changes in net mean stress at zero suction.

The flow rule is given by

$$g_{LC} = \frac{\alpha_a q^2}{g_y(\theta)^2} - \frac{M^2}{g_y(\theta = 0)^2}(p + p_s)(p_0 - p) \tag{2.6}$$

where α_a is a parameter that gives rise to the non-associative model, i.e., $g_{LC} \neq f_{LC}$.

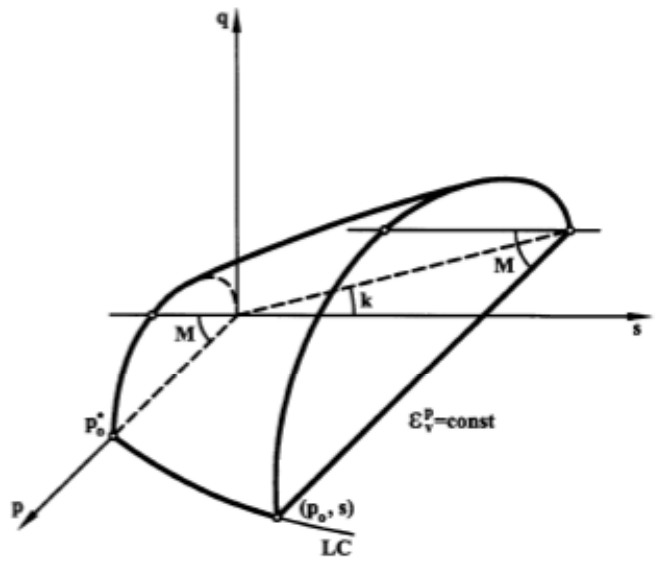

Figure 2.2. Three-dimensional representation of the yield surface in the BBM (Gens et al. 2006).

Microstructural level

In the BExM, the following assumptions are adopted related to microstructural behavior and its interaction with the macrostructure:

- The microstructure is mainly saturated and the effective stress concept holds.
- The microstructural behavior is elastic and volumetric.
- Mechanical, hydraulic, and chemical equilibrium exists between microstructure and macrostructure.
- Coupling between microstructure and macrostructure results in a possible buildup of macrostructural elastoplastic strains when elastic microstructural strains occur.

With these assumptions, the increment of volumetric microstructural strain increment $\mathrm{d}\varepsilon_{vm}^{e}$ depends exclusively on the increment of mean effective stress $\mathrm{d}\hat{p} = \mathrm{d}(\overline{p} - p_l) = \mathrm{d}(\overline{p} - p_g + p_g - p_l) = \mathrm{d}(p + s)$, where $\overline{p}$ is mean stress (or mean pressure), p_l is liquid phase pressure, p_g is gas phase pressure and s is suction. Therefore, a straight line $p + s = \text{constant}$ can be drawn around the current state of stress and suction along which no microstructural strain takes place. This line, called Neutral Line (NL), moves with the current stress state (C) and separates at each instant the zone of microstructural swelling from the zone of microstructural shrinkage in the $p - s$ plane (Figure 2.3).

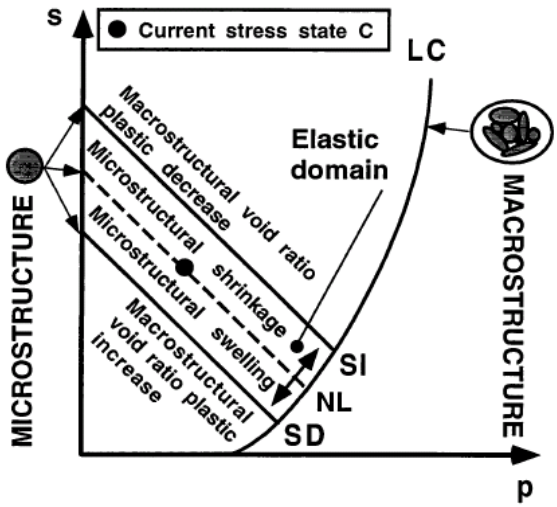

Figure 2.3. Microstructural and macrostructural elastoplastic responses in a double-structure model equivalent to the Barcelona Expansive Model.

Interaction between structural levels

Microstructural swelling affects the structural arrangement of the macrostructure, inducing an irreversible increase of the macroporosity. Reciprocally, microstructural shrinkage induces an irreversible decrease of the macroporosity. In BExM, the irreversible macrostructural deformations induced by microstructural effects are considered proportional to the microstructural strain according to interaction functions with the general form:

$$\mathrm{d}\varepsilon_{v\beta}^{p} = f\mathrm{d}\varepsilon_{vm}^{e} \tag{2.7}$$

where $\varepsilon_{v\beta}^{p}$ is the macrostructural plastic strain arising from the interaction between both structures. Two interaction functions are defined; f_c for MC (microstructural contraction) path and f_s for MS (microstructural swelling) paths (Sánchez et al., 2005). Alonso et al. (1999) proposed the following possible interaction functions, in which case for isotropic loading, f_c (or f_I, corresponding to a drying process in which the soil shrinks) and f_s (or f_D, corresponding to a wetting process in which the soil swells) depend on the ratio p/p_o (Figure 2.4)

$$f_c = f_{c0} + f_{c1}\left(p/p_0\right)^{n_c} \text{ and } f_s = f_{s0} + f_{s1}\left(1 - p/p_0\right)^{n_s}, \tag{2.8}$$

The ratio p/p_o is a measure of the distance from the current stress state to the yield locus for the macrostructure *LC* and has the same meaning as the overconsolidation ratio for an isotropically consolidated soil. A low p/p_o implies a dense packing of the material. It is expected that under such dense packing (dense macrostructure), the microstructural swelling strongly affects the global arrangement of clay aggregates, which becomes more open. This results in a softening of the macrostructure, which implies that the macrostructural yield surface *LC* shrinks. Under this condition, expansion accumulates upon suction cycles. On the other hand, a high p/p_o implies a looser macrostructure. Thus, the microstructural swelling produces an invasion of the macropores, which tends to close the macrostructure and compression accumulates upon suction cycles. In such a case, the elastic domain increases and *LC* expands (Alonso et al. 1999; Sánchez et al., 2005).

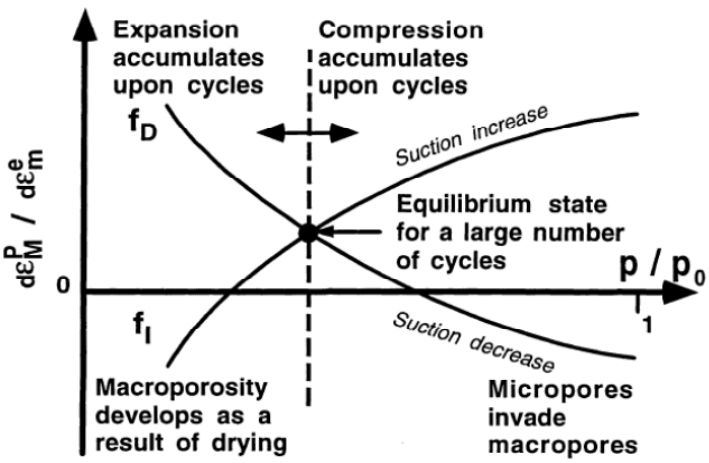

Figure 2.4. Summary of micro–macropore interaction mechanisms.

Elastic Strain

Equivalent to the BBM model, the macrostructural volumetric elastic strain increment for the BExM model is associated with changes in net mean stress dp and suction ds (Alonso et al., 1999)

$$\mathrm{d}\varepsilon_{vM}^{e} = \frac{1}{K_M}\mathrm{d}p + \frac{1}{K_s}\mathrm{d}s \tag{2.9}$$

where K_M is the macrostructural bulk modulus and K_s is the modulus associated with suction strain. K_M and K_s are defined as

$$K_M = \frac{(1+e_M)p}{\kappa_{ps}(s)}, \tag{2.10}$$

$$K_s = \frac{(1+e_M)(s+p_{atm})}{\kappa_{sp}(p,s)} \tag{2.11}$$

where $\kappa_{ps} = \kappa_{Ps0}(1+s\alpha_{ps})$ κ_{ps} and κ_{sp} are compressibility parameters for changes in neat mean stress and suction, respectively, and α_{ps} is an empirical parameter.

In BExM, the microstructural volumetric strain depends on the change in the microstructural effective stress

$$\mathrm{d}\varepsilon_{vm}^{e} = \frac{1}{K_m}\mathrm{d}\hat{p} \tag{2.12}$$

where K_m is the microstructural bulk modulus for change in mean effective stress. Alonso et al. (1999) define two alternative laws for the microstructural behavior through two alternative expressions for the microstructural modulus

$$K_m = \frac{(1+e_m)\hat{p}}{\kappa_m}, \tag{2.13}$$

$$K_m = \frac{e^{-\alpha_m \hat{p}}}{\beta_m}, \tag{2.14}$$

where κ_m, α_m and β_m are compressibility parameters.

The deviatoric elastic strain increment is defined as

$$\mathrm{d}\varepsilon_q^e = \frac{1}{3G}\mathrm{d}q \tag{2.15}$$

where G is the shear modulus and may be obtained using a constant Poisson's ratio ν in

$$G = \frac{3(1-2\nu)}{2(1+\nu)} K_M . \tag{2.16}$$

Thus, the equations for elastic mechanical strain indicate the dependency of bulk modulus on suction (and hence fluid saturation), which in a dry clay can be significantly stiffer than in a water-saturated clay.

Plastic Strain

Macrostructural plastic strain occurs by two possible mechanisms: either when the stress lies on the LC yield surface, or as a result of microstructural contraction/swelling (MC and MS path). The increment of plastic volumetric macrostructural strain is described as a result of microstructural contraction/swelling as

$$\mathrm{d}\varepsilon_{v\beta}^p = f\mathrm{d}\varepsilon_{vm}^e , \tag{2.17}$$

where $\mathrm{d}\varepsilon_{v\beta}^p$ is the macrostructural plastic strain as a result of microstructural contraction/swelling (MC or MS path, respectively).

When the stress state lays on the LC yield surface, the plastic strains are obtained from the plastic flow rule

$$\mathrm{d}\varepsilon_{vLC}^p = \mathrm{d}\Lambda \frac{\partial g}{\partial p} , \tag{2.18}$$

$$\mathrm{d}\varepsilon_{qLC}^p = \mathrm{d}\Lambda \frac{\partial g}{\partial q} , \tag{2.19}$$

where $d\Lambda$ is the plastic multiplier obtained from the consistency condition $\mathrm{d}f_{LC} = 0$ (recall Eq. (2.4)).

The macrostructural plastic strain induced by microstructural volumetric strain is given by the flow rule at the image point on the LC yield surface. The coordinates of the image point (p^*, q^*, s^*) are given by (Alonso et al., 1999) (Figure 2.5)

$$p^* = \frac{\eta^2 k_s s - M^2 p_0}{\eta^2 - M^2},\ q^* = \eta\left(p + k_s s\right),\ s^* = s \tag{2.20}$$

where $\eta = \dfrac{q}{p + k_s s}$.

The total plastic volumetric strain is the sum of both plastic mechanisms

$$\mathrm{d}\varepsilon_v^p = \mathrm{d}\varepsilon_{vLC}^p + \mathrm{d}\varepsilon_{v\beta}^p . \tag{2.21}$$

Then the hardening variable of the macrostructure — the pre-consolidation pressure p_0^*—depends on the total plastic volumetric strain ε_v^p, which is the sum of the plastic strain induced by LC yielding (ε_{LC}^p) and the plastic strain induced by microstructural strain impact on the macrostructure ($\varepsilon_{v\beta}^p$). That is,

$$\frac{\mathrm{d}p_0^*}{p_0^*} = \frac{(1+e_M)\mathrm{d}\varepsilon_v^p}{\lambda_{Ps0} - \kappa} . \tag{2.22}$$

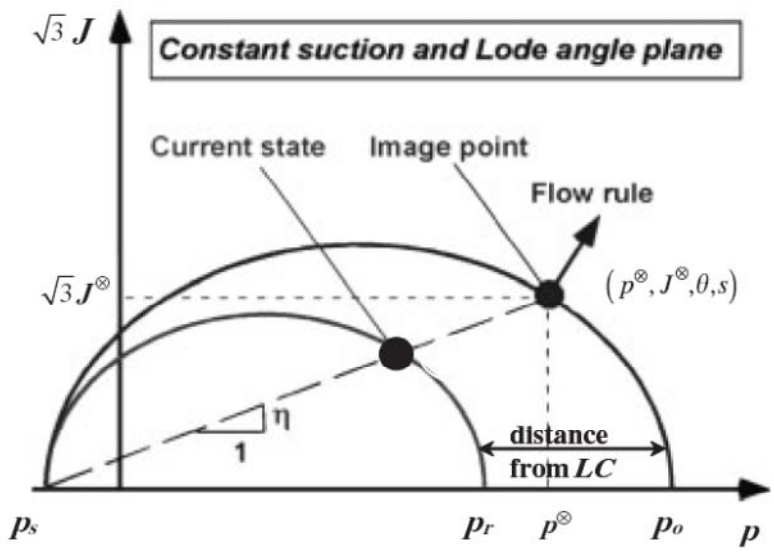

Figure 2.5. Reference pressure and plastic flow direction (Sánchez et al. 2005).

2.1.2 Implementation of BExM into TOUGH-FLAC

We implemented the BExM in FLAC^{3D}, by extending our previous implementation of the BBM to include the microstructure level and its interactions with the macrostructure. This is done using the User Defined constitutive Model (UDM) option in FLAC3D, including C++ coding and dynamic link libraries. Specifically, the following calculation items were added

1) Microstructural strain and effective stress
2) Macrostructural strain
3) Global elastic tensor depending on microscopic and macroscopic structural compliances
4) Micro/macrostructural interaction functions
5) Plastic macrostructural strain from structural interactions
6) Plastic corrections in the FLAC3D elastoplastic algorithm
7) Plastic hardening/softening factors

Implementation of the first five items is straightforward, whereas items 6 and 7 are related to the FLAC3D elastoplastic algorithm and involve calculation of the plastic multiplier dΛ associated with the elastic predictor-plastic corrector algorithm in FLAC3D. In this algorithm, current stress increments are

guessed (by Hooke's law) and added to the stresses from the previous time step, and then corrected back to the yield surface if the calculated principal stresses violate the yield criterion. Using such an approach the current stress is calculated as

$$p = p_{est} + K\mathrm{d}\Lambda c_a \tag{2.23a}$$

$$q = q_{est} + K\mathrm{d}\Lambda c_b \tag{2.23b}$$

where p_{est} and q_{est} are the estimated stresses obtained in the previous step, plus the current incremental elastic estimates, and constants c_a and c_b are the components normal to the plastic potential calculated as (Rutqvist et al., 2011):

$$c_a = M^2\left(2p - p_c + p_s\right) \tag{2.24a}$$

$$c_b = \alpha_a 2q \tag{2.24b}$$

The value of the plastic multiplier dΛ is defined by substituting Equations (2.24a) and (2.24b) in Equation (2.4), requiring that the new stress point be located on the yield surface ($f_{LC}(q, p) = 0$). Then,

$$a(\mathrm{d}\Lambda)^2 + b\mathrm{d}\Lambda + c = 0 \tag{2.25}$$

where

$$a = \left(MKc_a\right)^2 + \left(3Gc_b\right)^2 \tag{2.26a}$$

$$b = -\left[Kc_a c_a^e + \frac{3}{\alpha_a} Gc_b c_b^e\right] \tag{2.26b}$$

$$c = f\left(q_{est}, p_{est}\right) \tag{2.26c}$$

Finally, FLAC^{3D} evaluates new stresses p and q from Equations (2.23a) and (2.23b) using the expression for dΛ corresponding to the root of Equation (2.25) with the smallest magnitude (Rutqvist et al., 2011). In the case of microstructural contraction or swelling (i.e., MC or MS path), the components normal to the plastic potential are given by substituting p and q with p^* and q^* into (2.23a) and (2.23b). In the case of simultaneous *LC* yield and microstructural contraction or swelling, the stress state will be on the *LC* surface, and therefore $p = p^*$ and $q = q^*$, and Equations 2.23–2.26 are still valid.

Finally, at the end of each FLAC3D step, the hardening parameter, i.e., the pre-consolidation pressure p_0^*, the bulk modulus of both microstructure and macrostructure and the tangential bulk modulus, are updated based on the total plastic volumetric strain and stress state, and these are stored for use in the next step.

2.1.3 Testing and verification of implementation

Expansive clays show a non-reversible behavior when they undergo several wetting-drying cycles. This phenomenon cannot be reproduced with the BBM model, but the incorporation of the interactions between the microstructure and the macrostructure of an expansive soil allows accumulating plastic strain. To test our implementation of the BExM, we perform cyclic wetting-drying tests based on the ones presented by Alonso et al. (1999) and Sanchez et al. (2005).

First, we perform a cyclic wetting-drying test under a very low confining pressure (0.01 MPa). In this test example, the macrostructure is dense and expansion is expected to accumulate upon cycles because macroporosity will develop as a result of the interaction between the microstructure and the macrostructure. Figure 2.6 shows how expansion accumulates upon suction cycles. Furthermore, the magnitude of the plastic strain decreases upon cycles, because the plastic strain that occurs during wetting and dryings tends towards equilibrium. This can be observed from the interaction functions (Figure 2.7).

As the number of cycles increases, the interaction functions converge towards the equilibrium point (point *E* in Figure 2.7) and the accumulated expansion between two successive suction cycles decreases (Figure 2.8). Note that since the confining pressure is low, the ratio between the mean net stress and the apparent pre-consolidation stress is small, so suction cycles occur mainly on the left side of the equilibrium point *E*. This results in a net expansion of the soil sample. Therefore, after a cycle of wetting and drying, the plastic strain that occurs during wetting is higher than the one of drying (Figure 2.8). Since the soil expands during wetting, this gives rise to an overall expansion of the soil.

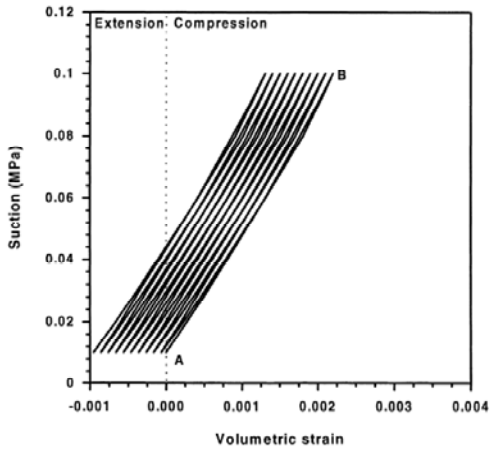

Figure 2.6. Strain evolution during suction cycles for a low confining pressure.

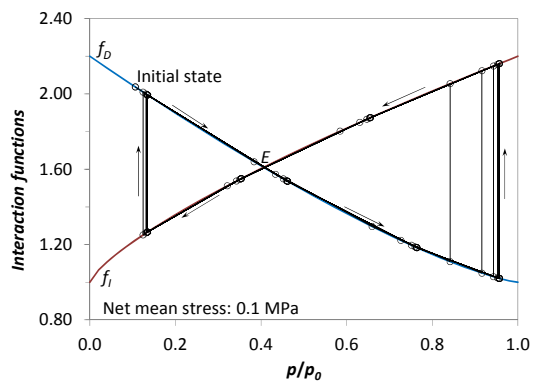

Figure 2.7. Evolution of the interaction functions for a low confining pressure.

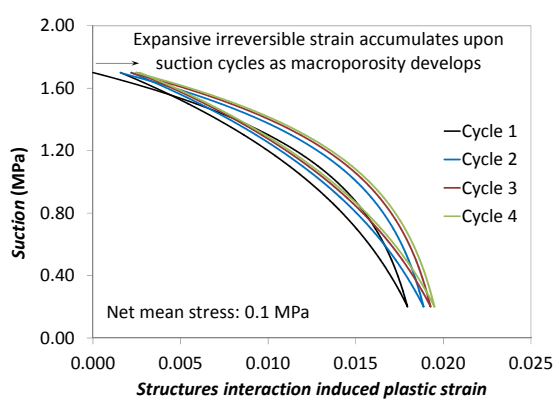

Figure 2.8. Evolution of the plastic strain due to the interaction between the microstructure and the macrostructure for a low confining pressure.

During suction cycles the microstructure behaves elastically (Figure 2.9). However, the macrostructure accumulates plastic strain, so its behavior is not reversible (Figure 2.10). Nevertheless, the expansion that accumulates upon each cycle decreases with number of cycles, so the macrostructure will eventually behave elastically.

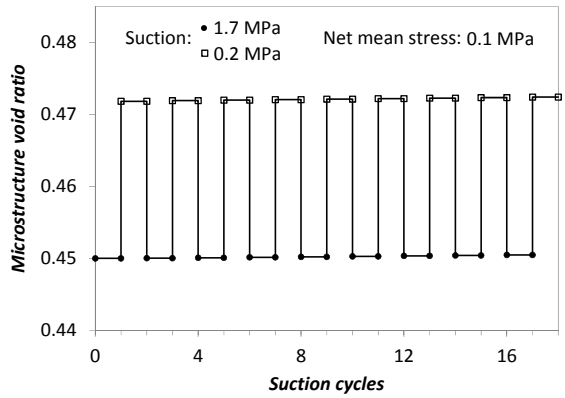

Figure 2.9. Void ratio evolution of the microstructure during suction changes for a low confining pressure.

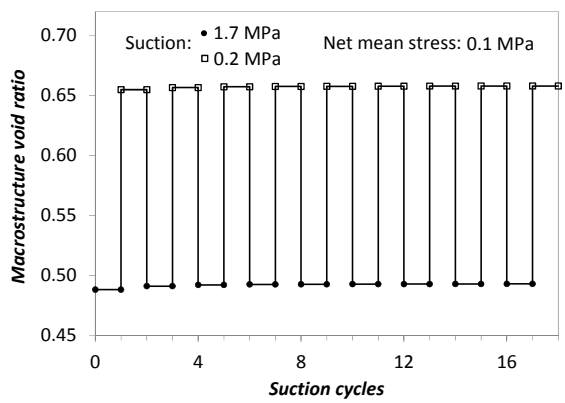

Figure 2.10. Void ratio evolution of the macrostructure during suction changes for a low confining pressure.

On the other hand, when the confining pressure is high the stress state is close to the LC yield surface and the macrostructure is relatively loose, so the microstructure will invade the macropores and compression will accumulate upon cycles (recall Figure 2.6). Figure 2.11 shows the strain evolution during suction cycles and how compression accumulates upon cycles. Note that in the first cycle the compression is much larger than in the other cycles. This is because the LC yield surface becomes active during the first wetting. In the following cycles, the LC yield surface does not become active. Similarly to the other case, the microstructure behaves elastically but the macrostructure does not.

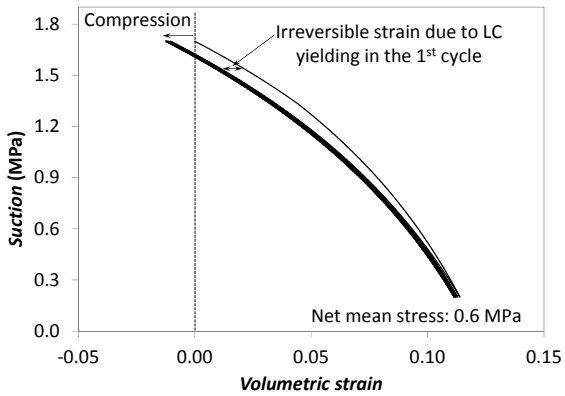

Figure 2.11. Strain evolution during suction cycles for a high confining pressure.

We show with these two opposite examples that the implementation of the BExM model in FLAC3D reproduces the behavior of expansive clays. We also calibrate our model to reproduce the results of a laboratory experiment made by Pousada (1984) (Figure 2.12). Our results are shown in Figure 2.13 and the values of the parameters used for this test are displayed in Table 2.1.

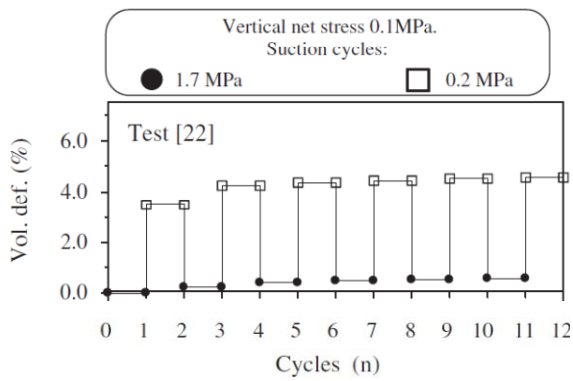

Figure 2.12. Volumetric deformation upon suction cycles reported by Pousada (1984) in an oedometric test under a vertical stress of 0.1 MPa.

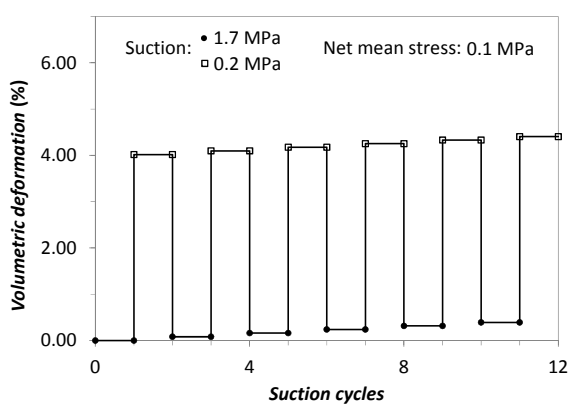

Figure 2.13. Volumetric deformation upon suction cycles mimicking the test of Pousada (1984).

Table 2.1. Parameters used to reproduce the suction cycles test of Pousada (1984).

Parameters defining the Barcelona Basic Model for macrostructural behavior

κ=0.01 κ_s=0.0001 $\lambda(0)$=0.065 p^c (MPa)=0.01 r=0.96 ξ (MPa^{-1})=0.2 p_0^* (MPa)=0.75

Parameters defining the law for microstructural behavior

α_m(MPa^{-1})=0.8 β_m(MPa^{-1})=0.01

Interaction functions between the microstructure and the macrostructure

$f_c = 1.0 + 1.2(p/p_0)^{1.3}$ $f_s = 1.0 + 1.2(1 - p/p_0)^{0.7}$

e_{micro}=0.45 e_{macro}=0.55

2.2 Linking dual-structure model to chemistry and testing

The BExM can be linked to chemistry through the dependence of β_m (see Eq. 2.14) on exchangeable cation concentration as shown in the following equation (Gens, 2010):

$$\beta_m = \sum_i \beta_m^i x_i \,, \tag{2.27}$$

where x_i is the equivalent fraction of the exchangeable cation, i, ranging from 0 to 1, and β_m^i is the parameters that control the microstructure stiffness and defined for each of the exchangeable cation. If a rough analogy is made with diffuse double layer theory, β_m^i is proportional to the ionic hydrated radius and inversely proportional to its valence (Guimaraes et al., 2013). Typically we have $\beta_m^{Li} > \beta_m^{Na} > \beta_m^{K}$ and $\beta_m^{monovalent} > \beta_m^{bivalent}$. After implementing equation 2.27 in TOUGHREACT-FLAC, we compute a hypothetical case to illustrate the effect of changes in concentrations of exchangeable cations on the volumetric strain.

We model a sample of 2 cm^3 discretized in 20 elements of 1 mm in the vertical direction. The properties of the expansive clay are summarized in Table 2.2. The experiment is performed under constant confining stress of 0.2 MPa. The sample has an initial water saturation degree of 0.5. The sample is wetted by injecting water through the bottom of the sample until the sample becomes practically saturated (water saturation degree of 0.98).

Table 2.2. Parameters used to test the effect of chemistry on the swelling capacity of expansive clays.

Parameters defining the Barcelona Basic Model for macrostructural behavior						
κ=0.001	κ_s=0.0001	$\lambda(0)$=0.065	p^c (MPa)=0.01	r=0.96	ξ (MPa^{-1})=0.2	p_0^* (MPa)=7.5
Parameters defining the law for microstructural behavior						
α_m(MPa^{-1})=0.8		β_m(MPa^{-1})=variable				
Interaction functions between the microstructure and the macrostructure						
$f_c = 1.0 + 1.2(p/p_0)^{1.3}$		$f_s = 1.0 + 1.2(1 - p/p_0)^{0.7}$				
e_{micro}=0.45	e_{macro}=0.55					
Permeability of the sample						
k=5·10^{-18} m^2						
Van Genuchten retention curve						
P_0 (MPa)=0.11		λ=0.19	S_{lr}=0.1			

The initial pore water composition is assumed to be the same as FEBEX bentonite (Fernandez et al., 2001). We model two scenarios here. In the first one the sample is saturated with 1 M NaCl solution, and in the second case the sample is saturated with 1M $CaCl_2$ solution. The model runs for 3 days and it takes about 1.5 days to fully saturate the sample (Figure 2.14). Initially exchangeable Ca (X_Ca) is the dominant exchangeable cation that accounts for about 90% of total sites. When the sample is hydrated with 1 M $CaCl_2$ solution, equivalent fraction of exchangeable Ca continues to increase over the course of hydration because the incoming aqueous Ca exchange with other cation from the exchangeable sites (Figure 2.15). If we hydrate the sample with 1 M NaCl, as shown in Figure 2.16, the exchangeable Na (X_Na) eventually dominates the exchangeable sites by taking over about 80% of the equivalent fraction. Based on the fact that β_m^i is proportional to the ionic hydrated radius and inversely proportional to its valence (Guimaraes et al., 2013), we can roughly estimate β_m^i using the following equation:

$$\beta_m^i = \kappa r^i / v^i, \tag{2.28}$$

where κ is a constant that has to be calibrated and r^i is hydrated radii of the cation and v^i is the valence of the cation. The hydrated radius for Na, K, Ca and Mg are 7.9, 5.3, 9.6 and 10.8 Å, respectively (Mitchell and Soga, 2005). For this case we use a κ of 3.24×10^{-4} Å^{-1} MPa^{-1} and the calculated β_m for the case with NaCl solution at the end of saturation is 2.45×10^{-3} MPa^{-1} and that for the case with $CaCl_2$ solution is 1.6×10^{-3} MPa^{-1}. Using these β_m, we calculate the volumetric strain (Figure 2.17). Model results show that NaCl solution leads to a volumetric strain that is 47% higher than a $CaCl_2$ solution, which is qualitatively consistent laboratory test results (e.g. Di Maio, 1996).

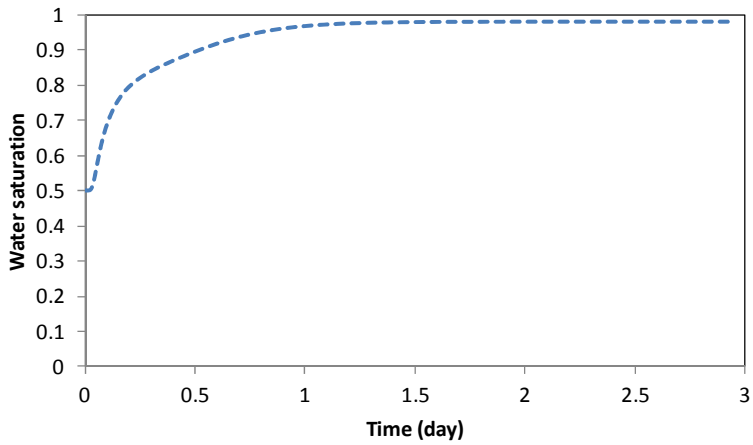

Figure 2.14. Changes in water saturation in the middle of the sample (sample is hydrated from the bottom).

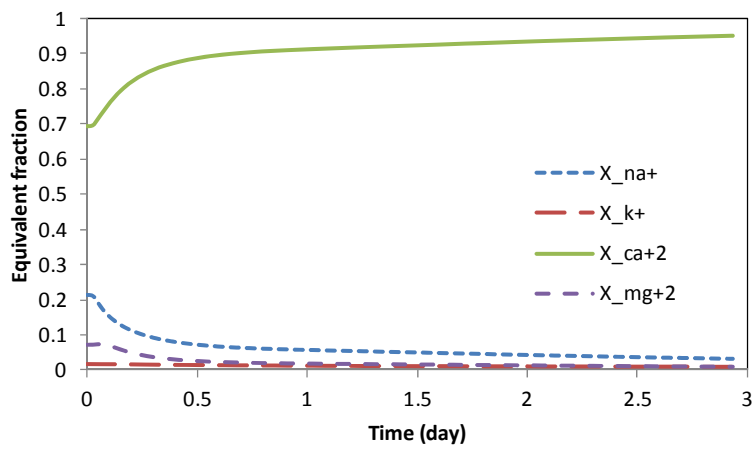

Figure 2.15. Changes in equivalent fraction of each cation in the middle of the sample when the sample is saturated with 1M $CaCl_2$ solution.

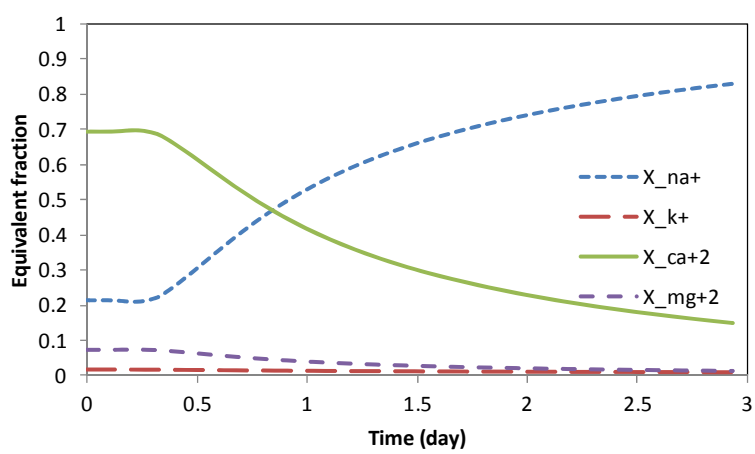

Figure 2.16. Changes in equivalent fraction of each cation in the middle of the sample when the sample is saturated with 1M NaCl solution.

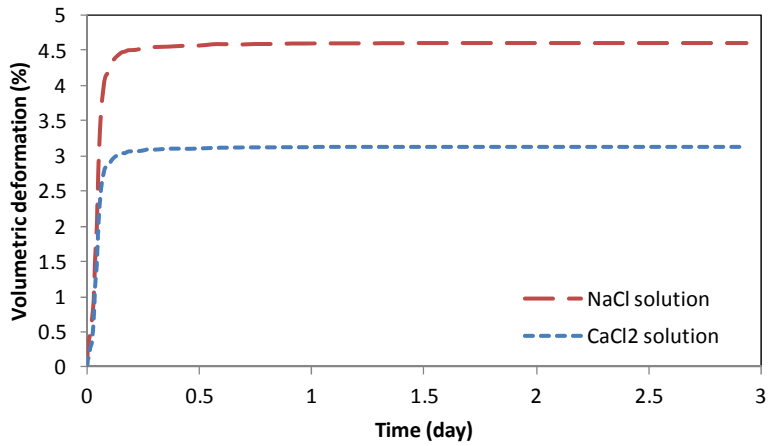

Figure 2.17. Volumetric deformation in the middle of the sample for the case with 1 M NaCl and $CaCl_2$ solution.

Although the modeling exercise presented here demonstrates the modeling capability of TOUGHREACT-FLAC that accounts for the effect of exchangeable cations, our confidence level will be increased if we can validate our model with laboratory data. However, those published laboratory tests (e.g. Di Maio, 1996; Wakim et al., 2009) typically lack detailed characterization of the geochemical parameters such as mineralogical and aqueous composition, which makes it difficult to find a suitable laboratory test.

2.3 Summary

We are developing and applying coupled THMC models for the analysis of EBS coupled processes in bentonite-backfilled repositories. We based this development on the extension of the Barcelona Basic Model to a dual-structure model for expansive clay, such as bentonite. We have implemented of the dual-structure model into TOUGH-FLAC and we have tested the model against literature data from experiments and independent models, although more testing is underway. We have also successfully linked the dual-structure model to chemistry in a rational approach suggested by Gens (2010), enabling the analysis of the effects of exchangeable cations on swelling strain. We are currently working on a more rigorous approach in linking the dual-structure model with the diffuse double layer theory for the coupling between chemistry and mechanics, resulting in a more complete coupled THMC model for the analysis of various THMC processes relevant to the long-term EBS behavior and stability.

3. MODELING REACTIVE DIFFUSIVE TRANSPORT

Engineered clay barriers have remarkable macroscale properties, such as high swelling pressure (Gonçalvès et al., 2007), very low permeability (Mammar et al., 2001), semi-permeable membrane properties (Malusis et al., 2003), and a strong coupling between geochemical, mechanical, and osmotic properties (Malusis and Shackelford, 2004; Gonçalvès et al., 2007). These properties are thought to arise from the distinct geochemical, transport, and mechanical properties of the interlayer nanopores of swelling clay minerals, such as Na-montmorillonite and other smectites (Gonçalvès et al., 2007).

In compacted smectite-rich media, most of the pore space is located in clay interlayer nanopores with the width of a few statistical water monolayers (Kozaki et al., 2001; Bourg et al., 2006). The complex microstructure of these clay barriers (Cebula et al., 1979; Melkior et al., 2009) can be approximated with a conceptual model in which all pores are identical planar pores between parallel negatively-charged

smectite surfaces. With this model, the width of the interlayer pores can be derived from the dry bulk density of the smectite, and properties such as the anion exclusion volume or the swelling pressure of the clay barrier can be predicted by solving the Poisson-Boltzmann equation in the space between the parallel, negatively charged clay particles (Gonçalvès et al., 2007; Tachi et al., 2010). Solving the Poisson-Boltzmann equation, however, is not a minor exercise when carried out in the context of a general multicomponent framework. In addition, it requires a fine discretization to capture the chemical and electrostatic gradients in the vicinity of the charged clay surfaces. This is why we are also pursuing a mean electrostatic approach, which makes it easier to consider larger length scales for transport (e.g., Tournassat and Appelo, 2011). The Poisson-Boltzmann approach, or even the Mean Electrostatic (or Donnan equilibrium) approach that is based on it, potentially provides a more mechanistic treatment of swelling pressure and anion exclusion than is possible with the largely empirical approaches employed by Gens (2010) and Guimarães et al (2013).

Microstructural investigations of compacted smectite-rich media reveal the existence of *crystalline hydrates* (known as the 1-, 2-, and 3-layer hydrates, in which the interlayer nanopore contains one, two, or three statistical water monolayers) at dry bulk densities where the average pore size is much larger than the width of the largest crystalline hydrate (Kozaki et al., 2001; Holmboe et al., 2012). These studies show that compacted smectite contains at least two types of pores: (1) crystalline hydrate nanopores with a width of 0.3, 0.6, or 0.9 nm (the 1-, 2-, and 3-layer hydrates); and (2) a population of larger, poorly characterized pores. Models that account for this "bimodal" distribution of pore widths (Bourg et al., 2006; Ichikawa et al., 2004; Tournassat and Appelo, 2011) provide useful insights into the diffusion of water and cations in the EBS. The power of these models arises from the fact that they can harness the extensive knowledge base that exists on the behavior of water and ions in the crystalline hydrate nanopores, from experimental (Sposito and Prost, 1982; González Sánchez et al., 2009; Ferrage et al., 2011; Marry et al., 2011) and molecular modeling studies (Sposito et al., 1999; Rotenberg et al., 2007a; Kosakowski et al., 2008; Bourg and Sposito, 2010; Churakov and Gimmi, 2011).

Several key properties of the EBS, however, such as anion diffusion and water advection, are likely to be determined by the largest pores in the compacted clay system rather than by the crystalline interlayer nanopores. The "bimodal" models of smectite clay barriers listed above either assumed that the water in the large pores is similar to bulk liquid water (Bourg et al., 2006, 2007, 2008; Bourg and Sposito, 2010) or they artificially assigned a width to these large pores [or equivalently, a value to the ratio of the number of crystalline hydrate nanopores to larger pores (Ichikawa et al., 2004; Tournassat and Appelo, 2011)]. Obviously, neither approach is satisfactory for predicting anion diffusion or water flow in the EBS. In the present project, we are developing a new model of diffusion in the EBS based on the knowledge that in conditions relevant to the EBS, Na-smectite has only four stable swelling states. These states are the 1-, 2-, 3-layer crystalline hydrates, with *d*-spacings d_{001} = 12.4, 15.4, 18.4 (Norrish, 1954; Holmboe et al., 2012), and the smallest possible "osmotic hydrate" with an average reported *d*-spacing of 32.7 ± 2.4 Å (Foster et al., 1955; Zhang and Low, 1989; Wilson et al., 2004). We hypothesize that compacted water-saturated Na-smectite can be approximated, at any dry bulk density, as a mixture of (at most) two swelling states. For a smectite consisting of a single swelling state with a basal spacing d_{001}, the dry bulk density ρ_b is given by the simple relation:

$$\rho_b = \frac{\rho_s d_s}{d_{001}} \tag{3.1}$$

where d_s = 9.4 ± 0.1 Å and ρ_s = 2.84 ± 0.04 kg dm^{-3} are the thickness and density of a smectite lamellum. We expect, therefore, that Na-smectite at ρ_b = 0.82 ± 0.06 kg dm^{-3} consists entirely (with minor deviations due to imperfect stacking of clay particles) of the smallest osmotic hydrate (with $d_{osmotic}$ = 32.7 ± 2.4 Å), whereas at ρ_b = 1.45 ± 0.05 kg dm^{-3}, it consists entirely of the 3-layer hydrate (with $d_{3\text{-layer}}$ = 18.4 ± 0.5 Å). At intermediate values of ρ_b, Na-smectite must consist of a mixture of the smallest osmotic hydrate and the largest crystalline hydrate as shown by the XRD results of Holmboe et al. (2012). The fraction of clay interlayers that form the osmotic hydrate ($X_{osmotic}$) can be determined from the relation:

$$\rho_b = X_{\text{osmotic}}\left(\frac{\rho_s d_s}{d_{\text{osmotic}}}\right) + \left(1 - X_{\text{osmotic}}\right)\left(\frac{\rho_s d_s}{d_{\text{3-layer}}}\right) \tag{3.2}$$

According to the simple conceptual model proposed above, in the range of dry bulk densities of interest in EBS applications, no assumptions need to be made regarding the size of the largest pores in any compacted water-saturated Na-smectite sample. The pores in the system consist of a mixture of the 3-layer hydrate and the smallest osmotic hydrate, and the relative proportion of the two types of pores varies with the dry bulk density ρ_b.

The simple conceptual model proposed above suggests that EBS performance (ion diffusion, water flow, semi-permeable membrane properties, swelling pressure) depends on the properties of the smallest osmotic hydrate (with d_{001} = 32.7 ± 2.4 Å) and the largest crystalline hydrates (the 3-layer hydrate with d_{001} = 18.4 ± 0.5 Å, and possibly also the 2-layer hydrate at very high degrees of compaction). The two types of pores have significantly different properties: for example, the crystalline hydrates are so narrow that the behavior of water and ions is dominated by short-range interactions with the clay surface, whereas the osmotic hydrate is sufficiently large that long-range, mean-field interactions in the so-called electrical double layer (EDL) play an important role (Tournassat et al., 2009; Bourg and Sposito, 2011b).

In this subtask, we describe the development of our conceptual model and its application to the self-diffusion of water and "hard" acids and bases (alkali metals, chloride). To develop our model, we apply a combination of microcontinuum scale models based on the Poisson-Boltzmann and Poisson-Nernst-Planck equations, to elucidate the coupling between EDL phenomena and molecular diffusion in clay nanopores, and molecular dynamics (MD) simulations, to gain insight into the influence of short-range intermolecular interactions on diffusion in clay nanopores. Our conceptual model will be broadened in the future to describe other phenomena that are discussed in this report, such as coupled THM processes (Section 2) or the diffusion of UO_2^{2+} (Section 4). Specifically, we propose to use the Poisson-Boltzmann equation, and the Mean Electrostatic Model based on it, to develop mechanistic descriptions of clay swelling pressure. Rather than being empirically based on cation exchange capacity which incorporates both inner sphere and outer sphere sorption, as well as EDL ions, this will consider the overlap of electrical double layers in the context of Stern layer (inner sphere) sorption. As an application to UO_2^{2+} diffusion, we will simulate uranium transport through the compacted bentonite using the Mean Electrostatic Model, with rigorous treatment of overlapping EDL where appropriate.

During the first part of FY13, we focused primarily on the following aspects:

First, we used micro-continuum scale simulations as described in section 3.1 to investigate the effects of ionic strength on the electrical double layer thickness, and thus on the EDL porosity that is available for diffusive transport. When the bentonite is highly compacted, the EDL porosity may make up the major portion of the porosity available for transport (i.e., bulk water is mostly not present). A dynamic model for EDL thickness was developed and implemented within a general purpose multicomponent reactive transport framework (i.e., one that can consider the full range of aqueous and surface complexation). The simulations demonstrate that ionic strength effects may partly reverse the effects of clay swelling. The model was then validated against a tracer test carried out in the Opalinus Clay, where it was able to capture the transport behavior of both uncharged non-reactive species (HTO) and anionic species (bromide and chloride). In addition, the reaction portion of CrunchEDL is being coupled to Comsol, which will make it possible to consider both pore scale electrostatic effects on diffusion and flow (including non-Darcian flow), as well as larger scale porous media behavior at the repository scale.

Second, we used MD simulations to predict the temperature-dependence of diffusion of water and Na^+ in clay nanopores in the temperature range from T = 278 to 353 K. This area of inquiry was selected for two reasons: (1) because temperature in the EBS may range from roughly 283 to 368 K (JNC, 2000; SKB, 2009), whereas most data on diffusion in clay barriers were obtained at or near 298 K; and (2) because the

temperature dependence of diffusion (expressed as an activation energy of diffusion E_a) is a *macroscopic scale* property that directly reflects—if tortuosity and other features that determine the geometric factor of the porous medium are invariant with T—the potential energy landscape explored by the diffusing species at the *pore scale*. Therefore, macroscopic measurements of E_a, when compared with pore-scale predictions of E_a obtained by MD simulation, yield direct information on the predominant diffusion pathway of the species of interest (e.g., does the species diffuse preferentially in the crystalline hydrate or in the osmotic hydrate?). This research is described in Section 3.2

During the remainder of FY13, we plan to focus on the following activities: (1) we plan to begin simulations of the UO_2^{2+} diffusion experiments conducted by Davis and Tinnacher (Section 4); (2) we plan to complete our MD simulation study of the temperature dependence of diffusion in clay nanopores by studying the behavior of Cs^+, Sr^{2+}, Ca^{2+}, Cl^-, and UO_2^{2+}; and (3) we plan to carry out a joint microcontinuum scale and MD simulation study of anion exclusion, the structure of the EDL, and water and ion diffusion in the smallest osmotic hydrate of Na-smectite as a function of ionic strength. These planned activities are described in section 3.3.

3.1 Mean Electrostatic Model for Diffusive Transport in the EBS

3.1.1 Derivation from Poisson-Boltzmann Equation

A rigorous model for the structure of the electrical double layer (EDL) can be derived from the combination of several equations, including the Poisson equation describing the distribution of electrical potential, ψ , in water

$$\nabla^2\psi = -\frac{\rho_z}{\varepsilon}, \tag{3.3}$$

where ε is the permittivity and ρ_z is the volumetric charge density given by

$$\rho_z = e\sum_i z_i C_i^{EDL}. \tag{3.4}$$

In Eq. (3.4), e is the elementary charge of the electron and z_i is the valence of the ion. The Boltzmann distribution gives an expression for the concentration, $C_i^{EDL}(z)$, in the electrical double layer as a function of distance from the charge solid surface, z,

$$C_i^{EDL}(z) = C_i \exp\left(\frac{-z_i e\psi(z)}{k_B T}\right), \tag{3.5}$$

where C_i is here the concentration in the bulk solution, k_B is the Boltzmann constant, and T is the absolute temperature. Combining Eq. (3.5) with the Poisson equation (Eq. (3.3)) yields the Poisson-Boltzmann equation (Schoch et al., 2008)

$$\nabla^2\psi = \frac{-e}{\varepsilon}\sum_i z_i C_i \exp\left(\frac{-z_i e\psi(z)}{k_B T}\right) \tag{3.6}$$

which can be solved exactly for various simple formulations (e.g., the Gouy-Chapman model, which assumes a symmetric electrolyte).

Integrating the Poisson-Boltzmann equation over nanometer length scales from charged mineral surfaces, however, was not practical in the present version of CrunchEDL because of the desire to consider larger length scales, so an alternative approach based on a Donnan Equilibrium model (Wersin et al., 2004; Leroy and Revil, 2004; Appelo et al., 2007; Leroy et al., 2007; Appelo et al., 2008; Birgersson and

Karnland, 2009; Tournassat and Appelo, 2011) is used. The electrical double layer is conceptualized as consisting of two parallel layers of charge, one being the surface charge associated with direct sorption at the mineral surface (the Stern layer, typically divided into an inner and outer Helmholtz layer), and the second being the diffuse layer charge, a swarm of counterbalancing ions (Figure 3.1).

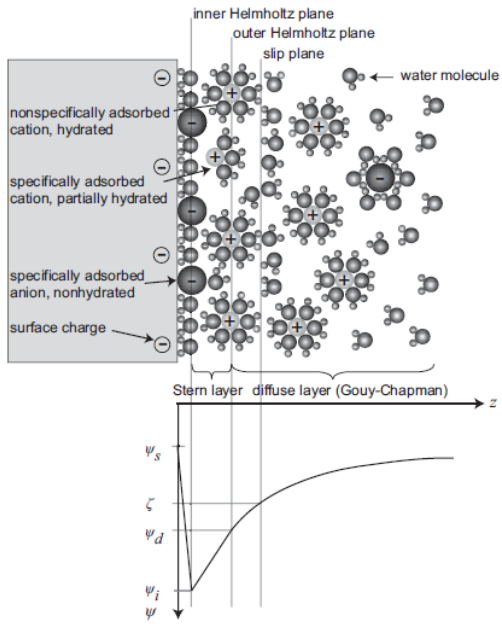

Figure 3.1. Schematic illustration of the Gouy-Chapman-Stern model of the solid-electrolyte interface, with the potential distribution $\psi(z)$ versus distance from the charged solid surface. The solid is illustrated with a negative surface potential ψ_s, described by three layers in solution. The inner Helmholtz plane layer ψ_i consists of nonhydrated co-ions and counterions (inner sphere complexes), whereas the outer Helmholtz plane layer ψ_d is built up of only hydrated counterions (outer sphere complexes). The diffuse layer is defined beyond the outer Helmholtz plane (from Schoch et al., 2008).

In the approach taken in CrunchEDL, the chemical potentials of the species in the diffuse layer and the bulk solution are equated. Writing equations for the chemical potentials of the species *i* in the bulk solution (or macroporosity) (superscript "B") and electrical double layer (superscript "EDL") respectively, we have

$$\begin{aligned} \mu_i^B &= \mu_i^{B,0} + k_B T \ln a_i^B \\ \mu_i^{EDL} &= \mu_i^{EDL,0} + k_B T \ln a_i^{EDL} + q_i \psi_m \end{aligned} \tag{3.7}$$

where the superscript *0* (first term on the right-hand side) refers to the chemical potential at the reference state, a_i are the species activities, q_i is the charge of an ion (the elementary charge of a particle, *e*, multiplied by the valence of the ion, z_i), k_B is the Boltzmann constant, and ψ_m is the mean electrical potential in the electrical double layer. The condition of Donnan Equilibrium implies that

$$\begin{aligned} \mu_i^{EDL} &= \mu_i^B \\ \mu_i^{EDL,0} &= \mu_i^{B,0} \end{aligned} \tag{3.8}$$

Combining Eqs. (3.5), (3.7), and (3.8) and assuming that the activity coefficients for the diffuse layer and bulk solution are the same gives the Boltzmann distribution for the ion activities in the electrical double layer, C_i^{EDL}:

$$C_i^{EDL} = C_i^B \exp\left(\frac{-z_i e\psi_m}{k_B T}\right). \tag{3.9}$$

The diffuse layer charge balances the charge within the Stern layer, Q^{SL}, which may consist in CrunchEDL of either a fixed mineral charge due to vacancies in the mineral structure (as in the case of classical ion exchange), or of fixed mineral charge modified by inner sphere and outer sphere complexes developed within the Stern layer calculated with a surface complexation model:

$$\phi^{EDL} \sum_i z_i C_i^{EDL} = Q^{SL} \tag{3.10}$$

where ϕ^{DL} is the volume (or porosity) of the electrical double layer. The left-hand side of Eq. (3.10) gives a volumetric charge density in units of charge equivalents per unit volume porous medium. The surface charge is given by

$$Q^{SL} = \sum_k^{Ns} z_k \Gamma_k \tag{3.11}$$

where Γ_k is the concentration in units of moles sorbed species per unit volume porous medium and z_k is the valence of the surface complex. In the CrunchEDL approach, therefore, one new equation is introduced (Eq. (3.10)), with one new unknown, the mean electrostatic potential of the diffuse layer, ψ_m. Note that in this formulation, the concentrations of the ions in the diffuse layer are dependent (or secondary) species that are calculated algebraically from the knowledge of the bulk solution composition and the mean electrostatic potential. A kinetic treatment of the diffuse layer ions would require that they be considered as primary unknowns.

Several approaches are available for calculating the fixed or Stern layer charge that is balanced by an electrical double layer. Even if the full Poisson-Boltzmann (PB) equation is used, special consideration needs to be given to the charge present in the Stern layer, a feature not always seen in the simpler implementations of the Poisson-Boltzmann equation. The starting point is the fixed mineral charge, which is normally given by the cation exchange capacity. If no Stern layer sorption occurred, the fixed mineral charge would provide a Dirichlet boundary condition for the electrostatic potential, ψ_f, at the solid surface,

$$\psi(0) = \psi_f . \tag{3.12}$$

In the case of no Stern layer sorption, therefore, the PB equation can be integrated across the entire thickness z of the electrical double layer. In the case where the charged bentonite particles are bordered by bulk water, this would be the point in space where the local solution becomes electroneutral (where the electrostatic potential goes to zero). In the case of overlapping double layers, as considered by Goncalves et al (2007) and Schoch et al (2008), this would be the midpoint between the two charged clay (or solid) surfaces. In the case of overlapping double layers, the boundary condition at the midpoint is that the derivative of the electrical potential goes to zero (Figure 3.2)

$$\left[\frac{\partial \psi}{\partial z}\right]_{z=\frac{1}{2}h} = 0 \tag{3.13}$$

where h is the distance between the two charged solid (clay) surfaces. In the case where Stern layer sorption is not present, the fixed mineral charge (or CEC) is used in CrunchEDL as the charge to be balanced. Where protonation or other cation sorption reactions within the Stern layer also take place, changes in pH and cation concentration will result in changes in the surface charge to be balanced by the EDL. These are treated in CrunchEDL with a surface complexation model, with the EDL charge then calculated from the modified surface charge according to Eqs. (3.10) and (3.11). The surface complexation model can be either electrostatic (with Coulombic corrections to the Gibbs free energy, as in Dzombak and Morel, 1990) or non-electrostatic, in which case the energy associated with charging the mineral surface is captured directly in the equilibrium constant. Note that in the case of overlapping double layers, the conventional Coulombic corrections to the surface complexation constants that are proposed in Dzombak and Morel (1990) are not correct, as discussed by Goncalves et al (2007), since these are based on the assumption of an electrically neutral solution bordering the clay (or in terms of the electrostatic potential, an infinite half-space).

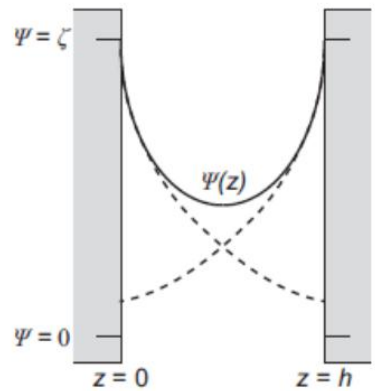

Figure 3.2. Schematic representation of the potential distribution in a nanochannel with height h in direction z when the EDLs overlap (solid line), compared to the EDL potentials if the opposite wall is not present (dashed line). From Schoch et al. (2008).

3.1.2 Dynamic Calculation of Electrical Double Layer Thickness

CrunchEDL also now includes a dynamic calculation of the electrical double layer porosity, ϕ^{EDL}, based on the diffuse layer thickness as a function of ionic strength according to

$$\phi^{EDL} = A_{clay}\lambda_{DL}D_L = A_{clay}\lambda_{DL}\frac{\beta_{DL}}{\sqrt{I}} \tag{3.14}$$

where D_L is the Debye length, λ_{DL} gives the multiples of the Debye length used in calculating the electrical double layer porosity (as in the approach of Tournassat and Appelo, 2011), β_{DL} is a temperature-dependent factor (= $2.15\text{x}10^{-10}$ meters at 25°C), I is the ionic strength of the bulk solution, and A_{clay} is the surface area of the charged mineral surfaces (normally clays). The Debye length provides an approximate measure of the width of the electrical double layer, although in their Donnan or mean electrostatic model, Tournassat and Appelo (2011) included as many as five Debye lengths to describe the EDL porosity.

Previously we have presented results in which the ionic strength is constant over the domain. It is also possible, however, to consider transient cases in which a salinity front propagates through the domain, changing the Debye length and thus the diffuse layer porosity dynamically. Note that in this case, the EDL thickness and thus the transport properties of the compacted bentonite are modified by the changing

ionic strength. The effect is different from the swelling behaviour described in Section 2, and may in fact work in the opposite way.

In the CrunchEDL approach in which solute mass is tracked in both the bulk porosity and the diffuse layer (EDL) porosity, this gives an accumulation term (neglecting liquid saturation) of

$$\frac{\partial\left[\phi^B C_i^B + \phi^{EDL} C_i^{EDL}\right]}{\partial t} = \frac{\partial\left[\phi^B C_i^B + \left(A_{clay}\lambda_{DL}\beta_{DL} \Big/ \sqrt{I}\right) C_i^{EDL}\right]}{\partial t}. \qquad (3.15).$$

In this case, the bulk porosity is treated as a constant, or at least as separately determined or fixed. Since the total porosity then can increase or decrease as the EDL thickness changes, special considerations need to be made to conserve mass in the system. Alternatively, it is preferred to treat the total porosity (bulk and EDL) as constant, in which case the bulk and EDL porosities would be updated according to:

$$\frac{\partial\left[\left(\phi^{Tot} - \phi^{EDL}\right) C_i^B + \phi^{EDL} C_i^{EDL}\right]}{\partial t} \qquad (3.16)$$

where ϕ^{Tot} is the total porosity = $\phi^B + \phi^{EDL}$.

The processes represented by Eqs. (3.15) and (3.16) are captured in a test problem in which a higher ionic strength solution (0.45M) propagates through a 10 cm long column of compacted bentonite that initially has a lower ionic strength (0.045M). In Figure 3.3, the total porosity is fixed at 4%, while the EDL porosity is predicted to change from 3.11% at the lower ionic strength to 0.98% at the higher ionic strength after 5 days of diffusion in the case where a single Debye length in Eq. (3.15) is used to describe the EDL porosity. As a result of the changes in the EDL thickness (and porosity), the bulk porosity changes according to Eq. (3.16) from 0.89% to 3.02% as the salinity front diffuses through the domain. The simulation was carried out by applying Dirichlet and no-flux boundary conditions at the left and right boundaries, respectively. The decrease in the EDL thickness as a result of the salinity front (here considered purely in terms of ionic strength, rather than the specific hydration properties of the cations) results in an increase in the bulk porosity, which should normally increase transport rates for all ions, but particularly for the anions that are either partially excluded or forced to follow more tortuous diffusion paths than would be the case for either cations or uncharged species.

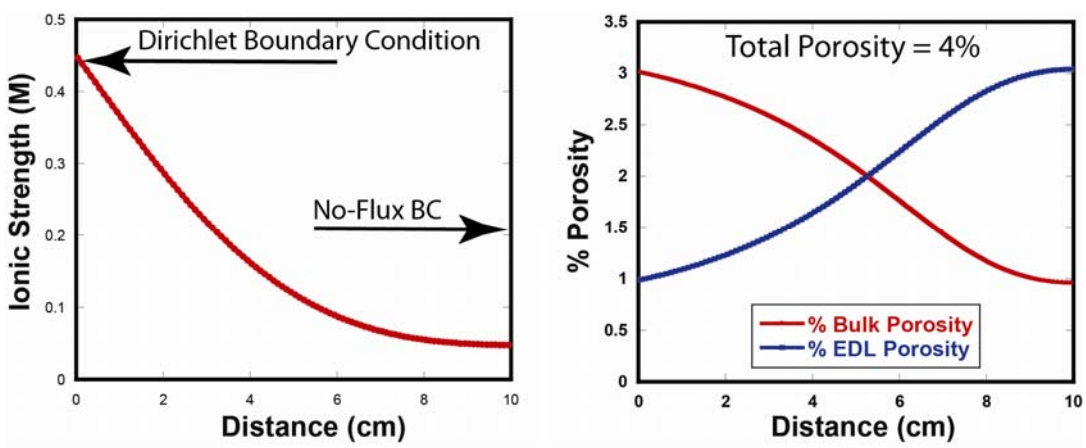

Figure 3.3. Results of dynamic EDL porosity calculations after 5 days of diffusion. Left panel: A high ionic strength front (I=0.45M) diffuses front left to right through the domain that is initially lower ionic strength (I=0.045M). The left boundary is a Dirichlet boundary condition, while the right boundary is no-flux. Right panel: Spatial profiles for bulk porosity and EDL porosity for the case of a constant total porosity of 4%.

3.1.3 Testing of EDL Model using the DR-A Experiment at Mont Terri, Switzerland

To test the EDL transport model developed and described here, we have used it to simulate non-reactive and reactive transport processes in the DR-A experiment at Mont Terri in Switzerland. While the Mont Terri site consists of Opalinus Clay, a primarily marly claystone with differing proportions of sand and carbonates. The Opalinus Clay is about 180 million years old. The stratigraphic section in which the Mont Terri site is located is shown in Figure 3.4. The Opalinus Clay is characterized by a very low permeability, which makes diffusion the dominant mode of solute transport (in this respect, similar to compacted bentonite under normal conditions).

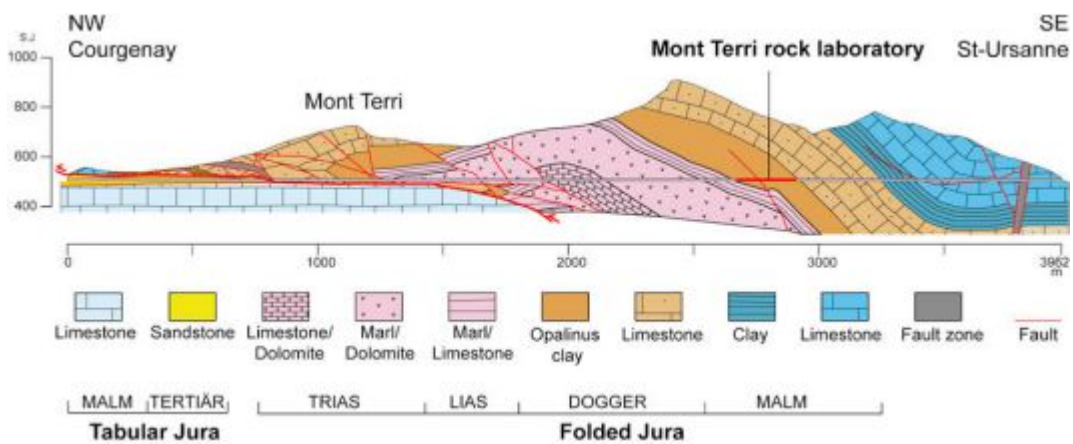

Figure 3.4. Stratigraphic section of the Jura Mountains in which the Mont Terri rock laboratory is located.

The DR-A test to date has consisted of a single borehole drilled in the Opalinus Clay that contains a constant ionic strength cocktail and anions, cations, and non-reactive tracers like tritium (HTO). An experiment in which the ionic strength is varied is underway now and will be the subject of modeling and simulation to be carried out in the next phase. Figure 3.5 shows the experimental setup used for the earlier DI-A test at Mont Terri. The key point is that there is a volume of cocktail in excess of the actual cylindrical volume through which solutes diffuse into the Opalinus Clay. This is treated in CrunchEDL by defining a capacity factor, α (= 2.175), that represents the additional volume needed to accommodate the extra solution volume (11.2 L) available to the actual borehole volume. Doing so and solving in radially symmetric cylindrical coordinates produces the fit of the actual HTO (tritium) data (Figure 3.6).

Table 3.1. Parameters for DR-A test

Length of injection interval	104 cm
Length of filter screen	67 cm
Volume of circulation system	11.2 L
Borehole diameter	76 mm
Filter, outer diameter	70 mm
Filter, inner diameter	62 mm
Filter, porosity	45%
Gap between filter and borehole wall	3 mm
Central tube, outer diameter	61 mm
Dip of bedding	32.5º
Porosity of Opalinus Clay	15%

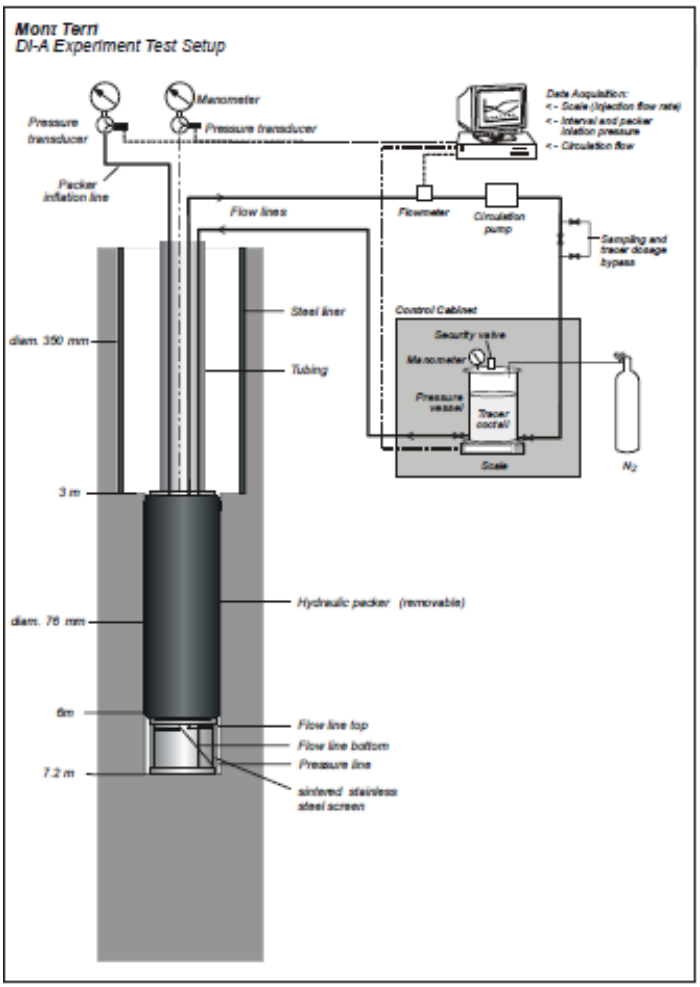

Figure 3.5. Schematic of the experimental setup from the DI-A test, similar in concept to the DR-A test.

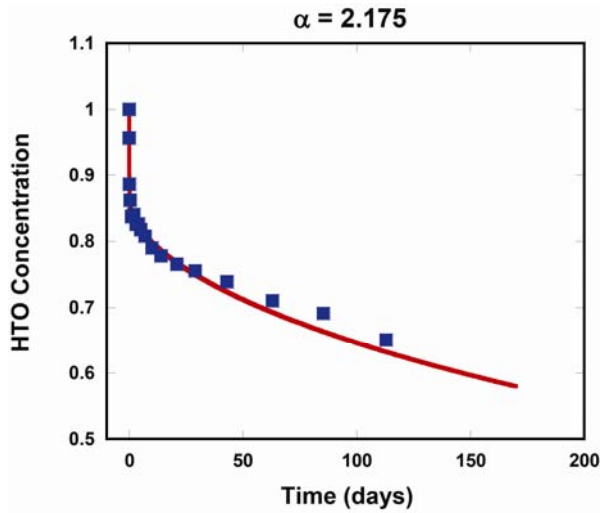

Figure 3.6. Fit of borehole HTO concentration versus time using a capacity factor of 2.175. This is solved in radially symmetric cylindrical coordinates using CrunchEDL.

The same system is then solved for the time evolution of the anions iodide and bromide in the borehole using a diffusion coefficient of 10^{-6} cm^2/s (an order of magnitude slower than the cations and HTO) for the anions in the EDL and one Debye length to define the EDL porosity (Figure 3.7). This is carried out assuming Stern layer sorption, with 20% of the rock made up of illite with $5x10^{-7}$ sites/m^2 having a specific surface area of 200 m^2/g. Note the slower decrease in concentration of the anions relative the HTO in the borehole as a result of anion exclusion in the Opalinus Clay.

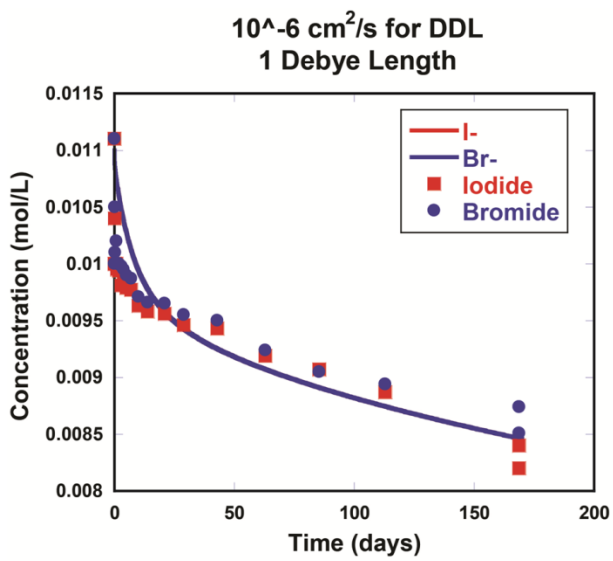

Figure 3.7. Anion concentration versus time in the borehole for the first DR-A test.

3.1.4 Development of a CrunchEDL-Comsol Coupling for Flow and Transport in Charged Porous Media

Now under development is a new coupling of the reaction portion of CrunchEDL with the general purpose flow and transport code Comsol. While CrunchEDL can handle transport through porous media, it is not as well suited to handle pore scale flow and transport, or Navier-Stokes flow in general. The Comsol coupling offers the ability to include Navier-Stokes or Darcian flow, while still solving the full

Nernst-Planck equation (as CrunchEDL does). Figure 3.8 shows a schematic of the coupling procedure between Comsol and CrunchEDL. Followed by an initialization (including initial and boundary condition speciation), the primary exchange between the two routines are the total concentrations, the individual species concentrations when the full Nernst-Planck equation is desired, and the charge density. Total concentrations in the bulk and EDL porosity are tracked and transported separately.

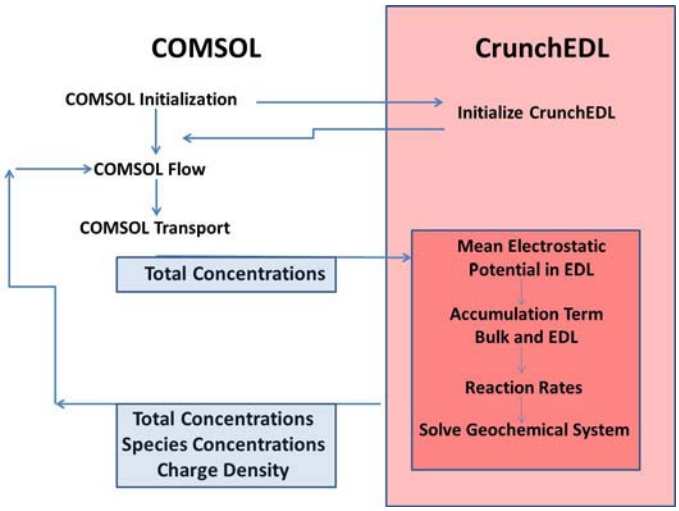

Figure 3.8. Illustration of the coupling scheme between Comsol and CrunchEDL.

3.2 Molecular scale predictions of diffusion in the EBS

3.2.1 Temperature Dependence of Water and Solute Diffusion in the EBS

As noted above, predicting the long-term performance of engineered and natural clay barriers near high-level radioactive waste (HLRW) repositories requires a fundamental understanding of the rates of molecular diffusion in these barriers. The diffusion of water and ions in water-saturated compacted clay barriers has, therefore, been extensively characterized, though mostly at ambient temperatures (Molera and Eriksen, 2002; Molera et al., 2003; Nakashima, 2003; Sato, 2003; Wang et al., 2005; Melkior et al., 2009; Tachi et al., 2010; Glaus et al., 2011; Tanaka et al., 2011; Holmboe et al., 2011).

Because of the large heat flux generated by high-level radioactive waste, the design of HLRW repositories requires knowledge of the self-diffusion coefficients (D) of water and solutes in compacted bentonite over a broad range of temperatures (roughly 283 to 368 K—JNC, 2000; SKB, 2009). The temperature dependence of diffusion (expressed as the activation energy of diffusion E_a through the Arrhenius relation $D \propto \exp(-E_a/RT)$, where R is the ideal gas constant and T is absolute temperature) also is of interest, because it is a *macroscopic scale* property that directly reflects—if tortuosity and other features that determine the geometric factor of the porous medium are invariant with T—the potential energy landscape explored by the diffusing species at the *pore scale*.

The vast majority of measurements of solute E_a values in compacted bentonite were reported by Kozaki and co-workers (Kozaki et al., 1996, 1997, 1998, 1999, 2001, 2005, 2008, 2010; Liu et al., 2003) from diffusion experiments with centimeter scale samples of compacted water-saturated montmorillonite, a common type of smectite. These experiments probed a range of temperatures (T = 278 to 323 K), dry bulk densities (ρ_b = 0.7 to 1.8 kg dm^{-3}), solutes (Na, Cs, Sr, Cl), ionic strengths (I = 0 to 0.5 mol dm^{-3} NaCl), and type of counterion (Na-, Ca-, and mixed Na/Ca-montmorillonite). The results showed that solute E_a values have a particularly strong dependence on dry bulk density. In the case of Na^+ self-diffusion in Na-montmorillonite, according to Kozaki et al. (2005), E_a equals ~18.5 ± 1.5 kJ mol^{-1} (consistent with the

value in bulk liquid water) at low dry bulk densities ($\rho_b \leq 0.8$ kg dm^{-3}), ~15.5 ± 1.5 kJ mol^{-1} at intermediate dry bulk densities ($\rho_b = 0.9$ to 1.2 kg dm^{-3}), and ~25 ± 2 kJ mol^{-1} at high dry bulk densities ($\rho_b \geq 1.6$ kg dm^{-3}).

In the case of water diffusion, E_a values in water-saturated smectite have been studied by a number of research groups using both macroscopic scale diffusion experiments (Nakazawa et al., 1999; Nakashima, 2000; Suzuki et al., 2004; Gonzalez-Sánchez et al., 2009) and quasi-inelastic neutron scattering (QENS) experiments (Gonzalez-Sánchez et al., 2009; Marry et al., 2011). These studies yielded conflicting results, with two groups (Nakazawa et al., 1999; Nakashima, 2000) reporting E_a values of 15 to 19 kJ mol^{-1} [near the value for bulk liquid water, 17.4 ± 0.2 kJ mol^{-1} in the temperature range 278-353K (Holz et al., 2000)] and three groups (Suzuki et al., 2004; Gonzalez-Sánchez et al., 2009; Marry et al., 2011) reporting E_a values of 19 to 23 kJ mol^{-1} in overlapping ranges of dry bulk density.

Molecular dynamics (MD) simulations are routinely used to gain insight into the molecular scale basis of water and solute diffusion in nanoporous materials, including clay interlayers (Sposito et al., 1999; Marry and Turq, 2003; Malikova et al., 2004a,b, 2005; Rotenberg et al., 2007a,b; Kosakowski et al., 2008; Marry et al., 2008, 2011; Mazo et al., 2008; Tournassat et al., 2009; Bourg and Sposito, 2010, 2011a,b; Botan et al., 2011; Pitman and van Duin, 2012). For example, molecular simulations helped reveal that most cations (with the notable exception of the weakly solvated cations K^+, Rb^+, and Cs^+) adsorb on smectite surfaces primarily as outer-sphere surface complexes (Sposito et al., 1999; Bourg and Sposito, 2011a); that ion adsorption on smectite basal surfaces is roughly consistent with the well known triple layer model (Tournassat et al., 2009; Bourg and Sposito, 2011b); and that the primary diffusion pathway of cations in compacted bentonite is through smectite interlayer nanopores (Rotenberg et al., 2007a; Bourg and Sposito, 2010). In principle, this type of simulation can readily predict the T-dependence of water and solute diffusion in clay interlayer nanopores. At present, however, only a handful of MD simulation studies have investigated diffusion in hydrated clay systems at non-ambient temperatures (Malikova et al., 2004a,b; Mazo et al., 2008; Marry et al., 2011; Pitman and van Duin, 2012). This scarcity results from a combination of methodological difficulties, as noted below.

The first difficulty in predicting E_a from MD simulations of clay interlayer nanopores is that simulation results can be highly sensitive to the choice of interatomic potential parameters (the main input of these simulations). Most interatomic potential models are parameterized to describe the properties of a system of interest at a specific temperature, and they sometimes fare poorly when used to simulate the same system at different temperatures (Vega et al., 2005). In the case of clay-water systems, the CLAYFF model, when used in combination with the SPC/E water model, has been successfully tested against the properties of interlayer water at 298 K (Cygan et al., 2004; Bourg and Sposito, 2010; Ferrage et al., 2011). This set of interatomic potential parameters remains almost entirely untested with regard to its ability to accurately predict the properties of clay-water systems at temperatures far beyond ambient conditions—with the exception of a study by Marry et al. (2011) that showed that it predicts the T-dependence of water diffusion in the one-layer hydrate of Na-hectorite more accurately than the widely used clay model of Skipper and coworkers (Skipper et al., 1991, 1995).

A second difficulty is that the D values of fluids and solutes obtained by MD simulation are influenced by the periodic boundary conditions of the simulation cell. This well-known artifact originates from the viscous coupling between the particles and their neighboring image particles, resulting in a reduced D value. In simulations of bulk liquids in a cubic simulation cell of length L, this effect is inversely proportional to the simulation cell size according to the theoretical relation (Placzek et al., 1951; Yeh and Hummer, 2004a,b; Zeebe, 2011):

$$D_s = D_{PBC} + \frac{k_B T \xi}{6\pi\eta L} \tag{3.17}$$

where D_s is the size-corrected diffusion coefficient, D_{PBC} is the diffusion coefficient predicted using periodic boundary conditions, k_B is Boltzmann's constant, $\xi \approx 2.837297$ is the so-called self-term for a

cubic lattice, and η is the viscosity of the medium. The finite-size correction (the last term in Eq. (3.17)) has the same temperature dependence as the ratio $T/\eta(T)$. Therefore, the T-dependence of D_s is not *a priori* equal to the T-dependence of D_{PBC}. For bulk fluids, MD simulation results (i.e., D_{PCB} values) can be converted to D_s values using Eq. (3.17) if the viscosity of the fluid is known. In hydrated clay systems (or in any other heterogeneous system), however, the applicability of Eq. (3.17) is unknown. Therefore, accurate predictions of E_a in clay interlayer nanopores require carrying out multiple simulations of the system of interest with a range of simulation cell sizes, for each temperature of interest. To our knowledge, this has never been carried out for a hydrated clay or any other nanoporous system.

A third difficulty is that the influence of temperature on the initial hydration and swelling of smectite particles is not well characterized. At ambient conditions, stacked smectite layers have stable hydration states in which the interlayer nanopores contain zero, one, two, or three (or, for some smectites, four) statistical monolayers of water molecules (designated hereafter as 0W, 1W, 2W, etc.) with experimental basal spacings d_{001} of 9.5 to 10.1 Å (0W), 12.0 to 12.7 Å (1W), 15.0 to 15.7 Å (2W), 18 to 19 Å (3W) and 21.4 to 22 Å (4W) (Norrish, 1954; Kozaki et al., 1998; Saiyouri et al., 2004; Ferrage et al., 2007, 2011; Svensson and Hansen, 2010; Holmboe et al., 2012). The range of reported values results from the fact that the water content per unit cell depends on the type of smectite (in particular, the magnitude of the negative structural charge and its origin from isomorphic substitutions in either the octahedral or the tetrahedral sheets) and the type of counterion. The values reported above were obtained at ambient temperatures, and their temperature dependence (which may influence the temperature dependence of D) is not known.

A fourth and final significant difficulty in predicting E_a is that the E_a values of interlayer water predicted by MD simulation are sensitive to the vibrational motions of clay structural atoms. Most previous MD simulations of hydrated clay systems treated the clay particles as rigid entities (i.e., the vibrational motion of clay atoms were prevented). Several authors have advocated the use of fully flexible clay lamellae (Kalinichev et al., 2000; Cygan et al., 2004), but data comparing simulations with rigid and flexible clay particles (and testing the results against experimental data) have not previously reported, to our knowledge.

To address the difficulties listed above, we performed a systematic analysis of the sensitivity of the D and E_a values of Na^+ and water in the interlayer nanopores of Na-montmorillonite to key methodological choices—the size of the simulated system (1285 to 61680 atoms), the internal degrees of freedom of the clay particles (from fully rigid to fully flexible)—for a range of temperatures (T = 278 to 353 K) and swelling states (1W, 2W, 3W, and 10W; with basal spacings of 12.4 to 40 Å). We focused particularly on the 2W and 3W hydration states, as X-ray diffraction (XRD) results show that in the KBS-3 concept (the reference concept for Sweden's HLRW repository), the montmorillonite particles in the engineered bentonite barrier form a mixture of the 2W (d_{001} ~15.6 Å) and 3W (d_{001} ~18.9 Å) states in proportions of 35–40% and 60–65% (Holmboe et al., 2012). To keep the size of this study reasonable, we used a single set of interatomic interaction parameters (the SPC/E water model, the CLAYFF force field) that have been found in several studies to accurately predict experimental data on the structure and dynamics of water and ions in smectite interlayer nanopores (Cygan et al., 2004; Bourg and Sposito, 2010; Ferrage et al., 2011; Marry et al., 2011). To test the accuracy of our MD simulation methodology and gain insight into the molecular scale basis of previously reported E_a values, we compared our MD simulation predictions with experimental results on the E_a values of Na^+ and water in compacted water-saturated Na-smectite.

3.2.2 Methodology

All MD simulations were carried out with the code LAMMPS (Plimpton, 1995). Interatomic interactions were modeled with the SPC/E water model (Berendsen et al., 1987) (treated as rigid using the SHAKE algorithm—Ryckaert et al., 1977), the Joung-Cheatham model of the Na^+ ion (Joung and Cheatham, 2008), and the CLAYFF force field (Cygan et al., 2004). CLAYFF assigns partial charges and van der

Waals parameters to each atom type in the clay structure, along with a single physical bond stretch parameter for the structural O-H groups. Smectite particles are periodically layered two-dimensional aluminium phyllosilicates, consisting of an octahedrally coordinated metal-oxide sheet sandwiched between two tetrahedrally coordinated silicate sheets. Smectite particles hold a net negative structural charge because of isomorphic substitution by elements of lower valence in the tetrahedral and octahedral sheets. The smectite modeled in this study was a generic Wyoming type Na-montmorillonite with the unit cell formula $Na_{0.66}[Al_{3.33}Mg_{0.66}][Si_8]O_{20}[OH]_4$ having isomorphic substitutions of Al^{3+} by Mg^{2+} in the octahedral sheet. The montmorillonite lattice structure was based on a triclinic pyrophillite structure taken from the literature (Bickmore et al., 2003) and was subjected to semi-random isomorphic substitutions, outlawing the simultaneous substitutions of neighboring octahedral sites sharing a OH group. Unless otherwise stated, the periodically replicated simulation cells enclosed two unique montmorillonite layers, each consisting of 45 unit cells (9×5 unit cells, extending ~46.6 and ~45.9 Å in the lateral x and y directions, respectively) with Na^+ counterions and different amounts of water molecules in the interlayer nanopores. Production runs were carried out in the *NVT* ensemble (i.e., at fixed composition, volume, and temperature) at 278, 298, 323, and 353 K for a minimum of 5 ns. The production runs were preceded by 0.5 ns of simulation in the *NPT* ensemble (i.e., at fixed composition, pressure, and temperature) at 1 bar, to relax the montmorillonite layers and interlayers in the x,y, and z directions, and 1 ns simulation in the *NVT* ensemble to fully equilibrate the system. Electrostatic and dispersion interactions beyond a cut-off of 12 Å were computed by Ewald summation. To avoid translational drift of the montmorillonite layers (Teppen et al., 1997; Cygan et al., 2004), the simulations in the *NVT* ensemble were performed by independently fixing the center of mass of the montmorillonite layers. For the simulations in the NP_zT ensemble (see, for instance, Figure 3.11), the center of mass was only occasionally fixed in the lateral directions and only for water contents corresponding to > 2W. For lower water contents, lateral translation of the clay sheets was prevented by the high transverse shear moduli of the 1W and 2W state, which have been estimated to be 20 and 2–4 GPa, respectively (Mazo et al., 2008).

Self-diffusion coefficients (D) were calculated from the slope of the mean square displacement $\langle l^2 \rangle$ using the well-known Einstein relation:

$$D = \frac{1}{2n} \lim_{\tau \to \infty} \frac{d\langle l^2 \rangle}{d\tau} \tag{3.18}$$

The infinite time limit in Eq. (3.18) was approximated by using probe time scales of τ = 150 to 250 ps. The D values from the hydrated montmorillonite systems were calculated using n = 2, thus describing the two-dimensional diffusion in the interlayer nanopores. Error bars were estimated at the 95% confidence level, in most cases from five block-averaged values. Size-corrected diffusion coefficient D_s were obtained by extrapolating D versus inverse system size L^{-1} to $1/L = 0$. In the case of bulk liquid water, the Stokes-Einstein Brownian diffusion model (which predicts that $D \propto \eta^{-1}$) was used to estimate a "viscosity-corrected" D_s value (D_{sv}):

$$D_{\mathrm{sv}} = D_{\mathrm{s}} \frac{\eta_{\mathrm{SPC/E}}}{\eta_{\mathrm{exp}}} \tag{3.19}$$

where $\eta_{\mathrm{SPC/E}}$ and η_{exp} are the simulated and measured viscosities of bulk liquid water.

From the D_s values obtained at the different temperatures, activation energies of diffusion (E_a) were calculated based on the slope of the linearized Arrhenius equation, using the standard error in the slope to calculate the 95 % confidence interval.

$$\ln D = \ln D_0 - {E_{\mathrm{a}}}/{RT} \tag{3.20}$$

In order to account for the fact that our interatomic potential parameters underestimated E_a in bulk liquid water by a factor ΔE_a, we calculated a corrected value E_a^* with the relation:

$$E_{\mathrm{a}}^* = E_{\mathrm{a}} + \Delta E_{\mathrm{a}} \tag{3.21}$$

The same correction would have resulted, equivalently, by multiplying all D_s values in clay interlayers by the ratio of the diffusion coefficients of the species of interest in real water *versus* SPC/E water ($D_{0,\mathrm{exp}}/D_{0,s}$) at the temperature of interest.

The shear viscosity of SPC/E water was obtained from a separate set of simulations of 512 water molecules in the *NVT* ensemble at each corresponding temperature, by applying the standard Green-Kubo relations on the auto-correlation function of the stress tensor elements:

$$\eta = \frac{1}{5}\sum_{\alpha,\beta} \lim_{t\to\infty} \frac{V}{k_\mathrm{B}T} \int_0^t \langle p_{\alpha\beta}(t) p_{\alpha\beta}(0)\rangle dt \tag{3.22}$$

where $p_{\alpha\beta}$ are the five anisotropic components of the stress tensor, i.e., the off-diagonal elements p_{xy}, p_{xz}, p_{yz} and the differences between the diagonal elements $(p_{xx}-p_{yy})/2$ and $(p_{yy}-p_{zz})/2$ (Yeh and Hummer, 2004a; Chen et al., 2009; Medina et al., 2011; Tazi et al., 2012). The stress tensor elements were recorded every 2 fs for 10 ns. By comparing different relaxation times for the autocorrelation function (from 1 to 10 ps) and the uncertainties in the block-averaged viscosities at the 95% confidence level, the suitable integration times (t) were found to be, with increasing temperature, 8, 5, 3, and 2 ps, respectively.

3.2.3 Results and Discussion

3.2.3.1 Diffusion in bulk liquid water

In order to establish the influence of clay particles on the D and E_a values of water and sodium, we first determined the ability of our MD simulation methodology to predict water and Na^+ diffusion in bulk liquid water. Figure 3.9 shows the D values of water and Na^+ in bulk liquid water (calculated with Eq. (3.18)) as a function of the reciprocal simulation cell size (L^{-1}) for systems containing 512, 2778, or 22224 water molecules. For each temperature, the solid line shows the linear regression of the plotted data, whereas the dashed line is the best fit obtained with Eq. (3.17) using the viscosity η of SPC/E water (Figure 3.10). By comparing the slope of this extrapolated line with the slope obtained from Eq. (3.17), we find that in the case of Na^+, Eq. (3.17) correctly predicts the size dependence of D. In the case of water (where the D values are much more precisely known because of the larger number of water molecules than Na^+ ions in our simulations), Eq. (3.17) predicts the correct size dependence at ambient temperature (298 K). At lower temperatures, the size dependence predicted by Eq. (3.17) is slightly too small; at higher temperatures, it is too large.

For each temperature, a size-corrected $D_{0,s}$ value was obtained by extrapolating the D versus L^{-1} data in Figure 3.9 to infinite size using linear regression. As shown in Table 3.2, the resulting $D_{0,s}$ values underestimate the E_a values of water and Na^+ in bulk liquid water by $\Delta E_a = 2.8 \pm 0.6$ and 0.7 ± 0.3 kJ/mol, respectively. To determine whether this effect can be explained by the fact that the SPC/E model underestimates the T-dependence of η, we used a relation based on the Stokes-Einstein model of Brownian diffusion (Eq. 3.19) to calculate a "viscosity-corrected" diffusion coefficient $D_{0,sv}$. Our results show that viscosity alone cannot fully explain the disagreement between predicted and measured E_a values.

Our results on the viscosity of SPC/E water are consistent with previously reported data (Medina et al., 2011). The slight difference with the results of Medina et al. (2011) may arise from the fact that we did not set the density of the SPC/E water to the experimental water density. This was necessary because we did not impose the density of water in the simulations of hydrated montmorillonite. As seen in Figure 3.10, the SPC/E water model overestimates the density of liquid water by up to 1.8%.

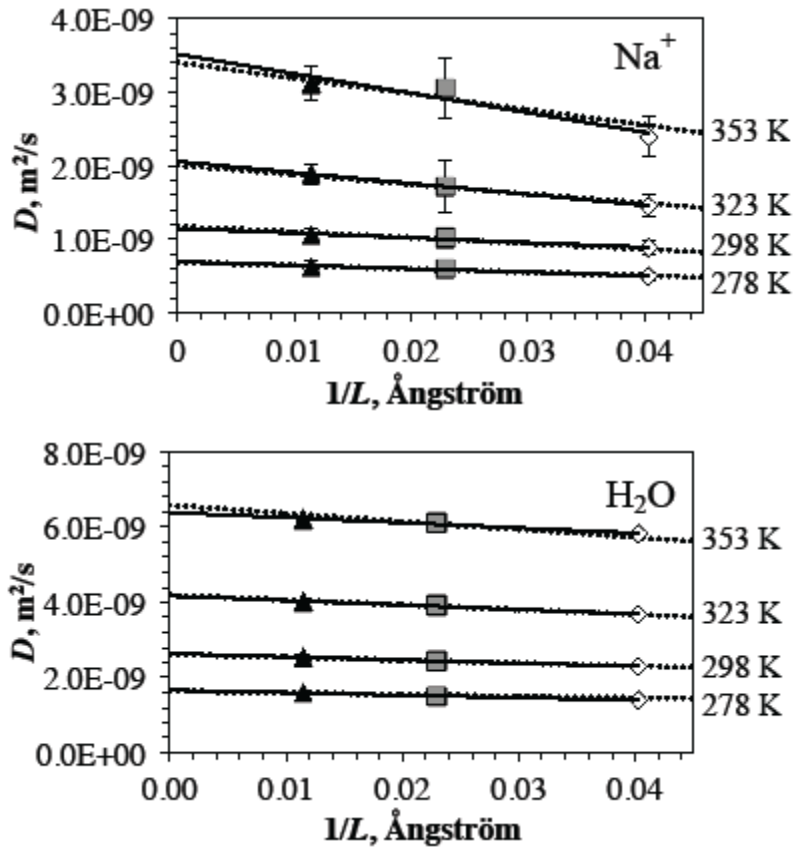

Figure 3.9. D values of Na^+ (top) and water (bottom) as a function of inverse simulation cell size (for simulations with 512, 8334, or 22224 water molecules) at different temperatures. The size-corrected diffusion coefficient $D_{0,s}$ is determined by linear regression (black line) to $1/L = 0$. The dashed line shows the best fit obtained with Eq. (3.17) using the viscosity of SPC/E water.

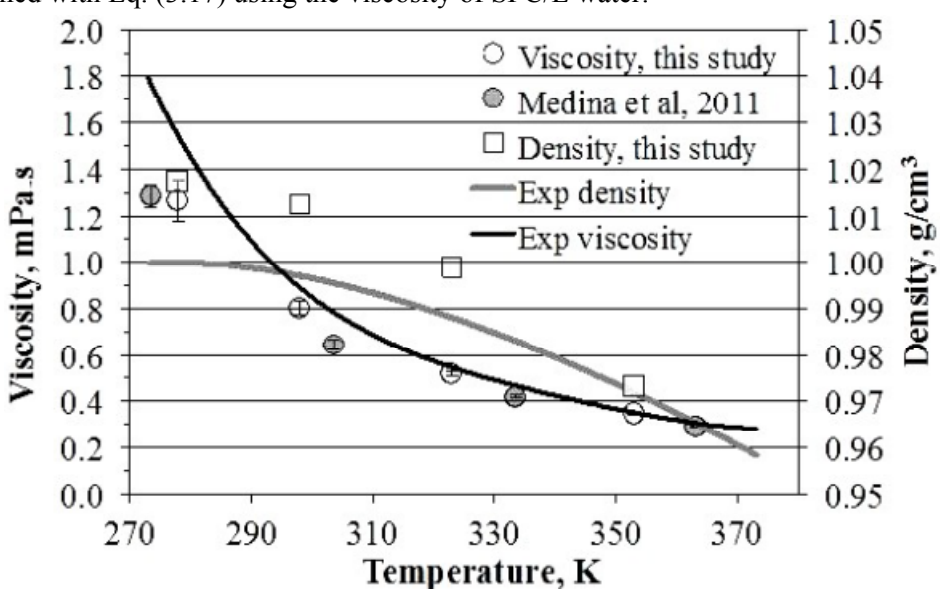

Figure 3.10. Comparison of the shear viscosity of the SPC/E water model, from this study (white circles) and from Medina et al. (2011) (gray circles), with the experimental viscosity of water (Lide, 2012) (black line). Right hand axis indicates our simulated (white squares) and the experimental (gray line) water density, respectively.

Table 3.2. Shear viscosity of water and self-diffusion coefficients of Na^+ and water in bulk liquid water. Predicted D values are shown for simulations with 512 water molecules (D), after correction for the finite-size effect ($D_{0,s}$), and after correction for both size and viscosity ($D_{0,sv}$). The subscript 'exp' denotes experimental values (Talekar, 1977; Holz et al., 2000).

	Viscosity [mPa·s]		Na^+ [10^{-9} m²/s]				H_2O [10^{-9} m²/s]			
T [K]	$\eta_{SPC/E}$	η_{exp}	D (24Å)	$D_{0,s}$	$D_{0,sv}$	$D_{0,exp}$	D (24Å)	$D_{0,s}$	$D_{0,sv}$	$D_{0,exp}$
278	1.266±0.087	1.514	0.50±0.06	0.69±0.03	0.56±0.02	0.752	1.40±0.01	1.66±0.02	1.39±0.02	1.303
298	0.804±0.031	0.891	0.88±0.10	1.15±0.04	1.03±0.03	1.335	2.29±0.01	2.63±0.01	2.37±0.01	2.299
323	0.520±0.008	0.548	1.45±0.15	2.06±0.01	1.95±0.01	2.314	3.68±0.04	4.17±0.04	3.96±0.04	3.956
353	0.345±0.006	0.355	2.39±0.27	3.51±0.24	3.41±0.24	3.859	5.83±0.06	6.39±0.06	6.21±0.04	6.557

3.2.3.2 Basal spacing and water content of clay nanopores

As noted in the introduction, the basal spacing and water content of smectite are not precisely known. For example, previous MD simulation studies of smectite interlayer nanopores used either 4 (Kosakowski et al., 2008), 4.5 (Marry and Turq, 2003; Malikova et al., 2005), or 5 (Bourg and Sposito, 2010) water molecules per unit cell per hydration layer. Our tests with 4, 5, or 6 water molecules per unit cell per hydrate layer (not shown) indicated that the D values of interlayer water and Na^+ are highly sensitive to the water content of the interlayer: an increase in water content from 4 to 5 or from 5 to 6 water molecules per unit cell and hydration layer caused the D values of interlayer water and Na^+ to increase by on average 15–20%, decreasing with increasing temperature. A small but significant decrease in the E_a of diffusion was also found (not shown) as well as a substantial increase in d_{001} with increasing water content. Our tests also showed that the unit cell volume of Na-montmorillonite increases slightly in the temperature range from 273 to 353 K, primarily because of the T-dependence of the d-spacing: from 273 to 353 K, d_{001} increased by about 1 Å (as shown by the black crosses in Figure 3.3 in the case of systems with 12, 15, or 18 water molecules per unit cell), whereas the unit cell area ab increased by only 0.1 Å^2.

The comparison between experimental (Holmboe et al., 2012) and simulated d_{001} data in Figure 3.11 shows that each statistical water monolayer contains about 5 water molecules per montmorillonite unit cell. This finding is supported by the fact that the density of interlayer water (calculated from the d_{001} value, the effective montmorillonite layer thickness, and the unit cell area), when plotted as a function of water content, oscillates with a periodicity of almost exactly 5 water molecules per unit cell (Figure 3.11). The effective montmorillonite thickness (9.25 Å) was obtained by extrapolating the slope of d_{001} in the linear regime at high water contents to the fully dehydrated state. Interestingly, the unit cell area increased by about 1% with decreasing water content. The density maxima of interlayer water (Figure 3.11) are consistent with the density of bulk liquid water shown in Figure 3.9. Similar simulations with other types of smectites (not shown) indicate that this is not always the case for the 1W state.

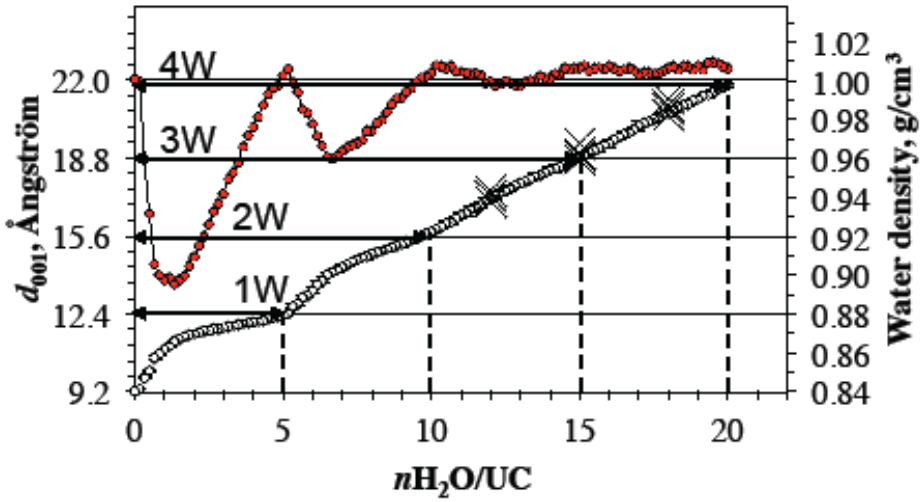

Figure 3.11. Basal spacing d_{001} (open circles) and interlayer water density (filled circles) as a function of the number of water molecules per unit cell (UC) in a MD simulation where the number of water molecules was slowly decreased by removing one water molecule every 40 ps (NP_zT ensemble). Experimental data on the d_{001}-values of the 1W, 2W, 3W, and 4W hydrate states of montmorillonite (Holmboe et al., 2012) are shown as black horizontal arrows. The precision of predicted d_{001} values is roughly 0.1 Å. Black crosses show the d_{001} values predicted from NP_zT ensemble simulations with 12, 15, or 18 water molecules per unit cell at T = 278 to 353 K.

3.2.3.3 Simulation cell size dependence of D in MD simulations of clay nanopores

In order to determine the size dependence of D in MD simulations of montmorillonite nanopores, a set of simulations of the 2W and 3W hydration states was conducted using nearly cubical simulation cells, with simulation cell sizes ranging from 24.3 to 86 Å (1285 to 61680 atoms; Figure 3.12). Interestingly, and contrary to the behavior observed in simulations of bulk liquid water (Figure 3.9), the D values of Na^+ and water in clay nanopores had no significant size dependence. This is illustrated in Figure 3.13 in the case of the 3W hydration state for T = 273 to 353 K. Similar results were obtained for the 2W hydration state, as well as for the 3W hydration state using fully rigid clay layers (not shown). A few of the datasets on D vs. $1/L$ (for instance for water at 353K in Figure 3.13) could be consistent with a size dependence of D, but the absence of a consistent trend between simulations at different temperatures or with different pore sizes indicates that this is likely caused by the use of different individual montmorillonite layers, each having a different configuration of isomorphic substitutions. According to Eq. (3.17), the invariance of D with $1/L$ indicates that the effective viscosity of the clay-water system is much higher than that of bulk liquid water or, equivalently, that viscous interactions in the clay-water system are much more short-ranged than in bulk liquid water. The absence of a size dependence of D in our simulations of the 2W and 3W hydration states would likely also be observed in simulations of the 1W hydration state. Simulations of larger pores (such as the 10W hydrate) may have a system size dependence intermediate between that observed in the 3W hydrate and in bulk liquid water. Hereafter, we use systems with two clay layers (90 unit cells) to probe the 1W, 2W, and 3W hydration state, and a system with one clay layer (45 unit cells) to probe the 10W hydration state (Figure 3.14).

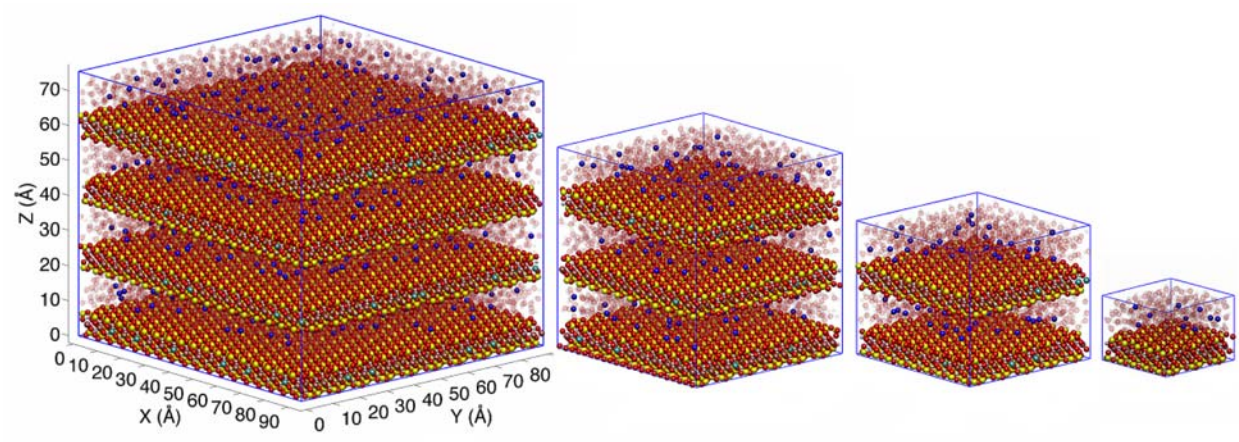

Figure 3.12. MD simulation snapshots showing the four different simulation cells that were used to study the 3W hydrate of montmorillonite. From left to right, the systems contained 61680, 16962, 7710 and 1285 atoms and {18×10×4}, {11×6×3}, {9×5×2} and {5×3×1} unit cells in the {*a*×*b*×*c*} directions, respectively.

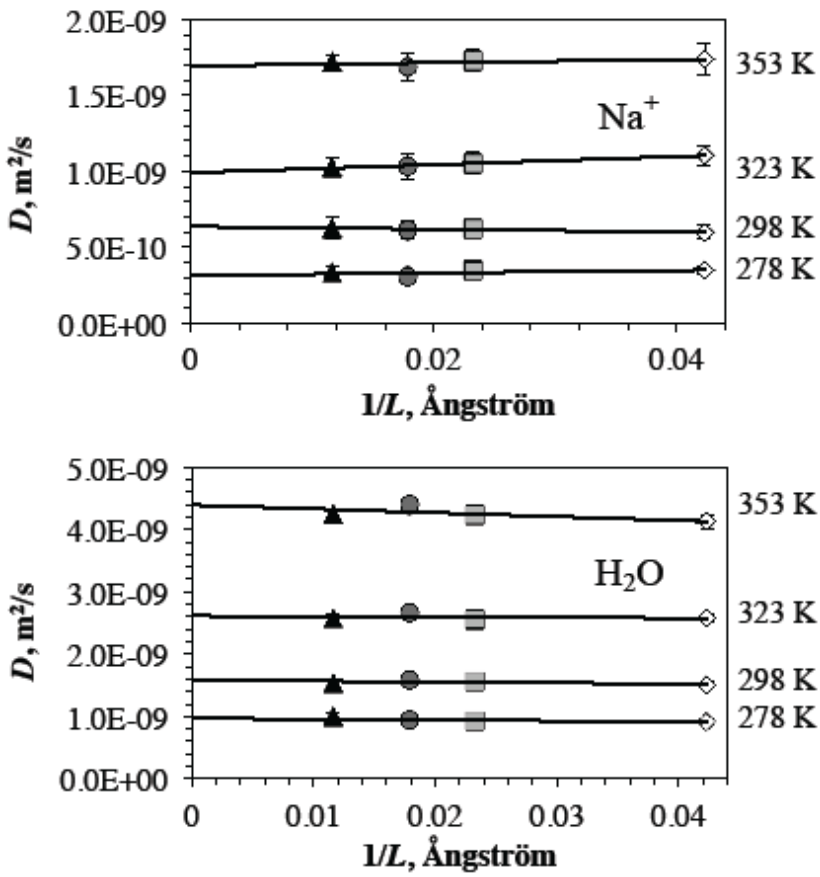

Figure 3.13. *D* values of Na^+ (top) and water (bottom) as a function of temperature and the mean inverse simulation cell size 1/*L*.

3.2.3.4 Influence of clay layer rigidity

In order to investigate the influence of the vibrational motions of clay atoms on the structure and dynamics of interlayer water and solutes, simulations were carried out with clay layers that were either fully rigid, fully flexible, or semi-flexible. For the last state, either all atoms in the clay layer were kept

fixed except the hydroxyl hydrogens ("flex O-H"), or vice versa ("rigid O-H"). Our results show that clay-layer rigidity has no significant influence on the one-dimensional atomic density profiles of interlayer species along the direction normal to the clay surfaces (representative density profiles are shown in Figure 3.14 in the case of the fully flexible systems) or on the coordination of interlayer species. In all systems having rigid or semi-flexible clay layers, small and localized irregularities were found in two-dimensional density maps displaying the preferential locations of water oxygen and hydrogen atoms above the clay siloxane surface. These artifacts stem from the fact that we carried out all equilibration runs using fully flexible clay particles, as described in Section 3.2.2, which unavoidably resulted in small irregularities in the coordinates of structural clay atoms in the production runs that used rigid or semi-flexible structures. To determine the influence of this effect on the D values of interlayer species, we conducted a comparative set of simulations of the 3W hydration state equilibrated in two different ways, using either our default methodology or an optimized clay structure for the production run, in which the positions of all structural clay atoms where fixed to their median positions during the final 100 ps of the equilibration run. The second equilibration method yielded two-dimensional density maps with no localized irregularities. This second equilibration method yielded one-dimensional density profiles in the direction normal to the clay surface that were slightly narrower than those obtained with the default methodology, indicating that structural disorder arising from the vibrational motions of structural clay atoms causes a slight broadening of the density distribution features of nanopore species. The differences in the D values of Na^+ and water obtained with the two methods of equilibration were found to be small and often insignificant, especially for the systems simulated with a fully rigid clay layer.

The normalized $D/D_{0,s}$ values of Na^+ and water for the same systems at the different degrees of clay-layer rigidity are shown in Figure 3.15. For all hydration states and temperatures investigated, simulations with fully flexible clay structures consistently resulted in higher D values for both Na^+ and water in the interlayer nanopores compared to simulations with fully rigid clay particles, regardless of equilibration method. For the two types of systems with semi-flexible clay layers, the D values of Na^+ and water were indifferent from each other and intermediate between the D values obtained with fully rigid or fully flexible clay structures. This reveals that the influence of clay flexibility arises roughly equally from the motions of structural H atoms and from the motions of all other atoms.

The influence of clay vibrational motions on interlayer D values increases sharply as water content decreases, demonstrating the short-ranged nature of this effect. For instance, for the 1W hydration state, the D value of Na^+ in contact with a fully flexible clay particle was higher by a factor of four compared to the corresponding value in contact with a fully rigid clay particle. For the 3W hydration state, the difference was approximately 25%, and for the 10W hydration state, no significant difference was detected. These findings demonstrate the importance of using a flexible clay structure when studying diffusion in clay nanopores. Although no significant effect was found at the highest hydration state for Na^+ or water, this may not be true for other types of counter-ions that predominantly form inner-sphere surface complexes, such as K^+ or Cs^+.

Table 3.3 summarizes the D values of Na^+ and water for each hydration state and temperature modeled with fully flexible clay layers (along with the ratio $D_{0,\mathrm{exp}}/D_{0,\mathrm{s}}$ for each species at each temperature). These pore scale diffusion coefficients are not directly equivalent to the "apparent" diffusion coefficient obtained from macroscopic scale diffusion experiments (Marry and Turq, 2003; Kosakowski et al., 2008; Bourg and Sposito, 2010). This is because our MD simulations inherently cannot describe pore-network-scale geometric effects such as tortuosity and pore connectivity. Nevertheless, macroscopic scale diffusion coefficients can in principle be estimated from our predicted pore scale diffusion coefficients if the relevant microstructural parameters are known (Marry et al., 2003; Gonzalez-Sánchez et al., 2009; Bourg and Sposito, 2010; Churakov and Gimmi, 2011).

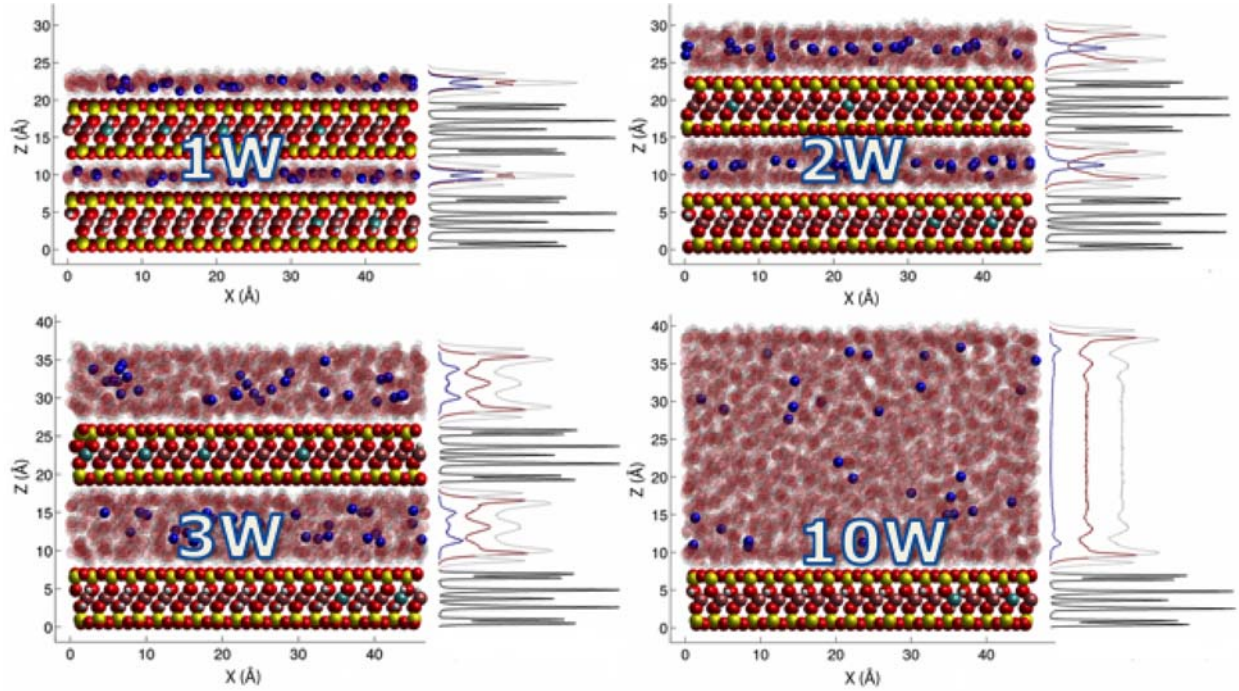

Figure 3.14. MD simulation snapshots showing the 1W, 2W, 3W and the 10W hydration states (with d_{001} = 12.4, 15.6, 18.8, and 40.7 Å, respectively) at 298 K and the corresponding atomic density profiles along z-direction for Na^+ (blue), H_{water} (light gray), O_{water} (red) and montmorillonite (black).

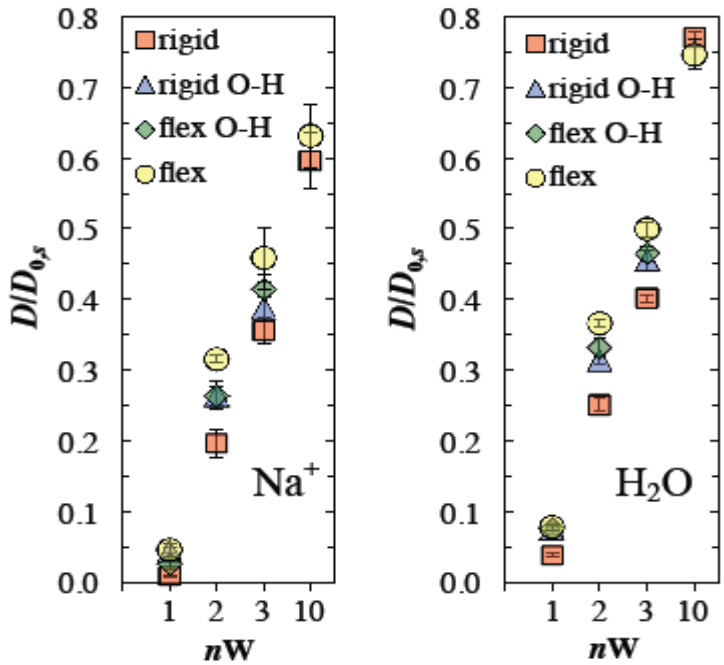

Figure 3.15. Normalized self-diffusion coefficients of Na^+ (left) and water (right) as a function of clay layer rigidity and hydration state (1W, 2W, 3W, or 10W) at 298 K. The normalization of D was made with regard to the corresponding size corrected $D_{0,s}$ value from Table 3.2. The clay layer rigidity was varied from fully rigid (red squares) to fully flexible (yellow circles). In the two semi-flexible states, either all structural clay atoms were kept fixed except the bonded hydroxyl hydrogen (green diamonds) or vice versa (blue triangles).

Table 3.3. Two-dimensional self-diffusion coefficients of Na^+ and water in clay interlayer nanopores in systems with fully flexible clay sheets and five H_2O molecules per unit cell per hydrate layer. The last column shows the correction factor that can be applied to account for the discrepancy between measured and predicted diffusion coefficients in bulk liquid water. The last row shows the E_a values of Na^+ and water in the clay interlayer nanopores at different hydration states, corrected for the difference in E_a values between bulk liquid SPC/E water and real water.

	D_{Na} (10^{-9} m^2/s)				
T (K)	1W	2W	3W	10W	$D_{0,exp}/D_{0,s}$
278	0.025±0.003	0.15±0.01	0. 28±0.03	0.44±0.04	1.085
298	0.053±0.010	0.36±0.01	0.53±0.05	0.77±0.15	1.165
323	0.109±0.022	0.65±0.07	0.79±0.11	1.29±0.15	1.126
353	0.217±0.017	1.13±0.14	1.43±0.10	1.90±0.20	1.099
E_a* (kJ/mol)	24.3±1.1	22.0±1.0	18.0±0.8	16.7±1.1	
	D_{H2O} (10^{-9} m^2/s)				
T (K)	1W	2W	3W	10W	$D_{0,exp}/D_{0,s}$
278	0.113±0.006	0.47±0.01	0.75±0.02	1.15±0.03	0.783
298	0.205±0.011	0.96±0.01	1.31±0.03	1.91±0.02	0.873
323	0.385±0.021	1.68±0.06	2.19±0.07	3.19±0.04	0.949
353	0.789±0.048	2.82±0.15	3.63±0.02	5.09±0.08	1.030
E_a* (kJ/mol)	23.7±0.4	22.1±0.6	19.9±0.3	19.0±0.3	

3.2.3.5 Comparison with measured E_a values in compacted Na-montmorillonite

As noted in the introduction, most interatomic potentials used in MD simulations were parameterized to describe the system of interest at a specific temperature, and they sometimes fare poorly when applied at very different temperatures. To account for this, we report E_a values that were calculated from our MD simulations of clay interlayer nanopores, then corrected for the difference (ΔE_a) between measured and predicted E_a values in bulk liquid water (Table 3.3). Based on the experimental results of Talekar (1977) and Holz et al. (2000) (E_a = 18.4 ± 0.3 and 17.4 ± 0.2 kJ/mol for Na^+ and water in the temperature range of our study), we used ΔE_a = 0.7 ± 0.3 and 2.8 ± 0.6 kJ/mol for Na^+ and water, respectively.

In Figure 3.16, we compare our predicted E_a values with macroscopic and pore scale experimental data on E_a in water-saturated Na-smectite. Most experimental values were reported as a function of the dry bulk density (ρ_b) of the porous medium. Therefore, we used recent XRD data to estimate the range of ρ_b values in which water-saturated smectite forms the 1W, 2W, 3W, or ~10W hydrates. As shown in Figure 3.16, our MD simulation predictions are consistent with most experimental results. In the case of Na^+, our predicted E_a values are equal to or slightly lower than the experimental results of Kozaki et al. (2005). In the case of H_2O, our predicted E_a values are consistent with the results of Marry et al. (2011) and Suzuki et al. (2004), and with half of the data reported by Nakazawa et al. (1999), while being ~2 to 3 kJ mol^{-1} higher than the results of Gonzalez-Sánchez et al. (2009) and Nakashima (2000). Our results predict a ~6 kJ mol^{-1} increase in the E_a values of Na^+ and water with increasing clay-water ratio (from bulk liquid water to the 1W hydrate). Finally, our results show that Na^+ has a higher E_a value in the so-called *crystalline hydrates* (1W, 2W, 3W states) and a lower value in the *osmotic hydrates* (such as the 10W state) than in bulk liquid water, as hypothesized by Kozaki et al. (2005).

The different studies compiled in Figure 3.16 are not perfectly equivalent, because they used different smectite minerals with small differences in the magnitude and distribution of their negative structural charge. As noted in Section 3.2.2, the smectite used in this study was a Wyoming-type montmorillonite

with a structural charge of -0.66 e per unit cell arising exclusively from isomorphic substitutions in the octahedral layer. The smectite used by Kozaki et al. (2005), for example, was the Kunipia-F montmorillonite (a reference montmorillonite of the Japanese radioactive waste management program), which has a larger negative structural charge (-0.84 e per unit cell) and has isomorphic substitutions in both the octahedral and tetrahedral layers. Our preliminary results modeling a generic Kunipia-F type montmorillonite with the methodology developed in this study suggest that the additional negative structural charge in the tetrahedral sheet results in a significant degree of inner-sphere surface complexation of interlayer Na^+ ions, which may lead to higher E_a values. This matter will be the investigated during the end of FY13.

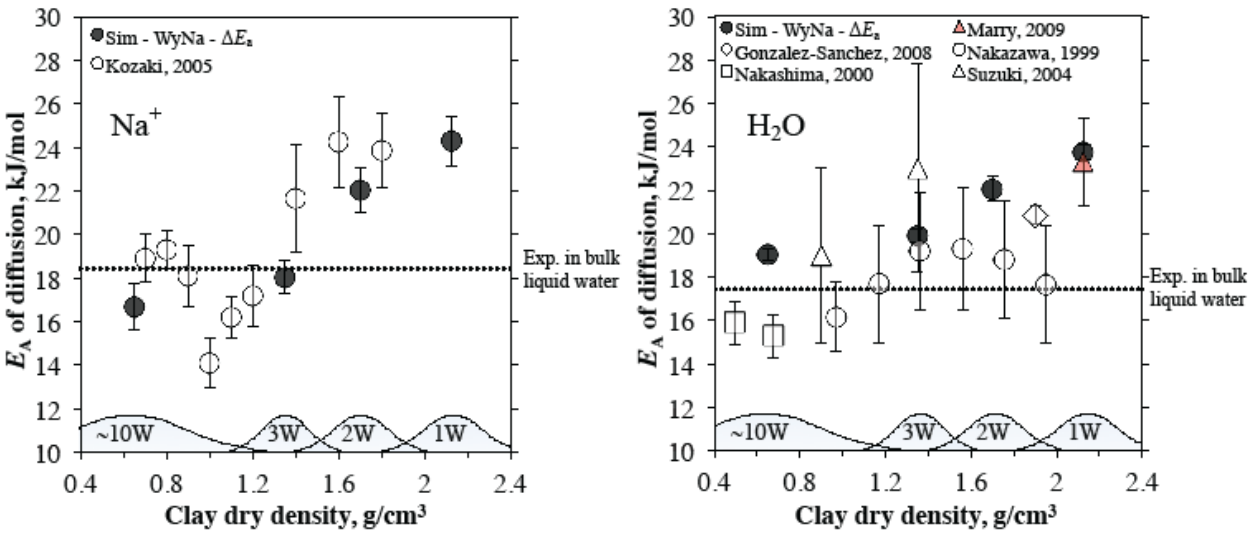

Figure 3.16. Activation energy of diffusion of Na^+ and water in water-saturated Na-smectite, plotted as a function of dry bulk density. Our MD simulation results are shown as black circles. Other symbols represent macroscopic (white symbols) or pore scale (red symbols) experimental results. Error bars represent the standard error in the slope of the linearized Arrhenius plot. Dashed horizontal lines indicate the measured E_a values of diffusion of Na^+ and water in bulk liquid water (Talekar, 1977; Holz et al., 2000). Approximate regions of predominance of each hydration state (shown schematically in the lower part of each figure) were estimated from X-ray diffraction data (Holmboe et al., 2012).

3.2.4 Summary

Using a new capability for a dynamic electrical double layer (EDL) thickness, we simulated the effects of the diffusive propagation of a ionic strength front on EDL porosity and transport. The simulations demonstrate that the changes in EDL thickness as a function of ionic strength may in fact have an opposite effect to that resulting from clay swelling. In addition, we were able to implement the Mean Electrostatic Model for the EDL with and without Stern layer sorption. A full treatment of these layers is more complicated in the context of the Poisson-Boltzmann equation and will be the focus of much of the work for the remainder of FY13. The ionic strength dependent EDL model was then used to simulate anion and uncharged species out-diffusion from a borehole in the DR-A experiment at the Mont Terri experimental facility in Switzerland. The key accomplishment was the ability to capture both behaviors (uncharged and charged species) with the same model. In addition, we completed much of the necessary software changes needed to couple the reaction portion of CrunchEDL with the general purpose PDE simulator Comsol. This will provide the basis for both pore scale electrostatic flow and transport, as well as larger repository scale simulations.

We determined the influence of water content, temperature, simulation cell size, and clay-layer flexibility on MD simulation predictions of Na^+ and water diffusion in the montmorillonite interlayer nanopores. Our simulations led to the development of a robust MD simulation methodology that correctly predicts

the temperature dependence of Na^+ and water diffusion in bulk liquid water and in the interlayer nanopores of hydrated montmorillonite. Our results show that MD simulations can help to extrapolate existing diffusion measurements to the high temperatures that occur in the near field of high-level radioactive waste repositories, while also providing molecular scale insights into the predominant diffusion pathways of water and solutes in the EBS. In particular, our results support the view that the predominant diffusion pathway of Na^+ in compacted water-saturated bentonite shifts from the osmotic hydrate to the crystalline (3- and 2-layer) hydrates with increasing dry bulk density.

4. EXPERIMENTAL STUDIES ON REACTIVE DIFFUSIVE TRANSPORT

The long-term management of nuclear waste repositories requires reliable predictions of uranium(VI) diffusion through waste containment barriers, such as compacted bentonite. Uranium diffusion coefficients can be affected by metal solution speciation and chemical solution conditions, such as pH and inorganic ligand concentrations, as well as a variety of metal-mineral surface interactions. Furthermore, specifically for clays, metal diffusion processes are influenced by: (1) the electrical charge of the diffusing solute, (2) the degree of compaction, and (3) the electrical double layer structure at the clay/water interface. Most currently available uranium diffusion models do not specifically include the expected changes in metal diffusion rates due to these variations. However, we believe that a "de-coupling" of parameters and processes is necessary to ensure an accurate prediction of apparent diffusion rates under the chemical gradients expected within engineered barrier systems.

In order to achieve this goal, we first completed a detailed theoretical analysis of the potential impacts of solution chemistry on various types of uranium diffusion coefficients and clay (surface) characteristics. In addition, uranium(VI)-montmorillonite batch sorption equilibrium experiments were performed to characterize uranium sorption as a function of chemical solution conditions, and to provide data sets for the development of a surface complexation model. Last, lab-scale diffusion experiments were designed, and the reactive diffusive transport of calcium (an important element driving uranium solution speciation) and uranium(VI) were evaluated experimentally and/or in predictive model calculations.

4.1 Background

4.1.1 Relevance

The long-term management of nuclear waste repositories requires reliable predictions of contaminant transport in the subsurface at chemical conditions varying over time and space. This includes an evaluation of radionuclide mobility through waste containment barriers in engineered barrier systems (EBS) close to the source term. Compacted bentonite has been proposed as a backfill material in EBS because of its low permeability (Pusch, 1992; Bourg, et al., 2003; Kim et al., 1993) and strong sorptive properties (Eriksen et al., 1999; Ochs et al., 2001). The limited permeability of bentonite is at least partially the result of its low porosity and the swelling of Na-montmorillonite, its major component, in water. Due to these characteristics, the transport of contaminants through bentonite layers is expected to be limited and dominated by diffusion (Ochs et al., 2001; Madsen, 1998; Bourg et al., 2007).

However, the state of knowledge with respect to diffusion-driven flux shows that there are large differences in diffusion behavior between various radionuclides, e.g., between halides (^{36}Cl, ^{129}I) and actinides ($^{238,235}U$, ^{237}Np, ^{232}Th). The differing behaviors are a result of the two major processes that have important effects on macroscopic diffusive transport, i.e., molecular diffusion and sorption. Hence, laboratory sorption and diffusion studies are an important component for the design of waste containment barriers (Shackelford, 1991) and the calibration of diffusion-based transport models. As the basis of nuclear fuel, uranium is one of the primary elements to be considered in environmental risk assessments

for nuclear waste repositories, with U(VI) representing its most mobile oxidation state. Therefore, a fundamental understanding of uranium(VI) diffusion through bentonite is essential.

In current models for radionuclide diffusion through bentonite in an EBS, the apparent and effective diffusion coefficients are linked through a K_d value, a sorption partitioning coefficient (or another type of sorption isotherm). This parameter is often believed to be a constant value for a particular radionuclide and solid-phase sample. In the case of U(VI), however, this is unlikely to be true because of the very high sensitivity of the K_d value to pH, as well as bicarbonate and calcium concentrations. By extension to the aqueous chemistry of other actinides, we can expect the K_d values of Np, Am, and Pu to also be sensitive to pH and bicarbonate concentrations. It should be noted that waste forms, and possibly concrete in the vicinity of an EBS, are likely to create gradients in these chemical variables (pH, HCO_3^-, Ca^{2+}) within the EBS (Figure 4.1). Therefore, it is important to develop conceptual models that can describe U(VI) diffusion as a function of chemical solution conditions. Specifically, predictive models need to independently take into account the effects of chemical solution conditions on (1) molecular diffusion, (2) metal sorption reactions and (3) clay surface properties.

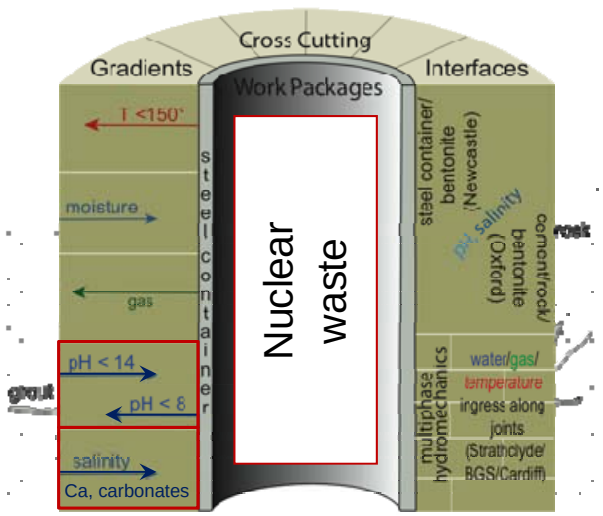

http://www.eng.ox.ac.uk/about-us/jobs/fp/THMC.png/image_preview

Figure 4.1. Expected gradients across the EBS.

4.1.2 Effects of Chemical Solution Conditions on U(VI) Diffusion Coefficients

In the following, we present our theoretical analysis of the potential impacts of solution chemistry on various types of uranium diffusion coefficients and clay (surface) characteristics (Tinnacher and Davis, 2013). First, we will provide an overview of various types of diffusion coefficients and discuss the influence of chemical solution conditions on these parameters as they are relevant for U(VI) diffusion (Table 4.1). We will begin with the simplest case, molecular diffusion in a liquid, and then increase the level of complexity, taking into account more and more effects of the porous media. It is important to note that, along this discussion from simple to more complex coefficients, the impacts of chemical solution conditions on diffusion coefficients are additive.

Table 4.1. Effects of solution chemistry on diffusion coefficients

Diffusion coefficient	Equation	Diffusion in	Impact of solution chemistry on
Molecular diffusion coefficient	$D_0 = \frac{k_B T}{6\pi\mu R_0}$	Dilute aqueous solution	• Molecular size of solute species (R_o) • Solute concentration
Pore diffusion coefficient	$D_p = \frac{\delta}{\tau^2} D_0$	Pore water	• Clay constrictivity (δ) • Clay tortuosity (τ^2)
Effective diffusion coefficient	$D_e = \varepsilon D_p$	Overall porous media	Diffusion-accessible porosity (ε), e.g. for anions
Apparent diffusion coefficient	$D_a = \frac{D_e}{\varepsilon + \rho K_d}$	Overall porous media including sorption	Sorption behavior (K_d) due to changes in: • Solution speciation • Main sorption processes

Molecular diffusion is defined as solute transport resulting from the random thermal motion of molecules in solution (Selim and Amacher, 1997). In liquids, the Stokes-Einstein equation is the most common basis for the estimation of diffusion coefficients in free aqueous solution, also known as molecular diffusion coefficients (D_0) (Cussler, 1997):

$$D_0 = \frac{k_B T}{f} = \frac{k_B T}{6\pi\mu R_0} \tag{4.1}$$

where f is the friction coefficient of the solute, k_B is Boltzmann's constant, T is temperature, μ is the solvent viscosity, and R_0 is the solute radius.

Molecular diffusion coefficients typically vary with solute concentration, and decrease with increasing solute radii. If the solute of interest is hydrated or solvated in any way, then the "diffusion-relevant" radius is represented by the solute-solvent complex, and not the solute itself (Cussler, 1997). For uranium, changes in chemical solution speciation and U(VI) complexation with inorganic ligands, such as carbonates, can change the molecular size of aqueous species, as well as their hydration properties and the water exchange kinetics with the hydration sphere (Kerisit and Liu, 2010). Current results from potential-based molecular dynamics simulations suggest that these changes lead to differences in molecular diffusion coefficients for various U(VI) solution species, e.g., UO_2^{2+} and $UO_2(CO_3)_3^{4-}$ (Kerisit and Liu, 2010). However, molecular diffusion rates of the fastest and slowest U(VI) species vary by less than a factor of 2, which will lead to only minor changes in overall U(VI) diffusion rates in porous media relative to other effects associated with metal-solid interactions.

In porous media, migrating solutes experience tortuous pathways and potentially changing diffusion volumes over increased transport distances. This is taken into account with the pore diffusion coefficient (D_p), which is defined as

$$D_p = \frac{\delta}{\tau^2} D_0 \tag{4.2}$$

The constructivity factor (δ) is a measure of the diffusion volume along the diffusion pathway (Figure 4.2), with $\delta < 1$ for decreasing and $\delta > 1$ for increasing volumes along the pathway. For saturated bentonite, the diffusion volume and clay porosity are typically assumed to be constant throughout the sample, resulting in $\delta = 1$ (Holmboe, 2009). The tortuosity (τ^2) is a dimensionless, geometric parameter, or a 'winding factor' (≥1) (Holmboe, 2009), representing the average length of diffusion paths linking the system boundaries relative to the distance ∂x (Figure 4.2). As described in detail below, τ^2 is a function of various (chemical) system conditions that can influence clay characteristics. Hence, overall, the pore

diffusion coefficient (D_p) is subject to all chemical changes affecting molecular diffusion and clay tortuosity.

Further increasing the degree of complexity, the effective diffusion coefficient (D_e) represents a measure of the diffusive flux within the porous media while taking into account the porosity (ε) of the media.

$$D_e = \varepsilon D_p \tag{4.3}$$

Hence, according to Fick's first law of diffusion, the diffusive flux (J) of a solute under steady-state conditions is described by

$$J = -D_e \frac{\partial C}{\partial x} \tag{4.4}$$

In clays, chemical solution conditions can change the diffusion-accessible porosity, e.g. for anions, as described in further detail below. Therefore, overall chemical solution conditions can affect effective diffusion coefficients owing to their impact on molecular diffusion coefficients and clay properties, such as τ^2 and ε.

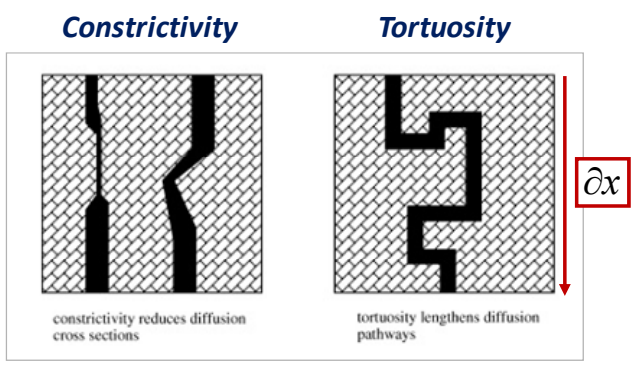

Figure 4.2. Visualization of constrictivity and tortuosity (Van Loon and Soler, 2004).

Last, for reactive solutes, such as uranium, metal interactions with the mineral surface in the pore environment have to be expected over the course of diffusion-dominated metal transport. As a result, some researchers have proposed the use of some form of an apparent diffusion coefficient (Maes et al., 2002; Tokunaga et al., 2004), which further extends the effective diffusion coefficient to directly include metal sorption or ion exchange reactions. The apparent diffusion coefficient (D_a) represents the overall macroscopic diffusion rate, and is included in Fick's second law of diffusion describing the solute concentration change in a (porous) volume element under transient conditions.

$$\frac{\partial C}{\partial t} = D_a \frac{\partial^2 C}{\partial x^2} \tag{4.5}$$

Apparent and effective diffusion coefficients are linked through the rock capacity factor (α) with

$$D_a = \frac{D_e}{\alpha} \tag{4.6}$$

where α is defined as

$$\alpha = \varepsilon + \rho K_d \tag{4.7}$$

In Eq. 4.7, ρ represents the dry bulk density of the mineral and K_d the sorption distribution coefficient. For non-sorbing species, K_d is equal to zero, and the rock capacity factor equals clay porosity. For sorbing solutes, the K_d value represents the slope of a linear sorption isotherm; however, non-linear isotherms can also be incorporated into apparent diffusion coefficients (Bai et al., 2009).

Chemical solution conditions and metal speciation are known to affect uranium sorption behavior and K_d values in clays (Bradbury and Bayens, 2011; Fox et al., 2006; Davis et al., 2004). Hence, in addition to the effects discussed for effective diffusion coefficients above, D_a is also impacted by chemical effects on U(VI) sorption parameters. Furthermore, Muurinen (1990) reported changes in apparent diffusion coefficients due to differences in uranium speciation, and argued that different species appear to follow different diffusion mechanisms.

While U(VI)-clay interactions are important to consider, their direct incorporation into diffusion coefficients in the form of K_d values or non-linear sorption isotherms appears problematic for a variety of reasons. First, the overall values of apparent diffusion coefficients become inherently dependent and sensitive to the correct values of α. As a result, it becomes meaningless to report values of apparent diffusion coefficients of reactive solutes without a characterization of their sorption characteristics (Shackelford, 1991). Second, sorption isotherms are inherently dependent on the sorption characteristics of the solid phase, and the concentrations and chemical solution speciation of the solute. While they provide good estimates for specific system conditions, they do not allow for any predictions of contaminant transport under conditions changing over time and space. For example, the application of linear sorption isotherms for the simulation of uranium diffusion in London clay is very limited (Brown et al., 1991). Uranium retardation was shown to be highly dependent on uranium solution concentrations, which varied substantially over space, even in a small, well-controlled lab system (9 mm clay sample, pH=8).

Therefore, an independent treatment of sorption terms and diffusion mass transfer appears to be a better approach. However, at this point, this strategy has been applied less frequently (Bai et al., 2009; Liu et al., 2010).

4.1.3 Influence of Solution Chemistry on Clay (Surface) Properties

Chemical solution conditions can affect the structural properties of clays, in terms of diffusion-accessible porosity and clay tortuosity, the dominant pathways of solute diffusion, as well as the reactive surface sites available and relevant for U(VI) sorption and ion exchange reactions (Figure 4.3). More specifically, diffusion processes are known to be influenced by: (1) the electrical charge of the diffusing solute, (2) the degree of compaction, and (3) the electrical double layer structure at the clay-water interface. In the following, we will briefly discuss these interactions in the context of montmorillonite and bentonite (Tinnacher and Davis, 2013).

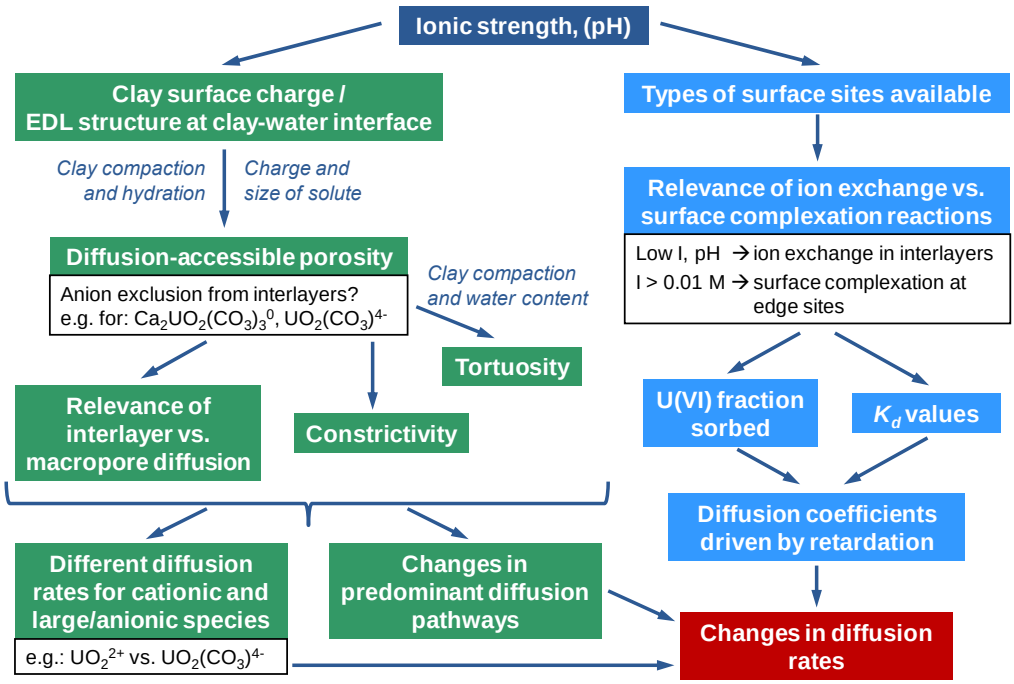

Figure 4.3. Overview of chemical solution effects on clay (surface) characteristics and diffusion rates.

In bentonite, the majority of the connected porosity is associated with the clay mineral fraction, which primarily consists of montmorillonite, a negatively-charged smectite. Montmorillonite particles are composed of stacks of smectite layers, which create interlayer spaces within individual clay particles. Hence, compacted smectite will have two porosities (Bourg et al., 2003): (1) large pores between clay particles, where diffusion is relatively unaffected by the clay surface, and (2) very thin interlayer pores, where diffusion is affected by surface charge and ionic strength. As diffusion is expected to take place differently in these two volumes (Bourg et al., 2003), this essentially creates two "small-scale diffusion pathways", where each may become dominant under different system conditions.

For instance, in compacted bentonite, smectites will be primarily present in the one- and two-layer hydrate form (i.e., one to two statistical monolayers of water in each interlayer). In addition, pore sizes can be so small that electric double layers balancing the charge of the bentonite may overlap (Bourg et al., 2003; Kerisit and Liu, 2009; Bourg, et al., 2006; Leroy et al., 2006). Under these conditions, anions have limited or no access to the interlayer (Figure 4.4) and can only diffuse through the macropore environments between clay particles. However, neutral and cationic solutes can, in principle, diffuse through the clay interlayers.

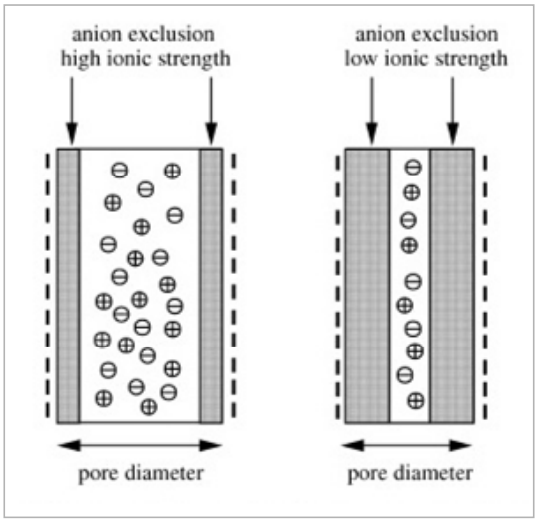

Figure 4.4. Visualization of anion exclusion effects (Van Loon & Soler, 2004).

On the other hand, at zero or minor degrees of compaction, anionic or larger neutral species may be able to enter the interlayer space in three-layer hydrate smectite particles. Furthermore, the influence of electrical double layers and background ionic strength might be expected to play greater roles under these conditions.

For uranium in the EBS, predominant U(VI) species may be either neutral or anionic depending on chemical solution conditions (Tinnacher and Davis, 2013). Anionic U(VI) species may not enter the interlayer when bentonite is compacted; perhaps even the neutral $Ca_2UO_2(CO_3)_3^0$ will not be able to enter because of steric hindrance. Thus, U(VI) diffusion into interlayer pores of compacted bentonite may be controlled by the supply of cationic U(VI) species, which may be found at low concentrations relative to other species. The diffusion of other U(VI) species will be limited to macropores between clay particles. As a result, different diffusion rates have to be expected for uranium as a function of the specific, molecular charge of individual species, e.g., UO_2^{2+} and $UO_2(CO_3)_3^{4-}$. In fact, Muurinen (1990) reported first indications of anion-exclusion effects for uranium in bentonite, and changes in effective diffusion coefficients due to variations in uranium speciation.

Moving on to another clay characteristic, tortuosity (τ^2) is in principal a dimensionless, geometric parameter. In practice, however, it is likely to depend on water content (Selim and Amacher, 1997), as well as clay compaction (dry density) and the ionic strength conditions in the pore-water (Van Loon et al., 2007).

Last, chemical solution effects on uranium speciation and clay surface properties will influence the fraction of sorbed U(VI), and hence, changes in metal diffusion coefficients driven by retardation. In addition, they will determine the dominant U(VI) sorption mechanism onto montmorillonite in terms of ion exchange or surface complexation. For instance, at low ionic strengths and mildly acidic pH, ion exchange within the interlayer space is expected to drive overall sorption. At ionic strengths greater than 0.01 M, surface complexation at edge sites predominates. Thus, even without strong compaction, solution conditions may still influence the “diffusion-accessible” porosity for U(VI).

4.2 Materials and Methods

During this past fiscal year, our experimental efforts were focused primarily on two main areas: (1) U(VI) batch sorption equilibrium experiments with Na-montmorillonite, and (2) diffusion studies in Na-montmorillonite. The data sets of previously performed equilibrium sorption experiments were further

extended to include an evaluation of the effects of calcium on uranium(VI) sorption behavior. This is motivated by the relevance of Ca for U(VI) solution speciation and the formation of ternary U-Ca-carbonato solution complexes in the circumneutral pH-range. All data sets were then used for the development of a U(VI)-Na-montmorillonite surface complexation model.

The implementation of diffusion experiments entailed the design of a diffusion cell and clay packing device that would allow experiments over a wide range of chemical solution conditions, including corrosive conditions at low pH and high ionic strength. In addition, because of the significantly higher solid-solution ratio in diffusion experiments compared to sorption studies, diffusion experiments also required an improved pretreatment procedure for the standardized Source Clay (Na-montmorillonite, SWy-2, Clay Minerals Society) to further minimize Ca impurities and the "uncontrolled" release of Ca from the solid phase. Motivated by the relevance of Ca for U(VI) solution speciation and the limited availability of Ca diffusion constants in pure montmorillonite in the literature (Kozaki et al., 2001), we performed a calcium bromide diffusion experiment in pretreated Na-montmorillonite. Finally, given the long duration of diffusion experiments, we simulated U(VI) diffusion behavior in lab-scale experiments in predictive models using the code ANADIFF (Eriksen et al., 1999; Eriksen and Jansson, 1996). These modeling results illustrate the relevance of chemical solution conditions for U(VI) diffusion rates, and are the basis for experimental planning and the selection of appropriate chemical solution conditions in U(VI) diffusion experiments.

A detailed description of materials and the setup for batch sorption equilibrium experiments has been provided in last year's report (Rutqvist et al., 2012; Section 5.2); hence, only a short summary will follow with respect to these subject areas.

4.2.1 Overview of Materials

All acids, bases and salt solutions used in experiments were of TraceSelect grade (Sigma Aldrich) in order to minimize calcium background concentrations. Uranium(VI) solutions contained ^{238}U from a 1.299 mM uranyl nitrate stock solution (provided by David Singer and Wayne Lukens at Lawrence Berkeley National Laboratory), and were analyzed by ICP-MS (Perkin-Elmer SCIEX ICP-Mass Spectrometer ELAN DRC II).

A commercially available, well-characterized, standardized Source Clay (Na-montmorillonite, SWy-2, Clay Minerals Society) was selected for experimental study. This material is known to contain considerable impurities of quartz (8%) and feldspars (16%) as well as calcite (Costanzo and Guggenheim, 2001; Chipera and Bish, 2001; Mermut and Cano, 2001). Hence, purification procedures were applied with the goal to effectively remove mineral impurities while preserving the original clay characteristics as much as possible. The pretreatment method described in last year's report was sufficient to decrease Ca release from Na-montmorillonite in batch sorption equilibrium experiments (0.5 g/L montmorillonite) to Ca concentrations that were low enough to avoid any influences on U(VI) solution speciation (5-30 µM Ca concentrations found in sorption experiments versus millimolar Ca concentrations required for changes in U(VI) solution speciation at $U(VI)_{Tot} = 10^{-6}$ M). However, due to the substantially higher clay concentration in diffusion studies (e.g., ~1 g/mL=1000 g/L), this procedure needed further improvement to prevent any unintended Ca release in these experiments.

4.2.2 Batch Sorption Equilibrium Experiments

All batch sorption experiments were set up at room temperature (22.5°C-23.5°C), with a nominal total U(VI) concentration of 10^{-6} M, a Na-montmorillonite concentration of 0.5 g/L, and a total ionic strength of 0.1 M NaCl. The main steps of the experiments included: (1) the pre-equilibration of Na-montmorillonite with a background electrolyte solution at the specified pH and chemical solution conditions, (2) U(VI) sorption equilibration with the mineral phase, (3) sampling and analysis of supernatant fractions after removal of the solid phase by centrifugation, and (4) a correction for U(VI) wall sorption effects based on an acid-wash procedure.

Experimental results for batch sorption envelope experiments are reported in terms of distribution coefficients (K_d values) and fractions of U(VI) sorbed. Distribution coefficients, with units of L/kg, represent the ratio of sorbed (e.g., in mol/kg) over dissolved (e.g., in mol/L) U concentrations after sorption over 48.5 hours. Sorbed U(VI) fractions were calculated based on concentration differences between (solid-free) standards and (solid-containing) samples.

4.2.3 Modeling Setup for Surface Complexation Models

In this report we present the results of a preliminary surface complexation model (SCM) to evaluate our ability to describe and predict the variations in uranium(VI) K_d values for sorption on montmorillonite as a function of solution conditions. We expect to refine this preliminary model further and produce the final SCM by the end of FY13. A review of the current status of U(VI) surface complexation modeling for montmorillonite was provided in last year's annual report (Rutqvist et al., 2012).

To use an SCM to describe the U(VI) sorption data, one must initially choose the electrical double layer (EDL) model that is part of the conceptual model of the SCM. In this case, we have chosen the triple layer model (TLM) because of the likely need to use EDL charge distribution terms in the final SCM to match the surface species with surface spectroscopy (Arai et al., 2006). Charge distribution terms cannot be used in simpler EDL models such as the diffuse double layer model.

Because we have not yet performed acid-base titrations of our specific montmorillonite sample to evaluate surface charge as a function of pH, we have employed the TLM developed for montmorillonite by McKinley et al. (1995), including the use of the same parameter values (see Table 4.5). Following the conceptual approach for the SCM of McKinley et al., we assume that UO_2^{2+} cations can exchange with other cations in the interlayer region of the montmorillonite, and that surface complexes can form on the edge sites of montmorillonite sheets. Furthermore, the same BET surface area of the SWy-1 montmorillonite used by McKinley et al. (1995), 31 m^2/g, has been included in our model as well. The edge surface area of montmorillonite has been estimated as 19.2 m^2/g (Duc et al., 2005) and this value was used in the EDL model.

In order to apply an EDL and SCM from the literature, one must be ensure that the site densities and ion exchange capacities are self-consistent (Davis et al., 2004). We have used the same cation exchange capacity (0.74 mmoles/g) and site densities for silanol and aluminol surface ligands (18.6 and 16.8 µmoles/g, respectively) as were used in the modeling by McKinley et al. (1995). In addition, we have used the same values of inner and outer layer capacitance (1.2 and 0.2 Farads/m^2, respectively) that were used by McKinley et al. (1995) and Zachara and Smith (1994).

The program FITEQL 4.0 (Herbelin and Westall, 1999) was used to fit U(VI) cation exchange and surface complexation constants to describe the U(VI) sorption data in the CO_2-free experimental system. For this preliminary model, surface complexation of U(VI) was assumed to occur only at aluminol sites. In addition, the constants obtained from that fit were then used in to predict U(VI) sorption at other experimental conditions. The refinement of the model during the remainder of FY13 will include the fitting of our own EDL parameters and additional U(VI) surface species as needed to fit the underpredictions of U(VI) sorption at other solution conditions.

4.2.4 Design of Diffusion Cell and Clay Packing Device

A detailed description of all considerations and steps for the design of the diffusion cell and clay packing device goes beyond the scope of this report. However, we will summarize the most important points in the following.

Research groups in Europe (e.g., Royal Institute of Technology, Sweden and Paul Scherrer Institute, Switzerland) have gained considerable experience with diffusion cells in through-diffusion experiments over the past years, but have also reported difficulties with specific components, such as the metal filters (e.g., Glaus et al., 2008). In these designs, a diffusion cell consists of the following main components: (1)

a "ring-like" cell containing the clay packing, (2) two metal filters holding the clay packing in place, and (3) two end pieces that allow for a homogeneous delivery of solutions over the metal filters, with solution flow in parallel to the filters. These end pieces are then connected to tubings that deliver the solutions of interest from two different reservoirs, the high-concentration and the low-concentration reservoirs.

We have decided to largely follow these designs (Figs. 4.5–4.7), which has the additional benefit of allowing for a direct comparison of our diffusion results with existing data in the literature. However, given the expected long time frames for uranium(VI) diffusion experiments, and our goal to characterize U(VI) diffusion behavior over a broad range of chemical solution conditions, including corrosive conditions at low pH and high ionic strength, the following additional design considerations were taken into account. With regards to the diffusion cell:

- Materials for the diffusion cell (PEEK) and the metal filters (Hastelloy C276, Mott Corporation) were selected to ensure (1) resistance to corrosion, (2) resilience to clay swelling pressures, (3) minimal swelling of the (plastic) material itself to ensure a constant volume of the clay packing, and (4) low machining costs.
- Dimensions for the "ring-like" cell containing the clay packing (D_i=2.54 cm, L=1 cm) were chosen in order to:
  - Minimize wall effects during reactive, diffusive transport and to
  - Ensure sufficient amounts of clay material for the slicing of the clay packing with an abrasion technique at the end of U(VI) diffusion experiments (with D_i=2.54 cm and the use of a U-233 tracer, we anticipate layer thicknesses as low as 20 µm).
- Hastelloy C276 was selected as material for the filters (Mott Corporation) to prevent the formation of fractures in the filter media caused by clay swelling during experiments, and to allow for rigorous cleaning of filters in between experiments (acid/base washes under oxidizing and reducing conditions, sonication).
- The porosity of the metal filters (10 µm) was chosen to decrease the potential trapping of clay particles in the filter media. The length of the clay packing (1 cm) and the filter thickness (0.16 cm) were selected to minimize the effects of potentially changing filter diffusivities on experimentally determined U(VI) diffusion coefficients based on mathematical considerations (Glaus et al., 2008).

In addition, a clay packing device was designed based on the following requirements:

- Reproducible packing of clay directly into the "ring-like" component of the diffusion cell.
- The possibility of quantifying the pressures applied during clay packing.

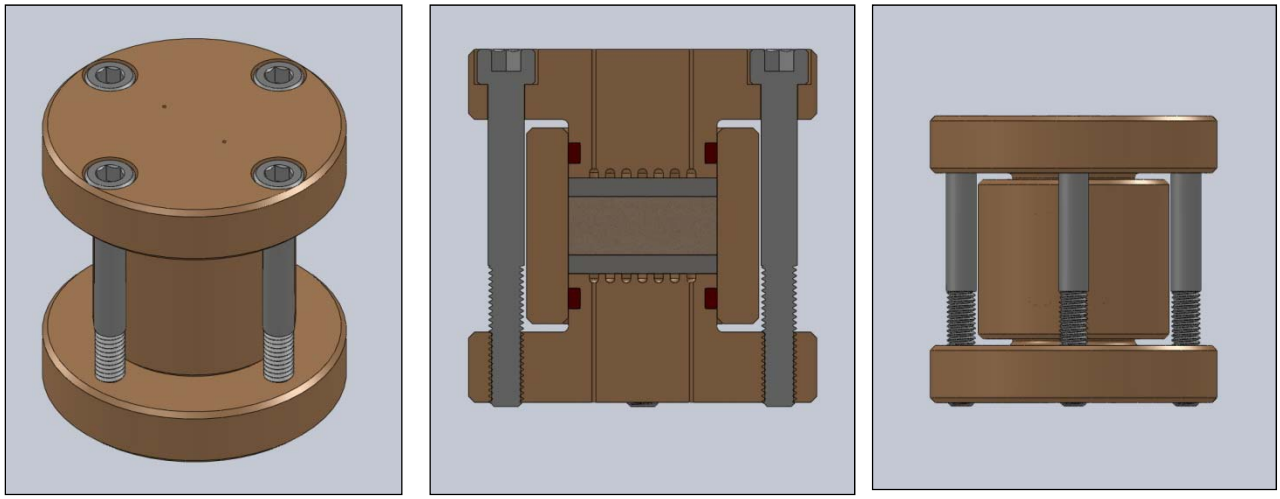

Figure 4.5. Diffusion cell design.

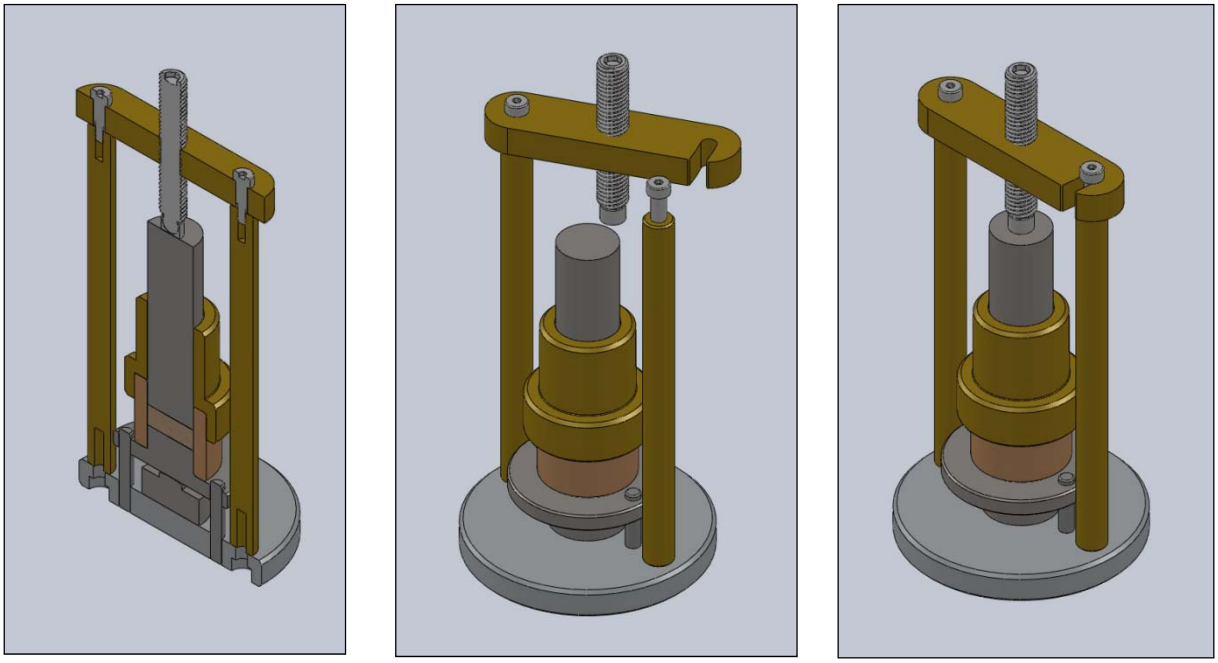

Figure 4.6. Design for clay packing device.

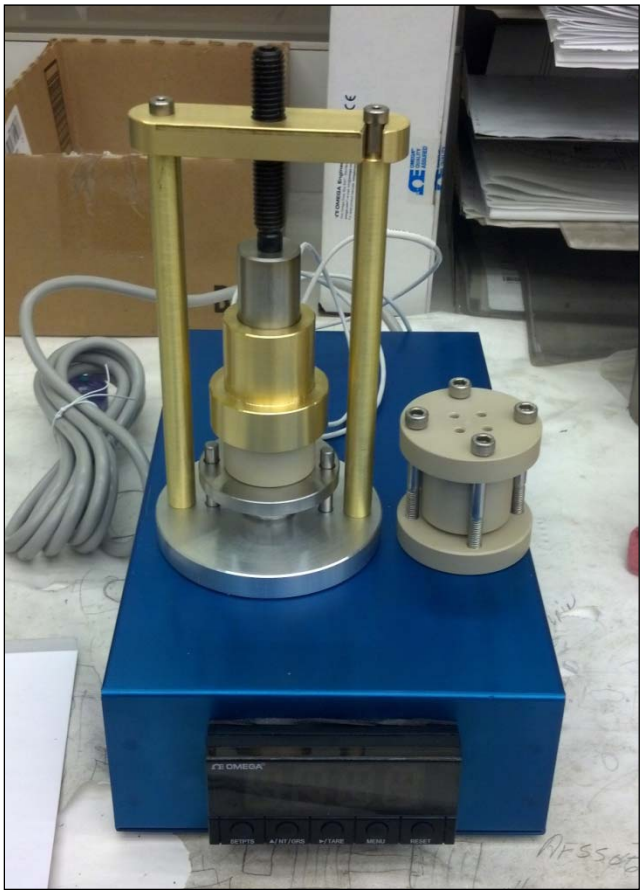

Figure 4.7. Diffusion cell and clay packing device.

4.2.5 Clay Pretreatment Specific to Diffusion Experiments

In last year's report (Rutqvist et al., 2012), we reported a pretreatment procedure for Na-montmorillonite (SWy-2, Clay Minerals Society), which included the following steps: (1) the removal of calcite impurities using a sodium acetate/acetic acid solution, (2) transforming the clay into its sodium form by equilibration with a Na-salt solution, (3) the removal of excess Na-salts from suspended clay, (4) the separation of quartz and feldspar impurities from clay particles by centrifugation and (5) oven-drying of the clay mineral phase. Pretreatment steps were performed using dialysis membranes, since this allows us to efficiently "up-scale" this setup for the purification of larger mineral quantities. To further improve the purification method for the use of Na-montmorillonite in diffusion experiments, the procedure was repeated with the following modifications:

- The number of extraction steps with sodium acetate/acetic acid solutions was increased from 4 to 6 steps.
- Clay equilibration in the Na-salt solution (1 M NaCl) was repeated 5 instead of 4 times.
- Clay centrifugation steps were performed 2–3 times, depending on the purity of the material based on visual evaluation, instead of only once.

4.2.6 Diffusion Experiment: Calcium Bromide Diffusion in Na-Montmorillonite

Calcium was selected for a diffusion experiment in Na-montmorillonite due to its relevance for U(VI) solution speciation and sorption behavior. Furthermore, impurities of calcium minerals have to be expected in engineered barrier systems, both in the bentonite buffer as well as the bordering cement-based layer. Hence, a calcium concentration gradient (Figure 4.1) and the diffusive transport of Ca within barrier systems seem very likely. At this point, only a few diffusion studies have been performed for Ca in bentonite (Mazzieri et al., 2010; Shackelford and Lee, 2003); data for Ca diffusion in Na-montmorillonite are even scarcer (Kozaki, 2001). However, these data will be very relevant for interpreting uranium(VI) diffusion behavior in Na-montmorillonite at varying Ca concentrations. Furthermore, using calcium bromide as a salt allowed us to study the diffusion behavior of a fairly non-reactive anion (bromine) in a sodium chloride background electrolyte solution.

The experimental setup for diffusion experiments consists of the diffusion cell containing the clay packing, the high-concentration and low-concentration reservoirs, the tubings and fittings connecting the reservoirs with the diffusion cell, and a peristaltic pump (Figure 4.8). All solutions used in the experiment were repeatedly adjusted to pH 7 using small volumes of acid/base solutions (TraceSelect grade NaOH and HCl) prior to their contact with the mineral phase.

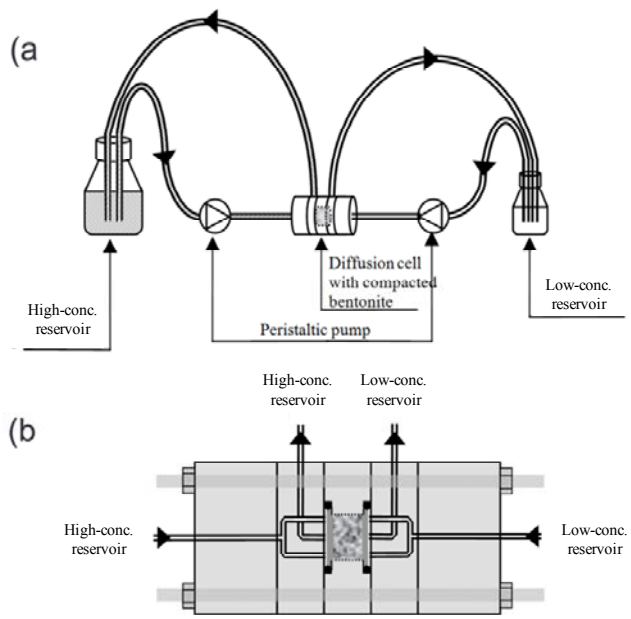

Figure 4.8. Schematic of setup for diffusion experiment (Courtesy of M. Holmboe; modified).

At the beginning of the experiment, a known weight of dry, pretreated Na-montmorillonite is packed into the "ring-like" component of the diffusion cell to give the desired dry density (~ 1.0 g/cm^3) in the given volume of the cell. Then, the high-concentration (200 mL) and the low-concentration (20 mL) reservoirs are filled with background electrolyte solution (0.1 M NaCl, pH=7), and the clay is saturated with electrolyte by circulating the solutions through the cell with a peristaltic pump (0.7 mL/min) for about 4 ½ weeks.

After clay saturation, the solution in the high-concentration reservoir is exchanged for a background electrolyte containing 1 mM $CaBr_2$, and the solution in the low-concentration reservoir is replaced with a 20 mL aliquot of fresh, $CaBr_2$-free electrolyte. Over the following weeks, the circulation of solutions through the diffusion cell is continued at the same flow rate. However, $CaBr_2$-free background electrolyte

solutions in the low concentration reservoir are continuously exchanged by replacing reservoir vials. This provides a constant concentration gradient between high- and low-concentration reservoirs, which is defined as less than 2% of the $CaBr_2$ concentration in the high-concentration reservoir found in the low-concentration reservoir. The collected low-concentration reservoir vials are weighed to correct for volume losses due to evaporation, sampled for Ca and Br analysis by ICP-MS, and their solution pH values are recorded. Furthermore, small volumes (1.5 mL) of the high-concentration reservoir solution are repeatedly sampled for Ca and Br analysis by ICP-MS, in order to monitor solute concentrations and the concentration gradient over the course of the experiment. This procedure is continued until the diffusive fluxes for both Ca and Br, have reached steady-state conditions, and a series of data points have been collected at steady state. The latter is a requirement for the mathematical determination of diffusion coefficients for Ca and Br based on experimental results (see Section 4.3. "Results and Discussion" for details below).

After reaching steady-state conditions for Ca and Br diffusion, the solution in the high-concentration reservoir is replaced with a $CaBr_2$-free background electrolyte solution containing approximately 1000 Bq/mL (27 nCi/mL) of tritiated water (HTO). Again, low-concentration reservoir solutions are continuously replaced, and tritium activities analyzed by liquid scintillation counting (PerkinElmer Liquid Scintillation Analyzer Tri-Carb 2900TR; Ultima Gold XR liquid scintillation cocktail), until the diffusive flux of HTO has reached steady-state conditions, and a sufficient number of data points has been collected under steady-state. The use of tritiated water as a non-reactive tracer allows for an exact determination of the diffusion-accessible porosity in the clay packing, which is required for the calculation of sorption distribution coefficients for sorbing solutes.

Similar diffusion experiments with U(VI) as solute of interest have been started. However, at this point, no experimental results are available, because of the differences in the experimental setup for Ca and U(VI). Due to the relatively high sorption affinities of U(VI) for Na-montmorillonite, the time frames for detecting U(VI) in low-concentration reservoir solutions and for reaching steady-state conditions for U(VI) diffusive flux are exceedingly long (for details, see Section "4.3.4. Predictive Modeling of Uranium(VI) Diffusion in Lab-Scale Experiments"). Hence, in these systems, U(VI) diffusion profiles will be determined based on U(VI) concentrations in the clay packing at the *end* of each experiment, instead of measuring U(VI) concentrations in low-concentration reservoir solutions *during* the experiment. As a result, these data sets only become available after a full completion of the experiment and the slicing of the clay packing using an abrasion technique.

4.2.7 Predictive Modeling of Uranium(VI) Diffusion in Lab-Scale Experiments

4.2.7.1 The Diffusion Code: ANADIFF

The simulation of U(VI) diffusion behavior in lab-scale experiments allows us to illustrate the relevance of chemical solution conditions for U(VI) diffusion behavior, and provides a basis for experimental planning and the selection of appropriate chemical solution conditions in U(VI) diffusion experiments. For this purpose, we simulated U(VI) diffusion as a function of chemical solution conditions using the code ANADIFF (Eriksen et al., 1999; Eriksen and Jansson, 1996). ANADIFF allows for the calculation of contaminant breakthrough curves and concentration profiles in a one-dimensional, lab-scale through diffusion experiment, assuming a constant solute concentration (C_0) in the source reservoir (Figure 4.9). In these simulations, clay samples and the two (metal) filters holding the clay packing in place are assumed to be homogeneous, with single, individual values of (transport) porosity. Calculations are based on Fick's first law of diffusion, describing diffusive flux of solutes under steady-state conditions with an "*effective*" diffusion coefficient (D_e).

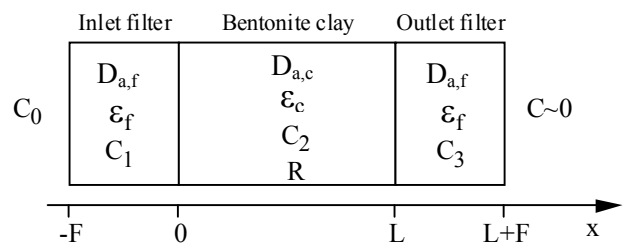

Figure 4.9. Schematic of diffusion cell, containing a clay packing sandwiched between two filter plates, used in ANADIFF simulations (Eriksen and Jansson, 1996).

For solute transport through the inlet and outlet filters, solute sorption onto the filter media is assumed to be negligible by default. This results in the following expression, e.g., for solute diffusion through the inlet filter:

$$J = -A\varepsilon_f D_{a,f} \frac{\partial C_1}{\partial x} \tag{4.8}$$

where J is the diffusive flux through the inlet filter ($-F < x < 0$, see Figure 4.9), A the cross-sectional area of the diffusion cell, ε_f the filter porosity, $D_{a,f}$ the *apparent* diffusion coefficient in the filter, C_1 the solute concentration in the filter and x distance. In this equation (Eq. 4.8), applicable to non-sorbing solutes, the "*effective*" diffusion coefficient in the filter ($D_{e,f}$) is the product of the apparent diffusion coefficient and the filter porosity ($D_{e,f} = D_{a,f}\varepsilon_f$).

In contrast, for diffusion through the clay packing, the code explicitly allows for solute interactions with the clay mineral, based on a linear sorption distribution coefficient (K_d value), resulting in

$$J = -A\varepsilon_c D_{a,c} \frac{\varepsilon_c + \rho K_d}{\varepsilon_c} \frac{\partial C_2}{\partial x} \tag{4.9}$$

where ε_c is the clay porosity, $D_{a,c}$ the apparent diffusion coefficient of the solute in clay, ρ the dry (bulk) density, and C_2 the solute concentration in the clay pore solution. The capacity (retardation) factor R is related to the K_d value by

$$R = \frac{\varepsilon_c + \rho K_d}{\varepsilon_c} \tag{4.10}$$

Hence, the expression $(\varepsilon_c D_{a,c} R)$ is equivalent to the effective diffusion coefficient in clay ($D_{e,c}$) for sorbing solutes.

4.2.7.2 Modeling Setup

ANADIFF is used to predict U(VI) diffusion through Na-montmorillonite in lab-scale experiments as a function of pH and Total Inorganic Carbon (TIC) concentrations in solution (Table 4.2). In these simulations, we combine our own experimental data with values from the literature.

For U(VI), an assumption of negligible solute-filter interactions may not be universally valid, especially if fine clay particles become trapped in the filter media (Glaus et al., 2008). Hence, U(VI)-filter interactions were implicitly included in our simulations as described in the following, while assuming that these interactions can vary with chemical conditions. In the first step, the dominant U(VI) solution species was determined individually for each set of chemical solution conditions to be simulated (Table 4.2), based on our previous results from speciation modeling with existing thermodynamic data (NEA database (Guillaumont et al., 2003); data not reported). Then, U(VI) diffusion coefficients in free aqueous solution (D_0) were estimated for these species using literature values from molecular dynamics simulations (Kerisit and Liu, 2010). Finally, the *effective* uranium diffusivities in the filter media ($D_{e,f}$) were

computed by taking into account that solute diffusion coefficients are typically 10-times smaller in filters than in free aqueous solution (Glaus et al., 2008). However, since ANADIFF only allows for a direct input of *apparent* but not *effective* filter diffusion coefficients, we "tricked" the code by entering the calculated effective diffusion coefficient as an apparent diffusion coefficient with an "artificial" filter porosity of 1.

For the simulation of U(VI) diffusion through the clay sample, model input parameters were based on results from our U(VI)-Na-montmorillonite batch sorption experiments (Table 4.2), performed at room temperature, and literature values for uranium diffusion coefficients in clay (Korichi et al., 2010). At this point, we assumed that uranium(VI) diffusion coefficients in Na-montmorillonite are estimated best by using published, experimentally determined U(VI) diffusion coefficients in clay (Korichi et al., 2010), rather than performing calculations with simulated values for molecular U(VI) diffusion coefficients. In general, extreme caution has to be exercised when transferring diffusion coefficients for reactive solutes between studies (Shackelford and Daniel, 1991), especially to avoid confusion between effective and apparent coefficients. In addition, it is useful to clearly state the underlying assumptions when applying published diffusion coefficients to new systems. In this case, we assumed that, for a given dry (bulk) density, the clay sample used in the study by Korichi et al. (from Maghna, Algeria) has similar tortuosity and porosity values as our pretreated Na-montmorillonite (SWy-2 from Wyoming, USA; Clay Minerals Society). This assumption is supported by fairly comparable U(VI) sorption parameters for both clays. Furthermore, we assumed that the dimensions of Korichi's diffusion cell were selected in such a way that filter effects on the experimentally determined U(VI) diffusion coefficients are negligible.

Based on these assumptions, we could back-calculate the U(VI) pore diffusion coefficient ($D_{p,c}$) based on the reported values for the apparent U(VI) diffusion coefficient ($D_{a,c}$) and the U(VI) K_d value determined at the same chemical solution conditions (pH=7.2, I=0.1 M $NaNO_3$, C_0=20 mg/L U(VI), dry density ρ =1.4 g/cm^3, porosity ε_c =0.512, tortuosity=4.6, K_d value=1905 L/kg).

$$D_{p,c} = D_{a,c} \frac{\varepsilon_c + \rho K_d}{\varepsilon_c} \tag{4.11}$$

Then, this value of $D_{p,c}$ ($D_{p,c}$=4.12 × 10^{-8} m^2/sec) was used to compute values of apparent U(VI) diffusion coefficients in clay for the individual chemical solution conditions to be simulated (Eq. 4.11), as by definition $D_{p,c}$ is independent of chemical solution conditions. In this calculation, we used U(VI) K_d values determined in our batch sorption experiments under variable chemical conditions (Table 4.2), and clay porosity and bulk density values reported by Korichi et al. (Table 4.3).

Overall, for the simulation of U(VI) diffusion over changing chemical solution conditions, we varied the following model input parameters: (1) the apparent U(VI) diffusion coefficients in the filter media, (2) the apparent U(VI) diffusion coefficients in the clay packing, and (3) the U(VI) K_d values for U(VI) sorption onto clay. An overview of input parameters that remained constant during all model runs is provided in Table 4.3.

Table 4.2. Overview of variable model input parameters

Sim.	pH	CO_2	TIC	Dominant U(VI) species	D_0 [1)]	$D_{e,f}$	$D_{a,f}$ [2)]	$D_{a,c}$	K_d
( )	( )	( )	(mol/L)	( )	(m^2/sec)	(m^2/sec)	(m^2/sec)	(m^2/sec)	(L/kg)
Variable TIC, comparable pH conditions (pH~7.3)									
1	7.29	'CO_2-free'	4.76E-05	$(UO_2)_2CO_3(OH)_3^-$	6.10E-10	6.10E-11	2.03E-10	8.60E-13	17,528
2	7.35	Atm. CO_2	3.52E-04	$(UO_2)_2CO_3(OH)_3^-$	6.10E-10	6.10E-11	2.03E-10	3.99E-12	3,780
3	7.24	1% CO_2	2.39E-03	$UO_2(CO_3)_2^{2-}$	5.52E-10	5.52E-11	1.84E-10	2.94E-11	512
Variable pH, comparable TIC concentrations (TIC~2E-05 mol/L, atmospheric CO_2)									
4	3.95	Atm. CO_2	1.10E-05	UO_2^{2+}	7.66E-10	7.66E-11	2.55E-10	7.88E-11	191
5	4.40	Atm. CO_2	9.45E-06	UO_2^{2+}	7.66E-10	7.66E-11	2.55E-10	3.47E-11	434
6	5.12	Atm. CO_2	2.18E-05	UO_2^{2+}	7.66E-10	7.66E-11	2.55E-10	7.83E-12	1,925
7	5.63	Atm. CO_2	2.88E-05	$UO_2(OH)^+$	7.66E-10	7.66E-11	2.55E-10	2.59E-12	5,820
8	6.12	Atm. CO_2	5.12E-05	$UO_2(OH)^+$	7.66E-10	7.66E-11	2.55E-10	9.06E-13	16,624

[1)] From Kerisit and Liu, 2010 and Kerisit, personal communication; [2)] Assuming a filter porosity of 0.3 (-)

Table 4.3. Constant model input parameters

	Parameter	Value (units)
Filters	Thickness	0.155 (cm)[1)]
	Porosity	0.3 (-)[1, 2)]
	Cross-sectional area	5.11 (cm^2)[1)]
Clay packing	Length	1.1 (cm)[1)]
	Porosity	0.512 (-)[3)]
	Dry density	1.4 (g/cm^3)[3)]
	Cross-sectional area	5.11 (cm^2)[1)]
Solutions	Conc. in source reservoir	10^{-6} (M)
	Conc. in receiving reservoir	0 (M)
Experiment	Time of interest	360 (days)

[1)] Van Loon et al., 2003.
[2)] Entered as porosity of 1 in ANADIFF (see text).
[3)] Korichi et al., 2010.

4.3 Results and Discussion

4.3.1 Batch sorption equilibrium experiments and surface complexation modeling

4.3.1.1 Experimental Results

In batch sorption equilibrium experiments, we evaluated the effects of CO_2(g) (atmospheric CO_2 (~ 0.039% CO_2), CO_2-free atmosphere and ~1% CO_2) and dissolved calcium (2 mM $CaCl_2$) on U(VI) sorption behavior to Na-montmorillonite. It is important to note here that CO_2 levels of ~1% are not uncommon in natural systems and probably represent a "low end" value of CO_2 concentrations in disturbed environments. An overview of all experimental data sets in terms of percent U(VI) sorbed (Figure 4.10; Table 4.4) and U(VI) log K_d values (Figure 4.11; Table 4.4) is provided below. Error bars represent 95% confidence intervals of analytical errors. These data sets were the basis for the development of a U(VI)-montmorillonite surface complexation model.

A detailed discussion of the impacts of CO_2 has been provided in last year's report (Rutqvist et al., 2012). Briefly, under atmospheric CO_2 conditions, U(VI)-montmorillonite distribution coefficients vary over three orders of magnitude as a function of pH. At low pH, U(VI) sorption is assumed to be limited due to its competition with protons for the same reactive surface/ion exchange sites (Stumm, 1992). At high pH, low uranium sorption is attributed to increasing carbonate concentrations, leading to weakly sorbing or non-sorbing aqueous U(VI)-carbonato complexes (Davis et al., 2004; Hsi and Langmuir, 1985). In CO_2-

free systems, the shape of the U(VI) batch sorption envelope is different compared to the atmospheric CO_2 system. In the low-pH region, U(VI) sorption characteristics remain similar with comparable K_d values in the pH range from 4 to 6. Above pH 7, however, U(VI) sorption is much stronger in the absence of CO_2. The increase in U(VI) sorption at high pH values is attributed to the lack of aqueous U(VI)-carbonato complexes in the N_2(g) environment. The effect of carbonato solution complexes on U(VI) sorption characteristics is also demonstrated by U(VI) sorption results for the system with elevated CO_2 concentrations (~1% CO_2 atmosphere). In this case, the shape of the sorption envelope is similar to the one determined under atmospheric carbon dioxide conditions. However, U(VI) sorption decreased at pH values greater than 5.8.

Overall, a variation in CO_2(g) and TIC concentrations in solution has substantial impact on the fraction of U(VI) sorbed (Figure 4.10) and causes changes in U(VI) K_d values over several orders of magnitude (Figure 4.11). As a result, changes in inorganic carbon concentrations can lead to variations in U(VI) mobility over several orders of magnitude.

Comparing the data sets for U(VI) sorption under atmospheric CO_2 conditions in the presence of 2 mM $CaCl_2$ and Ca background concentrations (Figure 4.12), we find that the data sets only diverge for pH values greater than ~7.4. In this higher pH region, U(VI) solution speciation changes due to the presence of 2 mM Ca, which leads to the formation of ternary Ca-U-carbonato complexes (Figs. 4.13 and 4.14). This shift in U(VI) speciation further causes a decrease in the fraction of U(VI) sorbed onto Na-montmorillonite. For instance, at pH~8, the U(VI) K_d value is lowered by approximately half an order of magnitude.

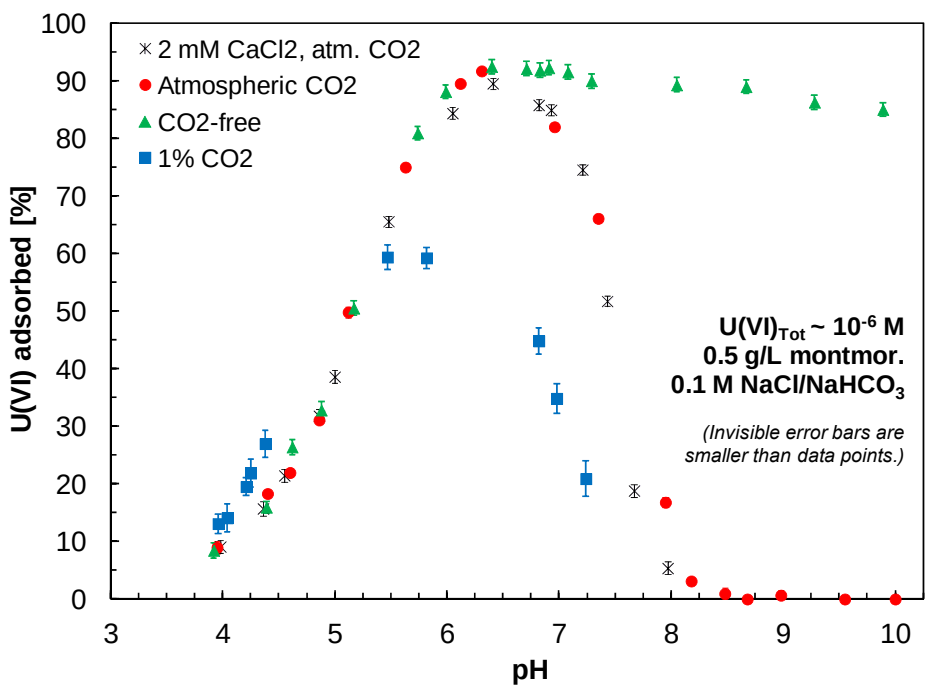

Figure 4.10. U(VI) adsorption onto Na-montmorillonite at varying chemical solution conditions.

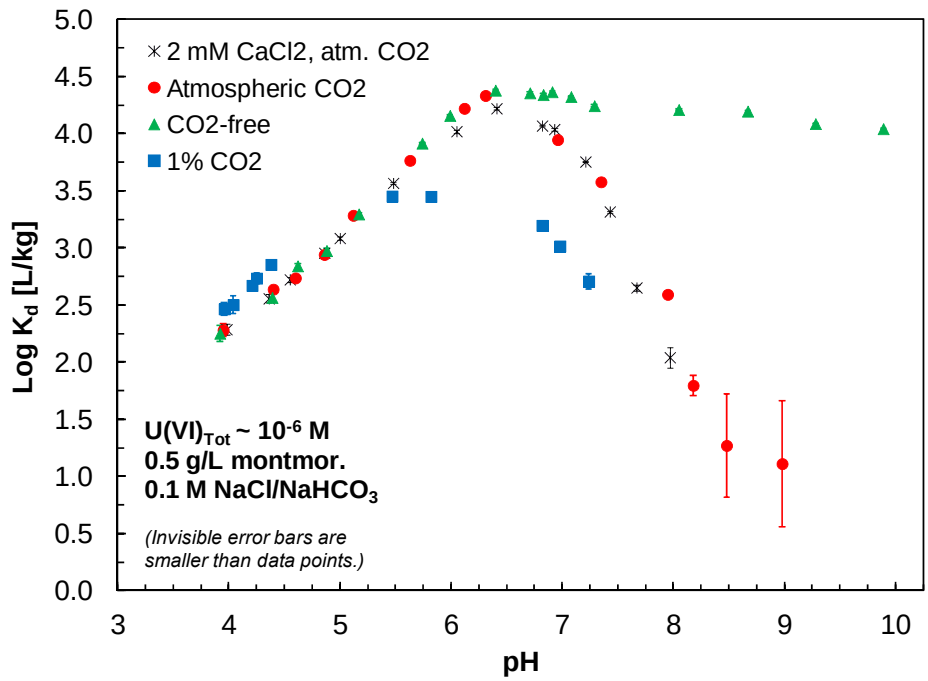

Figure 4.11. K_d values for U(VI) sorption to Na-montmorillonite at varying chem. solution conditions.

Table 4.4. Summary of U(VI) adsorption data in batch sorption envelope experiments

Atmospheric CO_2, Ca-free				CO_2-free atmosphere, Ca-free				~1% CO_2 atmosphere, Ca-free				Atmospheric CO_2, 2 mM Ca			
pH	U(VI) sorbed	Kd	log Kd	pH	U(VI) sorbed	Kd	log Kd	pH	U(VI) sorbed	Kd	log Kd	pH	U(VI) sorbed	Kd	log Kd
[ ]	[%]	[L/kg]	[L/kg]	[ ]	[%]	[L/kg]	[L/kg]	[ ]	[%]	[L/kg]	[L/kg]	[ ]	[%]	[L/kg]	[L/kg]
3.95	8.98	191	2.28	3.92	8.46	179	2.25	3.96	13.10	292	2.47	3.98	9.11	194	2.29
4.40	18.33	434	2.64	4.39	15.96	367	2.57	4.04	14.09	318	2.50	4.36	15.73	361	2.56
4.60	21.98	545	2.74	4.62	26.42	695	2.84	4.21	19.53	470	2.67	4.55	21.47	529	2.72
4.86	31.10	874	2.94	4.88	32.83	946	2.98	4.25	21.89	543	2.73	4.86	31.82	904	2.96
5.12	49.86	1,925	3.28	5.17	50.54	1,978	3.30	4.38	26.99	715	2.85	5.00	38.62	1,218	3.09
5.63	75.04	5,820	3.76	5.74	80.98	8,239	3.92	5.47	59.41	2,833	3.45	5.48	65.63	3,697	3.57
6.12	89.57	16,624	4.22	5.99	88.15	14,403	4.16	5.82	59.27	2,817	3.45	6.05	84.41	10,484	4.02
6.31	91.75	21,533	4.33	6.40	92.52	23,945	4.38	6.82	44.86	1,575	3.20	6.41	89.58	16,635	4.22
6.96	82.05	8,845	3.95	6.71	92.15	22,712	4.36	6.98	34.88	1,037	3.02	6.82	85.83	11,728	4.07
7.35	66.13	3,780	3.58	6.83	91.89	21,917	4.34	7.24	20.91	512	2.71	6.93	84.97	10,943	4.04
7.95	16.82	391	2.59	6.91	92.30	23,211	4.37	n/a	n/a	n/a	n/a	7.21	74.59	5,683	3.75
8.18	3.13	63	1.80	7.08	91.58	21,049	4.32	n/a	n/a	n/a	n/a	7.43	51.77	2,078	3.32
8.48	0.95	19	1.27	7.29	90.06	17,528	4.24	n/a	n/a	n/a	n/a	7.67	18.84	449	2.65
8.68	n.d.	n/a	n/a	8.05	89.33	16,212	4.21	n/a	n/a	n/a	n/a	7.97	5.39	110	2.04
8.98	0.66	13	1.11	8.67	89.03	15,703	4.20	n/a	n/a	n/a	n/a	n/a	n/a	n/a	n/a
9.55	n.d.	n/a	n/a	9.28	86.32	12,216	4.09	n/a	n/a	n/a	n/a	n/a	n/a	n/a	n/a
10.00	n.d.	n/a	n/a	9.89	85.07	11,027	4.04	n/a	n/a	n/a	n/a	n/a	n/a	n/a	n/a

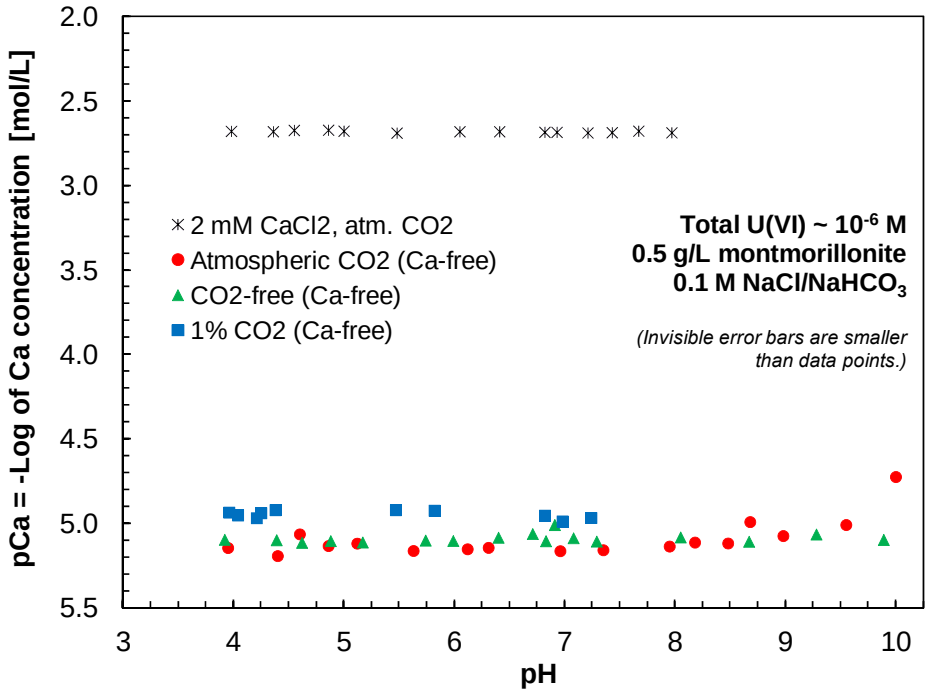

Figure 4.12. Total, measured Ca concentrations in solution for batch sorption equilibrium experiments.

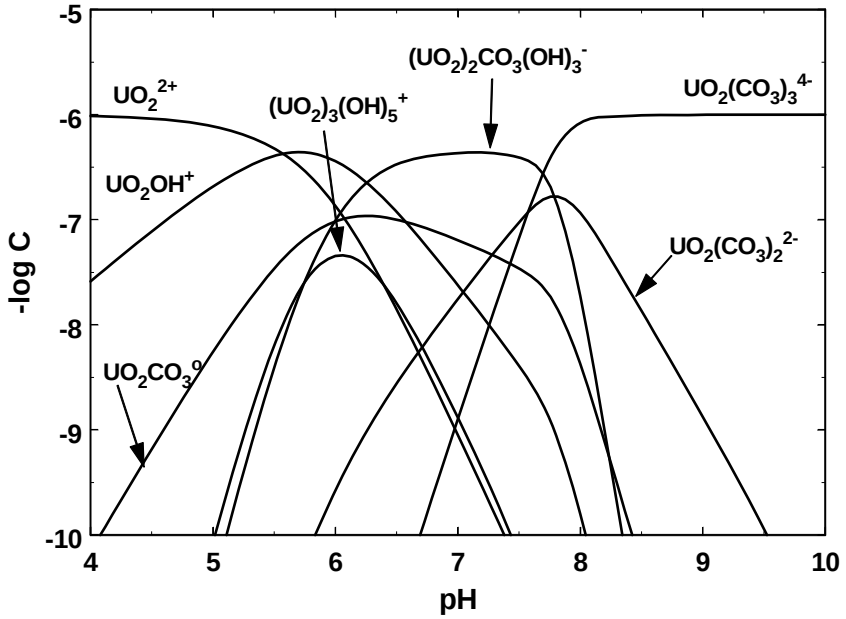

Figure 4.13. Aqueous speciation of a 1 micromolar U(VI) solution in 0.1 M NaCl in equilibrium with atmospheric CO_2 (log CO_2 = -3.5) as a function of pH. Vertical axis is the negative log of the concentration of each U(VI) species.

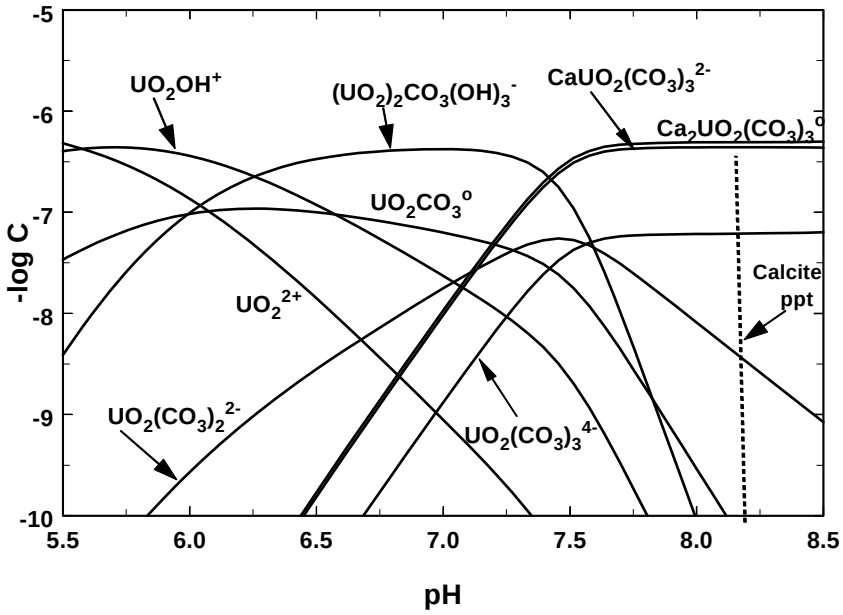

Figure 4.14. Same as Figure 4.13. except solution now contains 2 mM Ca. Aqueous speciation of a 1 micromolar U(VI) solution in 0.1 M NaCl in equilibrium with atmospheric CO_2 (log CO_2 = -3.5) as a function of pH. Vertical axis is the negative log of the concentration of each U(VI) species.

4.3.1.2 Modeling Results

In our preliminary modeling approach, we used only one of the four U(VI) sorption data sets for the fitting of model parameters, namely U(VI) sorption data determined in the CO_2-free (and Ca-free) system. Uranium(VI) sorption trends in the remaining three systems (1% CO_2, Ca-free; atmospheric CO_2, Ca-free; and atmospheric CO_2, 2 mM Ca) were then *predicted*, based on fitted values of surface complexation and ion exchange constants (Table 4.5) and the known changes in U(VI) solution speciation, which were calculated using published thermodynamic data (Guillaumont et al., 2003; Dong and Brooks, 2008).

Table 4.5. Overview of uranium(VI) surface reactions in surface complexation model

Species	Reaction	Log K (I = 0)
UO_2X_2	$UO_2^{2+} + 2NaX = UO_2X_2 + 2Na^+$	7.99
AlO_2UO_2	$Al(OH)_2 + UO_2^{2+} = AlO_2UO_2 + 2H^+$	-1.50
AlO_2UO_2OH	$Al(OH)_2 + UO_2^{2+} = AlO_2UO_2OH + H^+$	-10.34

Model predictions are able to capture very well the general changes in U(VI) sorption behavior as a function of varying chemical solution conditions (Figure 4.15). Ion exchange was more important than surface complexation only below pH 4 at this Na concentration (0.1 M). Hence, these results demonstrate the strong capability of surface complexation models to *predict* contaminant sorption behavior for various chemical solution conditions, which is possible due to their strong link to solution chemistry and metal solution speciation. In comparison, radionuclide transport models with constant K_d values do not have the same predictive capabilities, unless they are linked to surface complexation models in some manner, e.g., through expressions for "smart" K_d values.

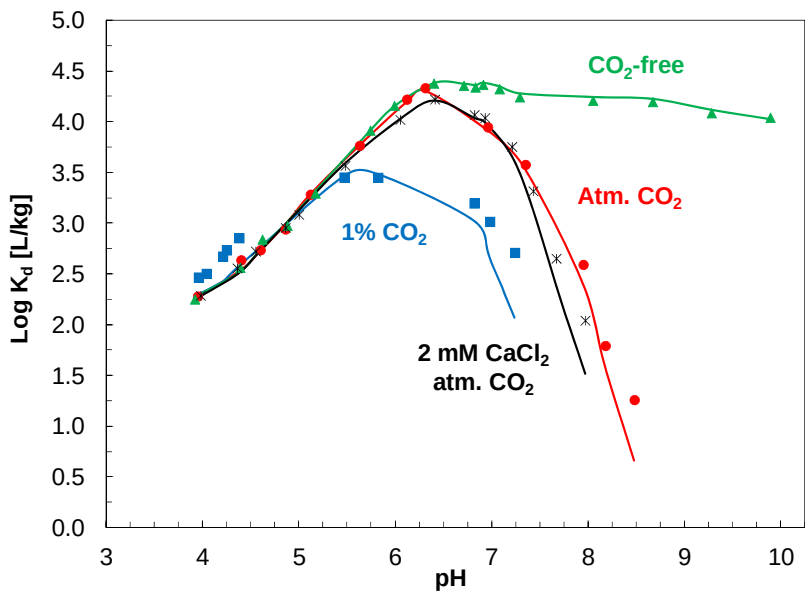

Figure 4.15. Modeling results for U(VI) sorption onto Na-montmorillonite over the whole pH range.

A more detailed comparison of the modeling results with the experimental data in the circumneutral pH range reveals two interesting features (Figure 4.16). First, at pH > 5.8, the model underpredicts U(VI) sorption in the 1% CO_2 system. This suggests that the formation of ternary U(VI)-carbonato surface complexes, which has not been included in this model at this point, may be relevant under these conditions. Second, while the model is able to capture the differences in U(VI) sorption in the presence and absence of Ca at pH values greater than ~7.4, it also predicts a larger decrease in U(VI) sorption for the 2 mM Ca system than the experimental data. A few additional experiments are needed in order to fully clarify both points, e.g., at higher CO_2 and Ca concentrations and varying ionic strength conditions.

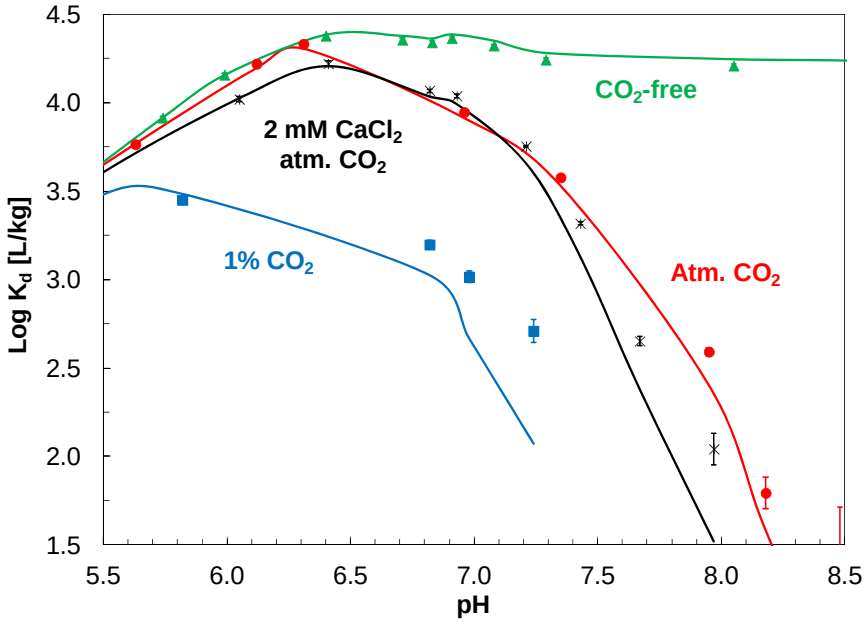

Figure 4.16. Detailed modeling results for U(VI) sorption onto Na-montmorillonite between pH values of 5.5 and 8.5.

4.3.2 Calcium Bromide Diffusion in Na-Montmorillonite

4.3.2.1 Experimental Results

After the collection of low-concentration reservoir solutions for the individual time points in the $CaBr_2$ diffusion experiment, solution pH was measured in each sample vial. Based on our results (Figure 4.17), the pH in these solutions continuously shifted from pH 7 to slightly lower values, most likely due to solution contact with the clay mineral phase.

Over the course of the experiment, the high-concentration reservoir (200 mL) was repeatedly sampled for small volume fractions (1.5 mL) in order to monitor Ca and Br concentrations by ICP-MS (Figure 4.18), while minimizing the loss of solution from the reservoir. Our analytical results show fairly constant total concentrations of Ca and Br in this reservoir. Furthermore, Ca and Br concentrations measured in low-concentration reservoir samples only exceeded 2% of their respective concentrations in the high-concentration reservoir for three data points. Hence, we can conclude that our assumption of a constant concentration gradient between high- and low-concentration reservoirs is generally justified, which is an important mathematical requirement for the application of the selected analytical solution of the diffusion equation (see details below).

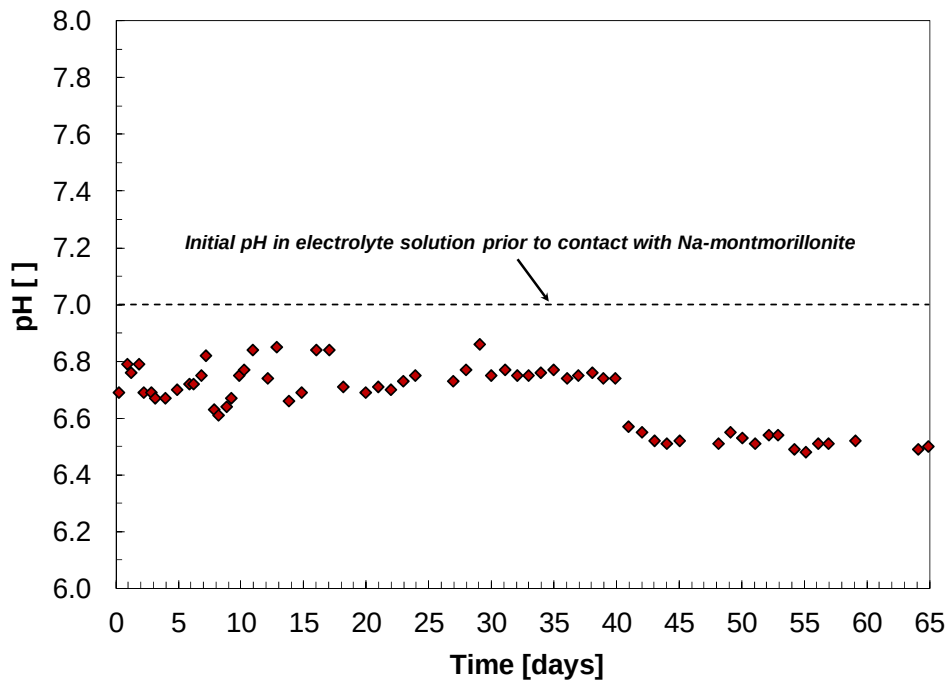

Figure 4.17. Results for monitoring of solution pH in low-concentration reservoir solutions during $CaBr_2$ diffusion experiment.

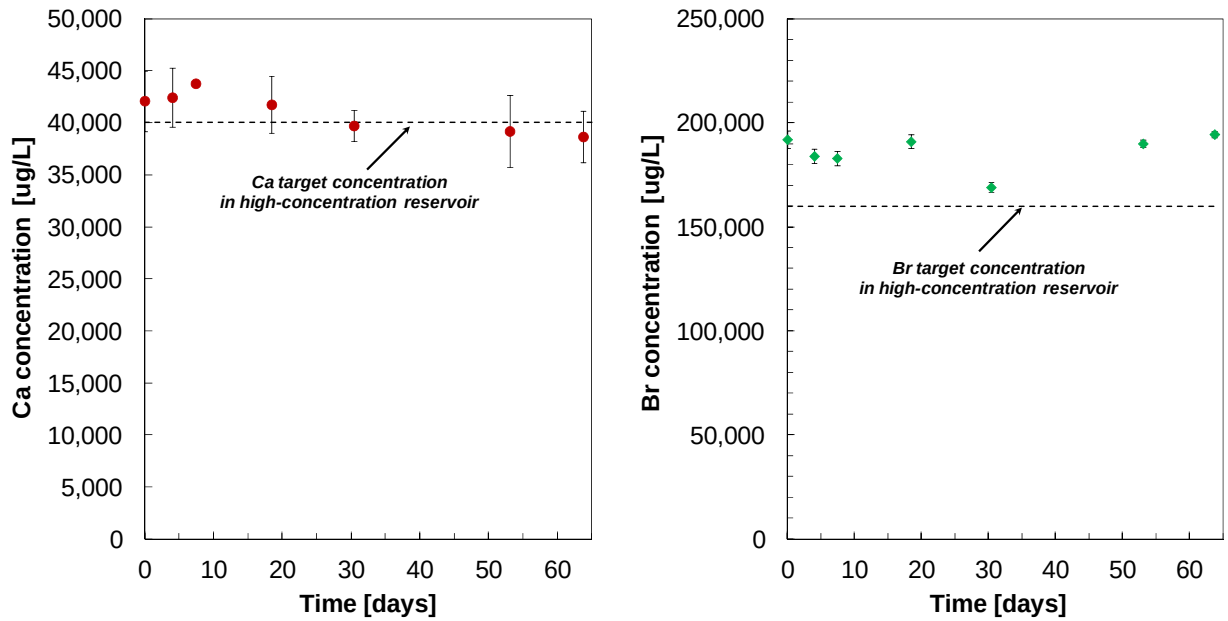

Figure 4.18. Results for monitoring of Ca and Br concentrations in high-concentration reservoir solution during $CaBr_2$ diffusion experiment. Error bars for Ca data represent standard deviations of replicate ICP-MS analysis of the same samples; error bars for Br data are standard deviations for replicate injections during ICP-MS analysis of the same samples.

In through-diffusion experiments, the solute concentrations or activities measured in the low-concentration reservoir solutions over time are typically used to compute the diffusive flux and cumulative mass of solutes based on the following equations (Van Loon et al., 2003; Van Loon and Soler, 2004). Following these data interpretation steps, measured Ca and Br concentrations and tritium activities were first corrected for their background values found in the background electrolyte solution. The net concentrations or activities for the individual time-point samples were then used to calculate the total concentration or activity that is diffused through the diffusion cell during each time interval Δt_i.

For tritium activity measurements, determined in terms of counts per minute (cpm) on the liquid scintillation counter (LSC), the net diffused activity ($N_{diff}^{\Delta t_i}$) per time step (Δt_i) was calculated for the *first* time step ($\Delta t_i = \Delta t_1$ and $N_S^{\Delta t_i} = N_S^{\Delta t_1}$) as

$$N_{diff}^{\Delta t_i} = \frac{N_S^{\Delta t_i}}{V_{count}} V_{sample} + \frac{N_S^{\Delta t_i}}{V_{count}} V_{dead} \tag{4.12}$$

where $N_S^{\Delta t_i}$ represents the net counts in each sample fraction after background subtraction, V_{count} the volume fraction of the low-concentration reservoir sample that is counted on the LSC (mL), V_{sample} the exact volume in the low-concentration reservoir determined by weighing (mL), and V_{dead} the dead volume (V_{dead} =1.3869 mL) on the low-concentration reservoir side of the diffusion setup, including the volumes in tubings, the grooves in the end plate and the metal filter pore space (all determined by weighing).

For all *later* time points, the net diffused activity per time step was computed with the following expression, which now also corrects for the activity left in the dead volume of the cell from the previous time step:

$$N_{diff}^{\Delta t_i} = \frac{N_S^{\Delta t_i}}{V_{count}} V_{sample} + \frac{N_S^{\Delta t_i}}{V_{count}} V_{dead} - \frac{N_S^{\Delta t_{i-1}}}{V_{count}} V_{dead} \tag{4.13}$$

Now, the activity (in units of nanoCi) diffused through the clay packing in the diffusion cell during each time step can be expressed as follows, while taking into account the tritium counting efficiency of the LSC (E=0.3911) and the conversion from disintegrations per minute (dpm) to nanoCi (1 nCi=2220 dpm):

$$A_{diff}^{\Delta t_i} = \frac{N_{diff}^{\Delta t_i}}{E \times 2220} \tag{4.14}$$

Hence, the total diffused activity (or cumulative activity) up to time point t_n (in nCi) is then given by

$$A_{diff}^{t_n} = \sum_{i=1}^{n} A_{diff}^{\Delta t_i} \tag{4.15}$$

and the average diffusive flux (nCi/(cm^2 hr)) per time step as

$$J^{t_i} = \frac{A_{diff}^{\Delta t_i}}{S \Delta t_i} \tag{4.16}$$

where S is the cross-sectional area of the clay packing (cm^2).

For the data interpretation of Ca and Br concentration measurements, the same general procedure is followed, but in concentration and mass units. Hence, the net diffused mass ($m_{diff}^{\Delta t_i}$) per time step (Δt_i) is computed for the *first* time step as

$$m_{diff}^{\Delta t_i} = \frac{c_S^{\Delta t_i}}{1000} V_{sample} + \frac{c_S^{\Delta t_i}}{1000} V_{dead} \tag{4.17}$$

where $c_S^{\Delta t_i}$ is the net concentration of Ca or Br (µg/L) measured by ICP-MS analysis. For all *other* timepoints,

$$m_{diff}^{\Delta t_i} = \frac{c_S^{\Delta t_i}}{1000} V_{sample} + \frac{c_S^{\Delta t_i}}{1000} V_{dead} - \frac{c_S^{\Delta t_{i-1}}}{1000} V_{dead} \tag{4.18}$$

Furthermore, the total diffused mass (or cumulative mass) up to time point t_n (in µg) is then given by

$$m_{diff}^{t_n} = \sum_{i=1}^{n} m_{diff}^{\Delta t_i} \tag{4.19}$$

The average diffusive flux (in µg/(cm^2 hr)) per time step is calculated as

$$J^{t_i} = \frac{m_{diff}^{\Delta t_i}}{S \Delta t_i} \tag{4.20}$$

The experimental results for the diffusive flux and cumulative mass/activity plots for Ca, Br, and tritium (^{3}H) are given in the following figures 4.19 to 4.24. For Ca, the time-frame needed to reach steady-state conditions in our Na-montmorillonite diffusion experiment (~33 days) agrees well with previously published data for calcium diffusion in bentonite (31 days (Mazzieri et al., 2010) or 35 days (Shackelford and Lee, 2003)).

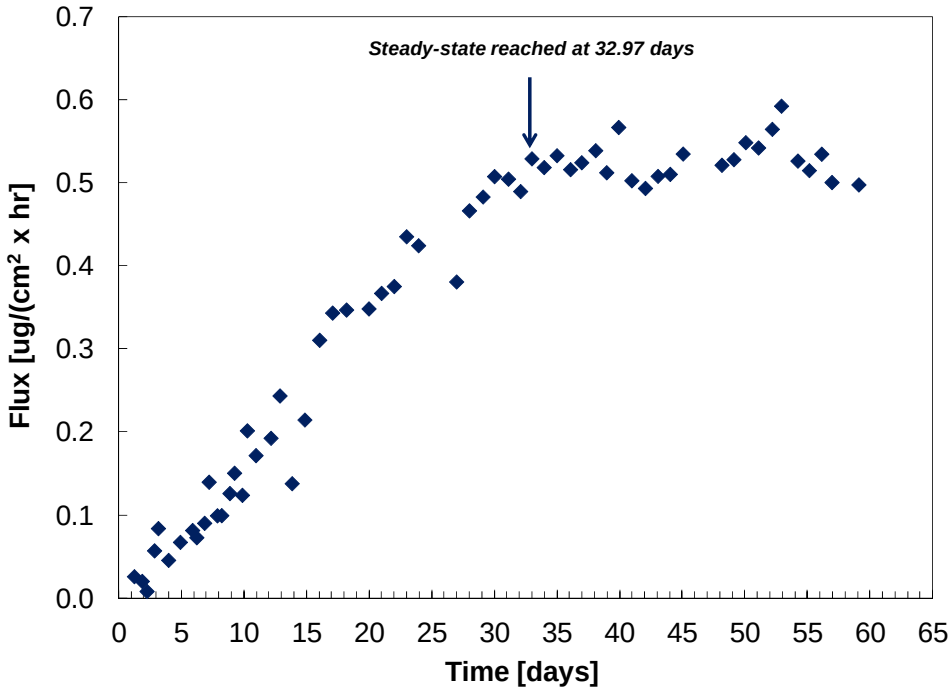

Figure 4.19. Diffusive flux of Ca through pretreated Na-montmorillonite as a function of time in $CaBr_2$ through-diffusion experiment at 1 mM $CaBr_2$, I=0.1 M NaCl and pH~7. Steady-state conditions are approximately reached at 32.97 days.

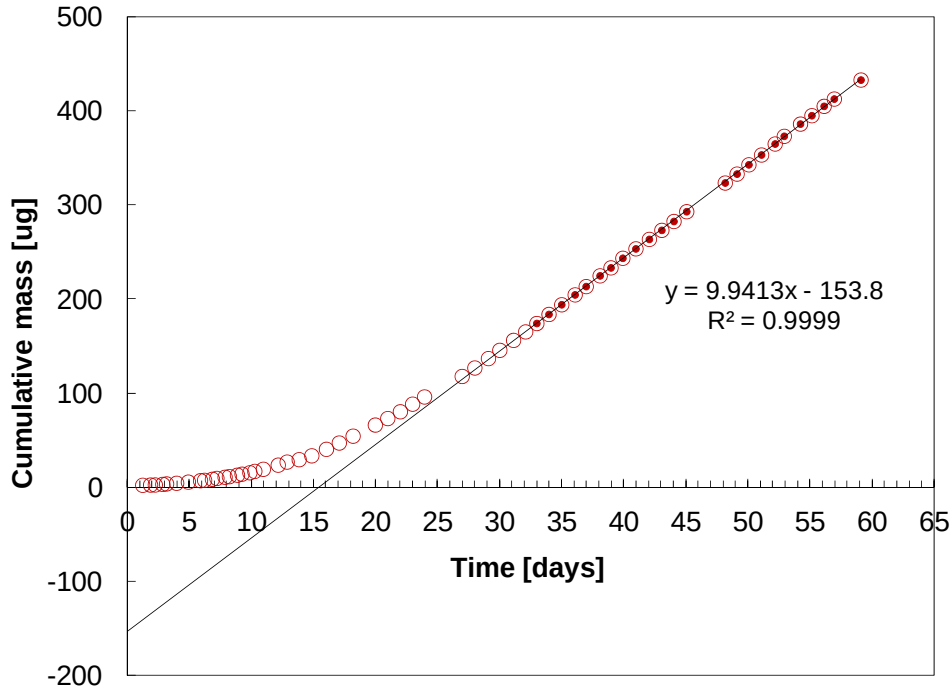

Figure 4.20. Cumulative mass of Ca as a function of time in $CaBr_2$ through-diffusion experiment in pretreated Na-montmorillonite at 1 mM $CaBr_2$, I=0.1 M NaCl and pH~7. Data points shown as dots are assumed to be under steady-state conditions and are used for the fitting of the asymptote to calculate diffusion parameters (see text for details).

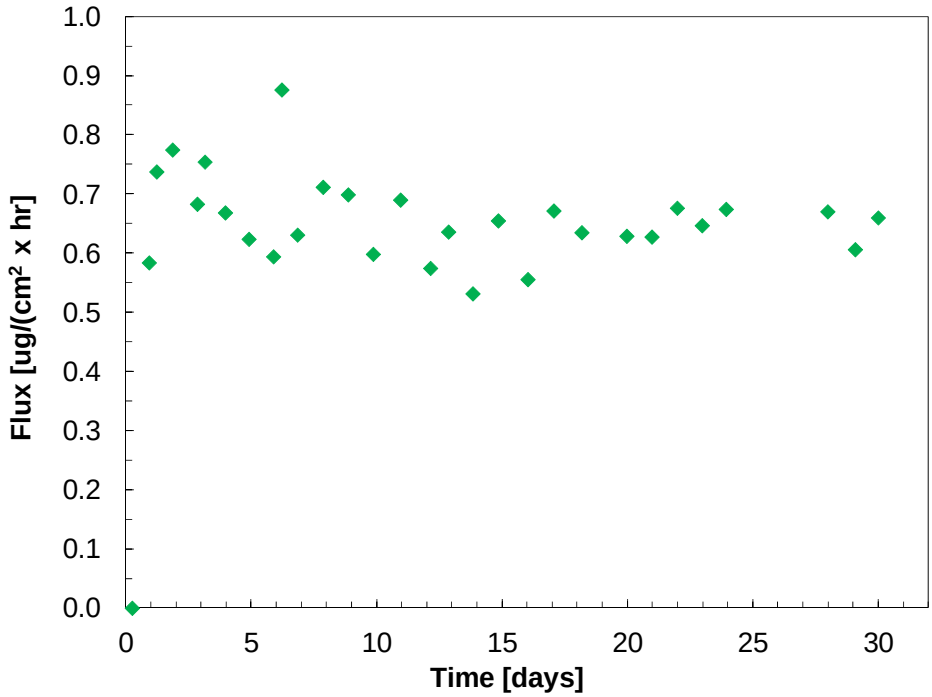

Figure 4.21. Diffusive flux of Br through pretreated Na-montmorillonite as a function of time in $CaBr_2$ through-diffusion experiment at 1 mM $CaBr_2$, I=0.1 M NaCl and pH~7. Steady-state conditions are most likely reached after a few days.

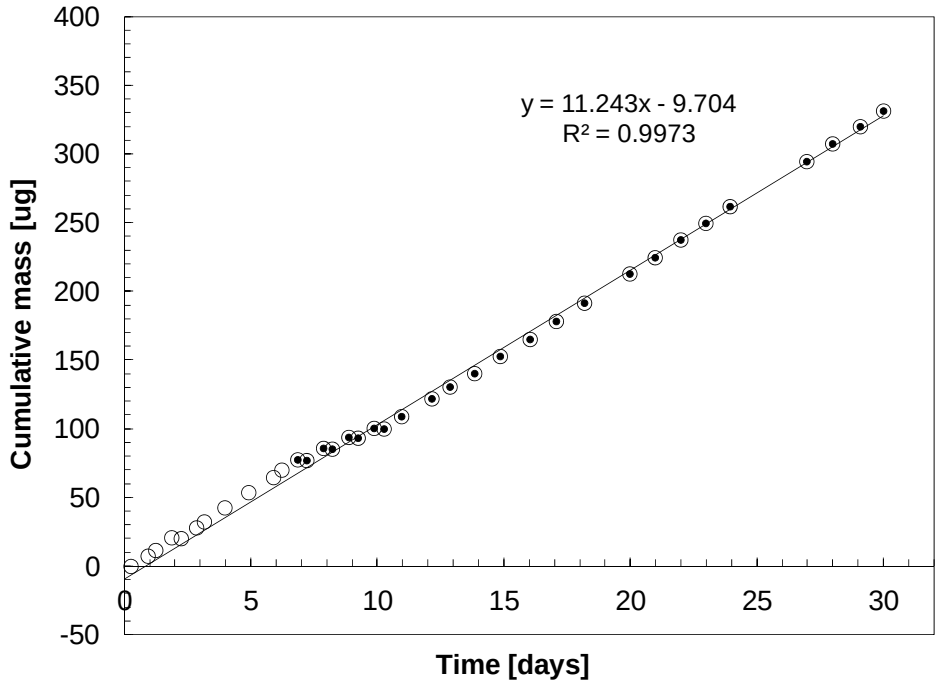

Figure 4.22. Cumulative mass of Br as a function of time in $CaBr_2$ through-diffusion experiment in pretreated Na-montmorillonite at 1 mM $CaBr_2$, I=0.1 M NaCl and pH~7. Data points shown as dots are assumed to be under steady-state conditions and are used for the fitting of the asymptote to calculate diffusion parameters (see text for details).

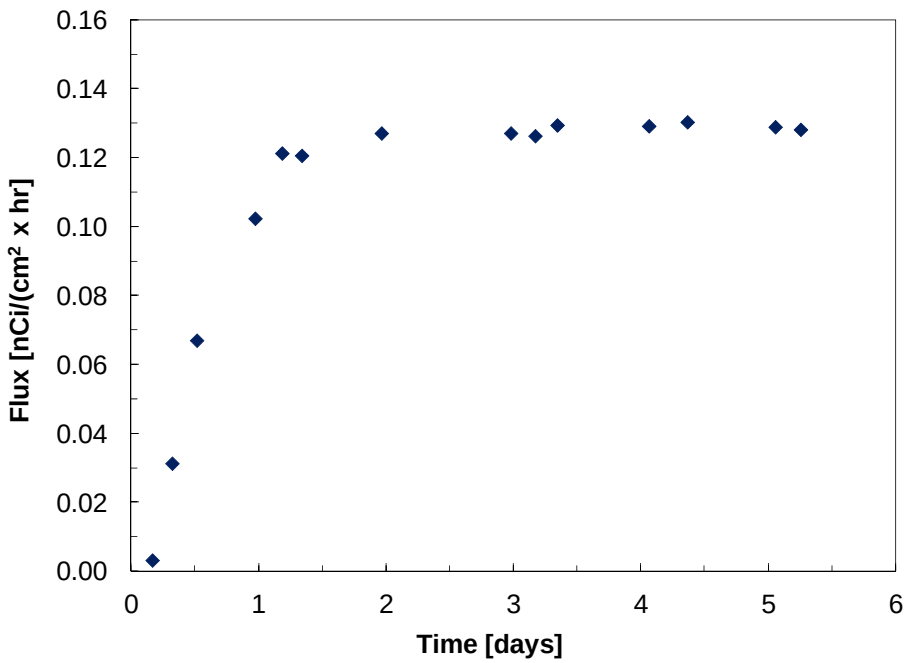

Figure 4.23. Diffusive flux of tritium through pretreated Na-montmorillonite as a function of time in $CaBr_2$ through-diffusion experiment at I=0.1 M NaCl and pH~7. Steady-state conditions are most likely reached after 1-2 days.

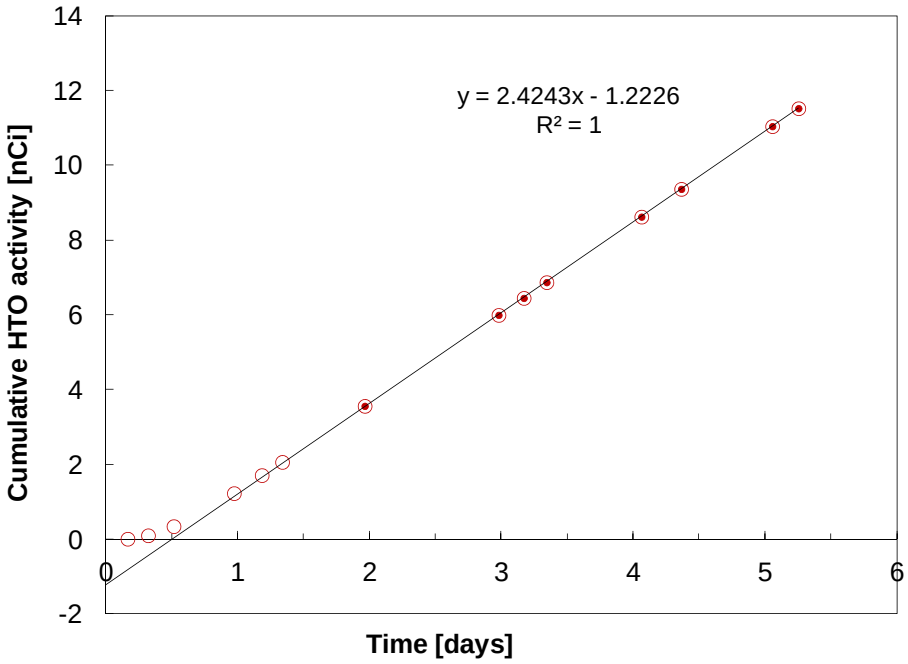

Figure 4.24. Cumulative activity of tritium as a function of time in $CaBr_2$ through-diffusion experiment in pretreated Na-montmorillonite at I=0.1 M NaCl and pH~7. Data points shown as dots are assumed to be under steady-state conditions and are used for the fitting of the asymptote to calculate diffusion parameters (see text for details). Tracer experiment is currently still ongoing in order to collect a larger number of data points under steady state conditions.

4.3.2.2 Mathematical Background for Data Interpretation

In the following, we provide a brief overview of the mathematical background for the interpretation of diffusion data; additional detail is given elsewhere (van Loon et al., 2003; Van Loon and Soler, 2004). For one-dimensional diffusion through a clay packing with a diffusion length of L, the diffusive flux (J) can be calculated based on Fick's first law:

$$J = -D_e \frac{\partial c}{\partial x} \tag{4.21}$$

where D_e represents the effective diffusion coefficient, c the solute concentration, and x the distance along the diffusion cell. The concentration change within the system is described by Fick's second law of diffusion:

$$\frac{\partial c}{\partial t} = D_a \frac{\partial^2 c}{\partial x^2} \tag{4.22}$$

where the apparent diffusion coefficient (D_a) is linked to the effective diffusion coefficient through the rock capacity value (α):

$$D_a = \frac{D_e}{\alpha} \tag{4.23}$$

For through-diffusion experiments, the concentration gradient in the clay packing along the diffusion length (x) is assumed to be linear under steady-state conditions. Hence, the analytical solution to the through-diffusion problem is found by solving Fick's second law (Eq. 4.22) with the following initial and boundary conditions:

$$c(x,t) = 0 \qquad t = 0$$

$$c(0,t) = C_0 \qquad x = 0$$

$$c(L,t) = 0 \qquad x = L$$

and by taking into account that the diffusive flux at the end of the clay packing ($x = L$) is equal to

$$J(L,t) = -D_e \frac{\partial c}{\partial x}\Big|_{x=L} \tag{4.24}$$

The general analytical solution (Crank, 1975; Jakob et al., 1999) gives the cumulative mass (or activity) diffused through the clay packing in the diffusion cell as a function of time. In terms of cumulative or total diffused mass, it can be expressed as

$$m_{diff}^{t_n} = c(L,t) \cdot V_{sample} = S \cdot L \cdot C_0 \left(\frac{D_e}{L^2} t - \frac{\alpha}{6} - \frac{2\alpha}{\pi^2} \sum_{n=1}^{\infty} \frac{(-1)^n}{n^2} \exp\left(-\frac{D_e n^2 \pi^2 t}{L^2 \alpha} \right) \right) \tag{4.25}$$

in terms of cumulative activity, it is equal to

$$A_{diff}^{t_n} = S \cdot L \cdot A_0 \left(\frac{D_e}{L^2} t - \frac{\alpha}{6} - \frac{2\alpha}{\pi^2} \sum_{n=1}^{\infty} \frac{(-1)^n}{n^2} \exp\left(-\frac{D_e n^2 \pi^2 t}{L^2 \alpha} \right) \right) \tag{4.26}$$

However, under steady-state conditions (with $t \to \infty$) the analytical solution can be simplified to

$$m_{diff}^{t_n} = \frac{S C_0 D_e}{L} t - \frac{S L C_0 \alpha}{6} \tag{4.27}$$

for concentration units, and analogously to

$$A_{diff}^{t_n} = \frac{SA_0 D_e}{L} t - \frac{SLA_0 \alpha}{6} \tag{4.28}$$

for activity units. As a result, the slopes of cumulative mass and activity curves are equal to

$$a = \frac{SC_0 D_e}{L} \qquad a = \frac{SA_0 D_e}{L} \tag{4.29}$$

and the intercepts of their asymptotes to

$$-b = \frac{SLC_0 \alpha}{6} \qquad -b = \frac{SLA_0 \alpha}{6} \tag{4.30}$$

After fitting the asymptotes to the experimental data for cumulative mass and activity plots, these equations (Eq. 4.29 and 4.30) can be further used to calculate the effective diffusion coefficient of the solute (D_e) as well as the rock capacity factor (α), e.g., for concentration units,

$$D_e = a \frac{L}{SC_0} \qquad \alpha = -\frac{6b}{SLC_0} \tag{4.31}$$

Furthermore, based on Eq. (4.23), the determined effective diffusion coefficient and rock capacity factor can now be used to compute the apparent diffusion coefficient (D_a) for the individual solutes.

In general, the rock capacity factor is defined as

$$\alpha = \varepsilon + \rho \cdot K_d \tag{4.32}$$

and includes the diffusion-accessible porosity (ε), the dry bulk density of the mineral (ρ), and the sorption distribution coefficient (K_d). For non-reactive tracers, such as tritiated water, the sorption distribution coefficient is equal to zero, and the calculated rock capacity factor can be directly used to determine the diffusion-accessible porosity in the clay packing. Then, this porosity value can be applied to compute the K_d values for sorbing solutes in the diffusion experiment based on Eq. 4.32. This is of particular interest, as the differences in solid concentrations between batch sorption equilibrium experiments and diffusion studies may affect the values of distribution coefficients determined in each type of experiment.

The results of our data interpretation are summarized in Table 4.6. In the calculation of sorption distribution coefficients, a value of 0.784 (g/cm^3) was used for the dry bulk density, which was determined based on the clay mass weighed into the diffusion cell and the known volume of the cell. A second determination of the exact clay mass will follow at the end of the diffusion experiment in order to minimize the experimental error associated with the computed parameters.

Table 4.6. Parameters determined in $CaBr_2$ diffusion experiment

	Ca	Br	HTO
Effective diffusion coefficient, D_e [cm^2/hr]	6.41E-03	1.60E-03	2.43E-03
Rock capacity factor, α [ ]	5.71E+01	7.96E-04	7.05E-01
Apparent diffusion coefficient, D_a [cm^2/hr]	1.12E-04	2.01E+00	3.44E-03
K_d [cm^3/g]=[L/kg]	71.99	-0.90	0

4.3.3 Predictive Modeling of Uranium(VI) Diffusion in Lab-Scale Experiments

In Figures 4.25 and 4.26, we depict simulated U(VI) diffusion profiles as a function of chemical solution conditions and time. These profiles represent *total* metal concentrations (sorbed and dissolved U(VI))

plotted over the total length of the diffusion cell. The positions of the inlet and outlet filters are highlighted by two blue-shaded areas on the left and right hand-side of each figure. The initial U(VI) solution concentration of 10^{-6} mol/L in the high-concentration reservoir is equivalent to 1 mM U(VI)/m^3. Hence, similar U(VI) concentration ranges found in the metal filter close to the high-concentration reservoir are not easily visible in these figures due to the scaling selected for the y-axis.

Based on these results, both the total concentration of U(VI) found in the clay packing as well as the overall shape of the diffusion profiles are strongly influenced by chemical solution conditions. For TIC, low inorganic carbon concentrations lead to high total U(VI) concentrations and steep slopes of diffusion profiles. In contrast, high TIC concentrations result in low total U(VI) concentrations and relatively flat profiles. For pH variations ranging from pH=4 to pH=6.1, we observe higher total U(VI) concentrations and steeper slopes of diffusion profiles with increasing pH. These trends are directly linked to U(VI) sorption behavior and the U(VI) K_d values specified for individual solution conditions. Large U(VI) K_d values lead to high concentrations of sorbed and hence total U(VI), especially within short distances from the inlet filter. This, in turn, creates steeper slopes for diffusion profiles.

In addition, U(VI) sorption affinities affect the distribution of total U(VI) over the length of the diffusion cell as a function of time. High U(VI) K_d values limit metal mobility through the clay packing at the beginning of the experiment. For instance, after 36 days, U(VI) is only transported about 0.6 cm into the diffusion cell setup in the "CO_2-free" system (K_d=17,528 L/kg), while it migrates through the entire clay packing under 1% CO_2 conditions (K_d=512 L/kg). Independent of the chemical solution conditions, we see an increase in total and sorbed U(VI) with each time step simulated over 360 days. This further implies that none of these systems becomes limited in mineral surface sites for U(VI)-clay interactions over time.

In Figure 4.27, we show relative U(VI) solution concentrations plotted over the length of the diffusion cell setup at the end of the simulated diffusion experiment (360 days). These are solution concentrations of U(VI) that are found in the pores of the clay packing or the filter media. Again, chemical solution conditions and U(VI) sorption affinities have large impacts on U(VI) solution concentrations and metal mobility. Systems with high U(VI) K_d values (e.g., "CO_2-free" system at pH=7.3) show higher concentrations of sorbed U(VI), which results in lower U(VI) solution concentrations in the clay pores. On the other hand, systems with low K_d values (e.g., pH=4, 4.4 and 5.1 at atmospheric CO_2) are characterized by higher U(VI) solution concentrations in the clay packing.

Overall, we conclude that chemical solution conditions and U(VI) speciation may have significant impacts on metal diffusion through clays in engineered barriers systems. However, these simulations are based on simplified conceptual models due to the limitations of the code ANADIFF. They can only account for changes in U(VI) sorption behavior (K_d values), but not the impacts of chemical solution conditions on clay (surface) characteristics (see Section 4.1.3 for details), potentially leading to indirect effects on U(VI) diffusion behavior, e.g., due to anion exclusion effects. Hence, there is a strong need to consider these parameters in further experimental investigations and predictive transport models.

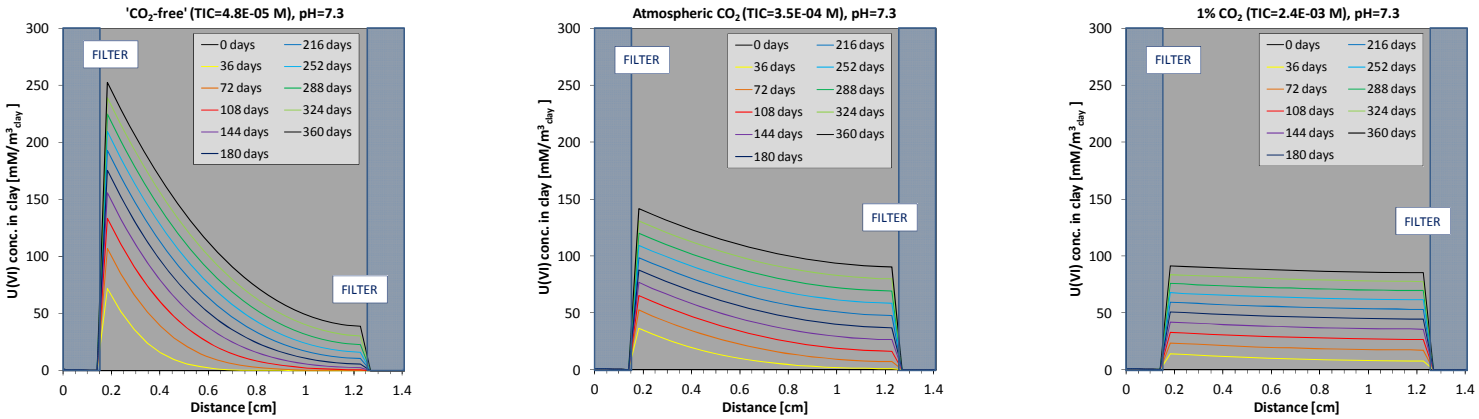

Figure 4.25. Simulated diffusion profiles: Total U(VI) conc. along a clay packing as a function of Total Inorganic Carbon (TIC) conc. and time.

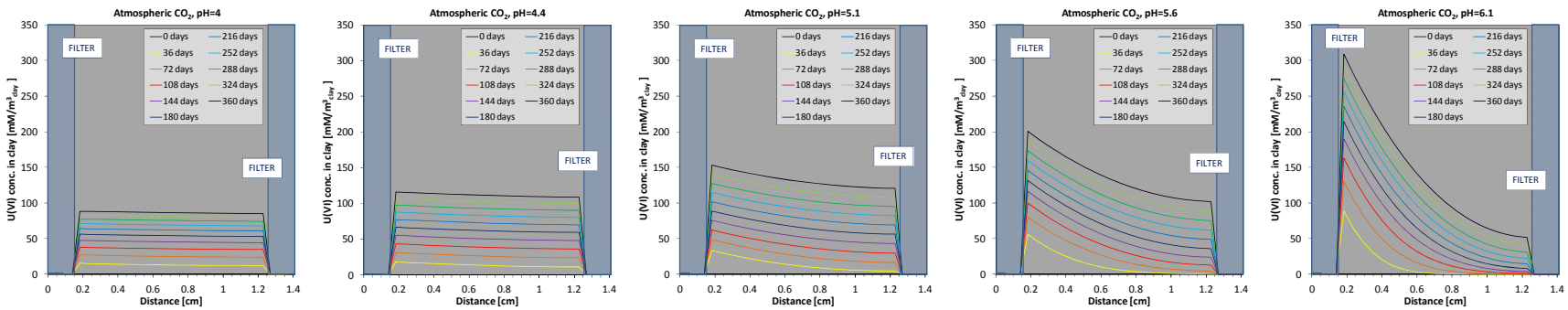

Figure 4.26. Simulated diffusion profiles: Total U(VI) concentrations along a clay packing as a function of solution pH and time.

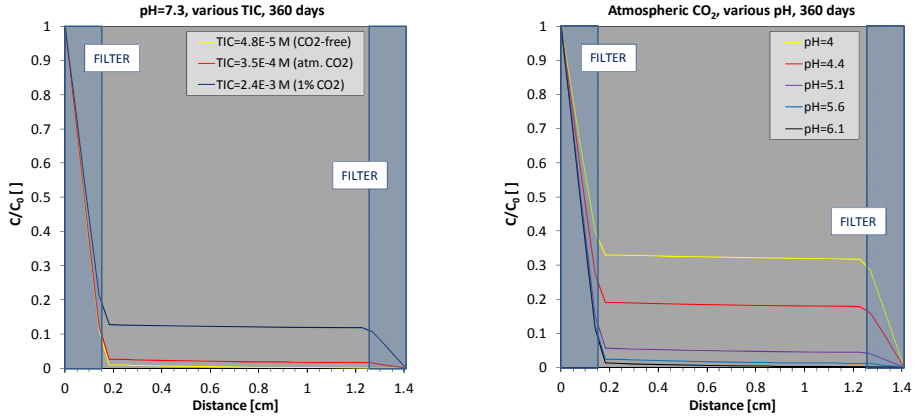

Figure 4.27. Simulated relative U(VI) solution concentrations as a function of Total Inorganic Carbon (TIC) concentrations and pH after a 360-day experiment.

4.4 Summary

From our theoretical analysis of the effects of chemical solution conditions on uranium(VI) diffusion coefficients and clay (surface) properties, we concluded that solution chemistry can literally affect *all types* of U(VI) diffusion coefficients, from the molecular diffusion coefficient in solution to the apparent diffusion coefficient in porous media.

In batch sorption equilibrium experiments, we demonstrated the influence of chemical solution conditions, in terms of pH, total inorganic carbon (TIC) and calcium concentrations, on U(VI) sorption behavior. As a result, U(VI) K_d values can vary over several orders of magnitude, which will lead to a change in U(VI) mobility to the same degree.

The surface complexation model we developed describes U(VI) sorption onto Na-montmorillonite based on two types of U(VI) sorption processes, ion exchange and two surface complexation reactions. During model development, only one data set of U(VI) sorption data (CO_2- and Ca-free system) was used for the fitting of model parameters. The model was then applied to *predict* uranium sorption behavior at all other experimental conditions varying in CO_2 and calcium concentrations. A slight underprediction of U(VI) sorption was noted in the presence of CO_2 and calcium, and a refinement of the model is now in progress.

Furthermore, we designed and built a diffusion cell and clay packing device and demonstrated our ability to perform clay diffusion experiments over extended time-frames (4 ½ months). In the first diffusion experiment, we determined diffusion coefficients and sorption parameters for Ca, an important element driving U(VI) solution speciation, and Br at pH 7 and an ionic strength of 0.1 M NaCl.

With respect to uranium(VI) diffusion, we have simulated U(VI) diffusion profiles and relative U(VI) solution concentrations in lab-scale experiments in predictive calculations using the code ANADIFF. The modeling results facilitate the selection of appropriate chemical solution conditions in U(VI) diffusion experiments. Experimental U(VI) diffusion studies are currently ongoing.

Ultimately, all of these efforts will lead to a decrease in uncertainties in reactive transport models describing uranium diffusion in engineered barrier systems and clay formations.

5. OVERALL SUMMARY

Bentonite and bentonite-sand mixtures have been found to have favorable properties for use as a backfill/buffer material for nuclear waste repositories. This report focuses on analyses of bentonite as a component of the EBS. Specific analyses presented here highlight progress made in areas of THMC coupled processes models, reactive transport models, and reactive transport experiments for bentonite. These research activities address key Features, Events and Processes (FEPs) with rankings from medium to high, as listed in Tables 7 and 8 of *Used Fuel Disposition Campaign Disposal Research and Development Roadmap* (FCR&D-USED-2011-000065 REV0) (Nutt, 2011).

5.1 THMC Process Modeling in Bentonite

We are developing and applying coupled THMC models for the analysis of EBS coupled processes in bentonite-backfilled repositories. This activity addresses FEPs 2.1.04.01, Buffer/Backfill; FEPs 2.1.07.02, 03, 04, 09, Mechanical Processes; FEPs 2.1.08.03, 07, 08, Hydrologic Processes; and FEP 2.1.11.04, Thermal Processes, by studying coupled processes in the EBS. Our FY13 accomplishments for this activity include:

- Implementing and testing a dual-structure model for expansive clay (Barcelona Expansive Model (BExM)) into TOUGH-FLAC.

- Linking BExM to the concentration of exchangeable cations through TOUGHREACT-FLAC coupling and demonstrating the capability of modeling the effect of exchangeable cation on the swelling of clay through a generic case.

In the remaining months of FY13, we will

- Improve the numerical stability of the BExM in TOUGH-FLAC and further test it with more comprehensive examples.
- Validate the link of BExM to the concentration of exchangeable cations with published laboratory test.
- Initiate work on more rigorous approach to link chemistry to mechanics through using double-layer theory and BExM dual structure framework (see item 1 in FY14)

For FY14, we propose to

- Work on a more rigorous approach to link chemistry to mechanics through the micro-structure strain. Currently this model is only linked to exchangeable cations as suggested by Gens (2010). However, it is known that chemistry can affect mechanical behavior in clay through the change in pore water salinity, abundance of swelling clay and exchangeable cations. Next step is to develop more comprehensive links between chemistry and mechanics taking advantage of the framework provided by a dual-structure model implemented in TOUGHREACT-FLAC.
- Testing of double-structure THMC model using existing laboratory data, such as swelling pressure vs salinity, swelling pressure vs abundance of swelling clays (sand/bentonite mixtures ratio vs swelling pressure), Swelling pressure vs exchangeable cations
- Application of double-structure THMC model for mechanistic modeling of long-term bentonite-buffer stability in a generic repository emplacement tunnel
- Develop MC coupling relation to describe effects of cementation on mechanical properties of bentonite (transition from plastic to brittle)

5.2 Modeling Reactive-Diffusive Transport in Bentonite

The focus of this activity has been on developing rigorous and yet practically useful approaches to modeling diffusive process in bentonite. This activity addresses Features, Events and Processes (FEPs), FEPs 2.1.04.01, Buffer/Backfill; and FEPs 2.1.09.52, 53, 54, Chemical Processes—Transport by investigating reactive-diffusive radionuclide transport in bentonite. Our FY13 accomplishments include:

- Use of a new capability for a dynamic electrical double layer (EDL) thickness to simulate the effects of the diffusive propagation of a ionic strength front on EDL porosity and transport.
- Implementation of the Mean Electrostatic Model for the EDL with and without Stern layer sorption.
- Use of our ionic strength dependent EDL model to simulate anion and uncharged species out-diffusion from a borehole in the DR-A experiment at the Mont Terri experimental facility in Switzerland, with a single model capturing the behavior of both charged and uncharged species.
- Completion of most of the necessary software changes needed to couple the reaction portion of CrunchEDL with the general purpose PDE simulator Comsol.
- Development of a robust MD simulation methodology that correctly predicts the temperature dependence of Na^+ and water diffusion in bulk liquid water and in the interlayer nanopores of hydrated montmorillonite for a range of dry bulk densities.

- Demonstration that MD simulations can help to extrapolate existing diffusion measurements to the high temperatures that occur in the near-field of high-level radioactive waste repositories while also providing molecular scale insights into the predominant diffusion pathways of water and solutes in the EBS.

In the remaining months of FY13 and during FY14, we will:

- Simulate the Davis-Tinnacher Ca^{2+} and Mg^{2+} diffusion experiments (Section 4)using CrunchEDL, with consideration of both planar and edge site sorption and EDL effects.
- Calculate the swelling pressure and osmotic efficiency of compacted clays in the case of overlapping double layers using a full numerical treatment of the Mean Electrostatic Potential model. This will remove the requirement of treating only symmetric electrolytes.
- Implement a full multicomponent treatment of the Poisson-Boltzmann equation in 1D and 2D. The key challenge will be to accommodate the various sub-zones shown in Figure 3.1 as well as the case of overlapping EDLs (Figure 3.2).
- Continue the work to couple Comsol and CrunchEDL. This will allow us to simulate non-Darcian flow at low flow velocities and as affected by electrostatic effects, in addition to making it possible to carry out pore scale flow and transport simulations.
- Complete our investigations of the *T*-dependence of diffusion for a different type of smectite (Kunipia-F), different types of ions (Cs^+, Sr^{2+}, Ca^{2+}, UO_2^{2+}, and Cl^-), and different populations of background cations (Na-, Ca-, or mixed Na/Ca-smectite). Our simulations of Ca^{2+} and UO_2^{2+} diffusion will inform the analysis of the Davis-Tinnacher diffusion experiments (Section 4).
- Carry out MD simulations of the smallest osmotic hydrate of Na-montmorillonite for a range of ionic strengths (0 to 0.4 M NaCl) in order to benchmark our Mean Electrostatic and Poisson-Boltzmann models of EDL phenomena (Section 3.1).

Develop a MD simulation methodology for predicting the swelling pressure of Na-montmorillonite as a function of pore size and solution chemistry.

5.3 Experimental Study on Reactive-Diffusive Transport

The major objective of this activity is to develop an improved understanding of radionuclide transport mechanisms and providing data sets for more accurately modeling the transport process in bentonite. This activity addresses Features, Events and Processes (FEPs), FEPs 2.1.04.01, Buffer/Backfill; and FEPs 2.1.09.52, 53, 54, Chemical Processes—Transport by investigating reactive-diffusive radionuclide transport in bentonite. In current models for radionuclide diffusion through bentonite in an engineered barrier, the apparent and effective diffusion coefficients are linked through the K_d value, which is often believed to be a constant value for a particular radionuclide. In the case of U(VI), this is less likely to be true, because of the very high sensitivity of the K_d value to pH, as well as bicarbonate and calcium concentrations. Our FY13 accomplishments for this activity include:

- Generated data sets of K_d values for uranium(VI) sorption onto Na-montmorillonite as a function of pH, TIC, and Ca concentrations.
- Developed a surface complexation model to describe the dependence of K_d values on chemical solution conditions.
- Published and presented a proceedings paper at the International High-Level Radioactive Waste Management Conference 2013 (Tinnacher and Davis, 2013), focusing on
    - Chemical solution effects on U(VI) diffusion coefficients and clay (surface) properties, and a

  - Simulation of uranium(VI) diffusion as a function of pH and TIC concentrations in lab-scale experiments.

- Designed and built a diffusion cell and clay packing device.
- Purified standardized montmorillonite (SWy-2) to minimize Ca release and to control chemical solution conditions in later diffusion experiments.
- Performed a calcium bromide diffusion experiment (1 mM $CaBr_2$, 0.1 M NaCl, pH~7) in pretreated Na-montmorillonite, and determined Ca and Br diffusion coefficients (total experimental time frame: 4.5 months). Uranium(VI) diffusion experiments are ongoing.

In the remaining months of FY13, we will:

- Organize the allocation of a heat-treated clay or bentonite sample from Florie Caporuscio's research group at Los Alamos National Laboratory (LANL).
- Further extend the data set for uranium(VI)-Na-montmorillonite K_d values to include varying chemical solution conditions (e.g., Ca and CO_2(g) concentrations, ionic strength), and if already available, heat-treated clay or bentonite samples from LANL.
- Refine the surface complexation model accordingly.
- Continue uranium(VI) diffusion studies in Na-montmorillonite at varying chemical solution conditions.

For FY14, we propose to:

- Conduct uranium(VI) equilibrium sorption experiments with heat-treated clay or bentonite samples, when they become available.
- Conduct uranium(VI) diffusion experiments as a function of chemical solution conditions and, when available, with heat-treated clay or bentonite.
- Perform an analysis and comparison of uranium(VI) diffusion in pure montmorillonite and bentonite.
- Publish a journal paper on U(VI) sorption onto Na-montmorillonite: experimental results and surface complexation modeling.
- Publish a journal article on analysis of Ca and Br diffusion coefficients in montmorillonite.
- Publish a review-type journal paper on the effects of chemical solution conditions on U(VI) diffusion coefficients and clay (surface) properties.

6. ACKNOWLEDGMENT

Funding for this work was provided by the Used Fuel Disposition Campaign, Office of Nuclear Energy, of the U.S. Department of Energy under Contract Number DE-AC02-05CH11231 with Berkeley Lab.

7. REFERENCES

Alonso, E.E., Vaunat, J., Gens, A. Modelling the mechanical behavior of expansive clays. Engineering Geology, 54, 173-183 (1999).

Appelo C.A.J., Vinsot A., Mettler S., Wechner S. Obtaining the porewater composition of a clay rock by modeling the in- and out-diffusion of anions and cations from an in-situ experiment. J. Contam. Hydrol., 101, 67-76 (2008).

Appelo C.A.J., Wersin P. Multicomponent diffusion modeling in clay systems with application to the diffusion of tritium, iodide, and sodium in Opalinus Clay. Environ. Sci. Technol., 41, 5002-5007 (2007).

Arai, Y., McBeath, M., Bargar, J.R., Joye, J., and Davis, J.A., Uranyl adsorption and surface speciation at the imogolite-water interface: Self-consistent spectroscopic and surface complexation models, Geochimica et Cosmochimica Acta, 2006, 70, 2492-2509.

Bai, J.; Liu, C. X.; Ball, W. P., Study of Sorption-Retarded U(VI) Diffusion in Hanford Silt/Clay Material. Environ. Sci. Technol. 2009, 43, (20), 7706-7711.

Berendsen H.J.C., Grigera J.R., Straatsma T.P. The missing term in effective pair potentials. J. Phys. Chem., 91, 6269-6271 (1987).

Bickmore B.R., Rosso K.M., Nagy K.L., Cygan R.T., Tadanier C.J. Ab initio determination of edge surface structures for dioctahedral 2:1 phyllosilicates: Implications for acid-base reactivity. Clays Clay Miner., 51, 359-371 (2003).

Birgersson M., Karnland O. Ion equilibrium between montmorillonite interlayer space and an external solution - Consequences for diffusional transport. Geochim. Cosmochim. Acta, 73, 1908-1923 (2009).

Botan A., Rotenberg B., Marry V., Turq P., Noetinger B. Hydrodynamics in clay nanopores. J. Phys. Chem. C, 115, 16109-16115 (2011).

Bourg I.C., Sposito G. Connecting the molecular scale to the continuum scale for diffusion processes in smectite-rich porous media. Environ. Sci. Technol., 44, 2085-2091 (2010).

Bourg I.C., Sposito G. Ion exchange phenomena. In: Handbook of Soil Science, 2nd ed., Sumner M.E., ed., CRC Press, Boca Raton, FL, Chap. 6 (2011a).

Bourg I.C., Sposito G. Molecular dynamics simulations of the electrical double layer on smectite surfaces contacting concentrated mixed electrolyte (NaCl-CaCl2) solutions. J. Colloid Interface Sci., 360, 701-715 (2011b).

Bourg I.C., Sposito G., Bourg A.C.M. Modeling the diffusion of Na+ in compacted water-saturated Na-bentonite as a function of pore water ionic strength. Appl. Geochem., 23, 3635-3641 (2008).

Bourg, I. C.; Bourg, A. C. M.; Sposito, G., Modeling diffusion and adsorption in compacted bentonite: a critical review. J. Contam. Hydrol. 2003, 61, (1-4), 293-302.

Bourg, I. C.; Sposito, G.; Bourg, A. C. M., Modeling cation diffusion in compacted water-saturated sodium bentonite at low ionic strength. Environ. Sci. Technol. 2007, 41, (23), 8118-8122.

Bourg, I. C.; Sposito, G.; Bourg, A. C. M., Tracer diffusion in compacted, water-saturated bentonite. Clay Clay Min. 2006, 54, (3), 363-374.

Bradbury, M. H.; Baeyens, B., Predictive sorption modelling of Ni(II), Co(II), Eu(IIII), Th(IV) and U(VI) on MX-80 bentonite and Opalinus Clay: A "bottom-up" approach. Appl. Clay Sci. 2011, 52, (1-2), 27-33.

Brown, P. L.; Haworth, A.; Sharland, S. M.; Tweed, C. J., Modeling studies of the sorption of radionuclides in the far field of a nuclear waste repository. Radiochim. Acta 1991, 52-3, 439-443.

Cebula D.J., Thomas R.K., Middleton S., Ottewill R.H., White J.W. Neutron diffraction from clay-water systems. Clays Clay Miner., 27, 39-52 (1979).

Chen T., Smit B., Bell A.T. Are pressure fluctuation-based equilibrium methods really worse than nonequilibrium methods for calculating viscosities? J. Chem. Phys., 131, 246101 (2009).

Chipera, S.J., D.L. Bish, Baseline studies of the Clay Minerals Society source clays: Powder X-ray diffraction analysis, Clays and Clay Minerals, 49, 398-409 (2001).

Churakov S.V., Gimmi T. Up-scaling of molecular diffusion coefficients in clays: A two-step approach. J. Phys. Chem. C, 115, 6703-6714 (2011).

Costanzo, P.A., S. Guggenheim, Baseline studies of the Clay Minerals Society source clays: Preface, Clays and Clay Minerals, 49, 371-371 (2001).

Crank, J., The Mathematics of Diffusion. Oxford Univ. Press, Oxford, 1975.

Cussler, E. L., Diffusion, mass transfer in fluid systems. 2nd ed.; Cambridge University Press: Cambridge, UK, 1997.

Cygan R.T., Liang J.J., Kalinichev A.G. Molecular models of hydroxide, oxyhydroxide, and clay phases and the development of a general force field. J. Phys. Chem. B, 108, 1255-1266 (2004).

Davis, J. A.; Meece, D. E.; Kohler, M.; Curtis, G. P., Approaches to surface complexation modeling of uranium(VI) adsorption on aquifer sediments. Geochim. Cosmochim. Acta 2004, 68, (18), 3621-3641.

Di Maio, C.. Exposure of bentonite to salt solution: osmotic and mechanical effects. Ge´otechnique 46, No. 4, 695-707, (1996).

Dong, W. M.; Brooks, S. C., Formation of aqueous MgUO2(CO3)32- complex and uranium anion exchange mechanism onto an exchange resin. Environmental Science & Technology 2008, 42, (6), 1979-1983.

Duc, M., Gaboriaud, F., and Thomas, F., Sensitivity of the acid-base properties of clays to the methods of preparation and measurement. 2. Evidence from continuous potentiometric titrations, J. Colloid Interface Sci., 2005, 289, 148-156.

Dzombak D.A., Morel F.M.M. Surface Complexation Modeling: Hydrous Ferric Oxide. J.W. Wiley, 416 p. (1990).

engineering. Geotechnique, 60, 3-74 (2010).

Eriksen, T. E.; Jansson, M. Diffusion of I-, Cs+ and Sr2+ in compacted bentonite - Anion exclusion and surface diffusion, SKB Technical Report 96-16; Royal Institute of Technology, Stockholm: 1996.

Eriksen, T. E.; Jansson, M.; Molera, M., Sorption effects on cation diffusion in compacted bentonite. Eng. Geol. 1999, 54, (1-2), 231-236.

Fernández, A., Cuevas, J., Rivas, P. Pore water chemistry of the FEBEX bentonite. Mat. Res. Soc. Symp. Proc. 663, 573-588, (2001).

Ferrage E., Lanson B., Sakharov B.A., Geoffroy N., Jacquot E., Drits V.A. Investigation of dioctahedral smectite hydration properties by modeling of X-ray diffraction profiles: Influence of layer charge and charge location. Amer. Mineral., 92, 1731-1743 (2007).

Ferrage E., Sakharov B.A., Michot L.J., Delville A., Bauer A., Lanson B., Grangeon S., Frapper G., Jimenez-Ruiz M., Cuello G.J. Hydration properties and interlayer organization of water and ions in synthetic Na-smectite with tetrahedral layer charge. Part 2. Toward a precise coupling between molecular simulations and diffraction data. J. Phys. Chem. C, 115, 1867-1881 (2011).

Foster W.R., Savins J.G., Waite J.M. Lattice expansion and rheological behavior relationships in water-montmorillonite systems. Clays Clay Miner., 3, 296-316 (1955).

Fox, P. M.; Davis, J. A.; Zachara, J. M., The effect of calcium on aqueous uranium(VI) speciation and adsorption to ferrihydrite and quartz. Geochim. Cosmochim. Acta 2006, 70, (6), 1379-1387.

Gens A. Soil - environmental interactions in geotechnical engineering. Geotechnique, 60, 3-74 (2010).

Gens, A, Alonso, E. A framework for the behaviour of unsaturated expansive clays. Can. Geotech. J. 29, 1013-1032 (1992).

Gens, A., Sánchez, M., Sheng, D. On constitutive modelling of unsaturated soils. Acta Geotechnica, 1, 137-147 (2006).

Glaus M.A., Frick S., Rossé R., van Loon L.R. Consistent interpretation of the results of through-, out-diffusion and tracer profile analysis for trace anion diffusion in compacted montmorillonite. J. Contam. Hydrol., 123, 1-10 (2011).

Glaus, M. A.; Rosse, R.; Van Loon, L. R.; Yaroshchuk, A. E., Tracer diffusion in sintered stainless steel filters: measurement of effective diffusion coefficients and implications for diffusion studies with compacted clays. Clay Clay Min. 2008, 56, (6), 677-685.

Gonçalvès J., Rousseau-Gueutin P., Revil A. Introducing interacting diffuse layers in TLM calculations: A reappraisal of the influence of the pore size on the swelling pressure and the osmotic efficiency of compacted bentonites. J. Colloid Interface Sci., 316, 92-99 (2007).

González Sánchez F., Gimmi T., Jurányi F., Van Loon L., Diamond L.W. Linking the diffusion of water in compacted clays at two different time scales: Tracer through-diffusion and quasielastic neutron scattering. Environ. Sci. Technol., 43, 3487-3493 (2009).

Greathouse J.A., Feller S.E., McQuarrie D.A. The modified Gouy-Chapman theory: Comparisons between electrical double layer models of clay swelling. Langmuir, 10, 2125-2130.

Guillaumont, R.; Fanghanel, T.; Fuger, J.; Grenthe, I.; Neck, V.; Palmer, D. A.; Rand, M. H., Update on the Chemical Thermodynamics of Uranium, Neptunium, Plutonium, Americium and Technetium. Elsevier: Amsterdam, 2003; Vol. 5.

Guimarães L.D.N., Gens A., Sánchez M., Olivella S. A chemo-mechanical constitutive model accounting for cation exchange in expansive clays. Geotechnique, 63, 221-234 (2013).

Herbelin, A. L. and Westall, J.C., FITEQL: A Computer Program for the Determination of Chemical Equilibrium Constants from Experimental Data, Version 4.0, Report 99-01, 1999, Chemistry Department, Oregon State University, Corvallis, Oregon.

Holmboe M., Jonsson M., Wold S. Porosity investigation of compacted bentonite using XRD profile modeling. J. Contam. Hydrol., 128, 19-32 (2012).

Holmboe M., Norrfors K., Jonsson M., Wold S. Effect of -radiation on radionuclide retention in compacted bentonite. Radiat. Phys. Chem., 80, 1371-1377 (2011).

Holmboe, M. The bentonite barrier: Microstructural aspects on colloid filtration and radiation effects on bentonite colloid stability. KTH, Royal Institute of Technology, Stockholm, 2009.

Holz M., Heil S.R., Sacco A. Temperature-dependent self-diffusion coefficients of water and six selected molecular liquids for calibration in accurate 1H NMR PFG measurements. Phys. Chem. Chem. Phys., 2, 4740-4742 (2000).

Hsi, C.K.D., D. Langmuir, Adsorption of uranyl onto ferric oxyhydroxides: Application of the surface complexation site-binding model. Geochim. Cosmochim. Acta 1985, 49, 1931-1941.

Ichikawa Y., Kawamura K., Fujii N., Kitayama K. Microstructure and micro/macro-diffusion behavior of tritium in bentonite. Appl. Clay Sci., 26, 75-90 (2004).

Jakob, A., Sarott, F.A., Spieler, P., 1999. Diffusion and Sorption on Hardened Cement Pastes. Experiments and Modelling Results. Paul Scherrer Institut Report 99-05.

JNC (Japanese Nuclear Cycle Development Institute) H12 project to establish the scientific and technical basis for HLW disposal in Japan. JNC Technical Report JNC TN1410 2000-001 (2000).

Joung I.S., Cheatham T.E., III. Determination of alkali and halide monovalent ion parameters for use in explicitly solvated biomolecular simulations. J. Phys. Chem. B, 112, 9020-9041 (2008).

Kalinichev A.G.K., Kirkpatrick R.J.K., Cygan R.T. Molecular modeling of the structure and dynamics of the interlayer and surface species of mixed-metal layered hydroxides: Chloride and water in hydrocalumite (Friedel's salt). Amer. Mineral., 85, 1046-1052 (2000).

Kerisit, S.; Liu, C. X., Molecular simulation of the diffusion of uranyl carbonate species in aqueous solution. Geochim. Cosmochim. Acta 2010, 74, (17), 4937-4952.

Kerisit, S.; Liu, C., Molecular Simulations of Water and Ion Diffusion in Nanosized Mineral Fractures. Environ. Sci. Technol. 2009, 43, (3), 777-782.

Kim, H.-T.; Suk, T.-W.; Park, S.-H.; Lee, C.-S., Diffusivities for ions through compacted Na-bentonite with varying dry bulk density. Waste Manage. 1993, 13, (4), 303-308.

Korichi, S.; Bensmaili, A.; Keddam, M., Reactive diffusion of uranium in compacted clay: Evaluation of diffusion coefficients by a kinetic approach. Defect Diff. Forum 2010, 297-301, 275-280.

Kosakowski G., Churakov S.V., Thoenen T. Diffusion of Na and Cs in montmorillonite. Clays Clay Miner., 56, 190-206 (2008).

Kozaki T., Fujishima A., Saito N., Sato S., Ohashi H. Effects of dry density and exchangeable cations on the diffusion process of sodium ions in compacted montmorillonite. Eng. Geol., 81, 246-254 (2005).

Kozaki T., Fujishima A., Sato S., Ohashi H. Self-diffusion of sodium ions in compacted sodium montmorillonite. Nucl. Technol., 121, 63-69 (1998).

Kozaki T., Inada K., Sato S., Ohashi H. Diffusion mechanism of chloride ions in sodium montmorillonite. J. Contam. Hydrol., 47, 159-170 (2001).

Kozaki T., Liu J., Sato S. Diffusion mechanism of sodium ions in compacted montmorillonite under different NaCl concentration. Phys. Chem. Earth A/B/C, 33, 957-961 (2008).

Kozaki T., Sato H., Fujishima A., Saito N., Sato S., Ohashi H. Effect of dry density on activation energy for diffusion of strontium in compacted sodium montmorillonite. Mat. Res. Soc. Symp. Proc., 465, 893-900 (1997).

Kozaki T., Sato H., Fujishima A., Sato S., Ohashi H. Activation energy for diffusion of cesium in compacted sodium montmorillonite. J. Nucl. Sci. Technol., 33, 522-524 (1996).

Kozaki T., Sato H., Sato S., Ohashi H. Diffusion mechanism of cesium ions in compacted montmorillonite. Eng. Geol., 54, 223-240 (1999).

Kozaki T., Sawaguchi T., Fujishima A., Sato S. Effect of exchangeable cations on apparent diffusion of Ca2+ ions in Na- and Ca-montmorillonite mixtures. Phys. Chem. Earth A/B/C, 35, 254-258 (2010).

Kozaki, T.; Adachi, Y.; Inada, K.; Sato, S.; Ohashi, H. Diffusion behavior of Ca2+ ions in compacted Na-montmorillonite. In: Scientific Basis for Nuclear Waste Management XXIV. Symposium, Sydney, NSW, Australia, 27-31 Aug. 2000 (Materials Research Society Proceedings Vol.663). Hart, K.P.; Lumpkin, G.R. (eds). p. 629-635, 2001.

Leroy P., Revil A. A triple-layer model of the surface electrochemical properties of clay minerals. J. Colloid Interface Sci., 270, 371-380 (2004).

Leroy P., Revil A., Altmann S., Tournassat C. Modeling the composition of a pore water in a clay-rock geological formation (Callovo-Oxfordian, France). Geochim. Cosmochim. Acta, 71, 1087-1097 (2007).

Leroy, P.; Revil, A.; Coelho, D., Diffusion of ionic species in bentonite. J. Colloid Interf. Sci. 2006, 296, (1), 248-255.

Lide D.R. CRC Handbook of Chemistry and Physics. CRC Press (2012).

Liu J., Kozaki T., Horiuchi Y., Sato S. Microstructure of montmorillonite/silica sand mixture and its effects on the diffusion of strontium ions. Appl. Clay Sci., 23, 89-95 (2003).

Liu, C.; Zhong, L.; Zachara, J. M., Uranium(VI) diffusion in low-permeability subsurface materials. Radiochim. Acta 2010, 98, (9-11), 719-726.

Madsen, F. T., Clay mineralogical investigations related to nuclear waste disposal. Clay Min. 1998, 33, (1), 109-129.

Maes, N.; Moors, H.; Wang, L.; Delecaut, G.; De Canniere, P.; Put, M., The use of electromigration as a qualitative technique to study the migration behaviour and speciation of uranium in the Boom Clay. Radiochim. Acta 2002, 90, (9-11), 741-746.

Malikova N., Cadéne A., Marry V., Dubois E., Turq P., Zanotti J.-M., Longeville S. Diffusion of water in clays - Microscopic simulation and neutron scattering. Chem. Phys., 317, 226-235 (2005).

Malikova N., Marry V., Dufrêche J.-F., Simon C., Turq P., Giffaut E. Temperature effect in a montmorillonite clay at low hydration-microscopic simulation. Mol. Phys., 102, 1965-1977 (2004a).

Malikova N., Marry V., Dufrêche J.-F., Turq P. Na/Cs montmorillonite: Temperature activation of diffusion by simulation. Curr. Opin. Colloid Interface Sci., 9, 124-127 (2004b).

Malusis M.A., Shackelford C.D. Explicit and implicit coupling during solute transport through clay membrane barriers. J. Contam. Hydrol., 72, 259-285 (2004).

Malusis M.A., Shackelford C.D., Olsen H.W. Flow and transport through clay membrane barriers. Eng. Geol., 70, 235-248 (2003).

Mammar N., Rosanne M., Prunet-Foch B., Thovert J.-F., Tevissen E., Adler P.M. Transport properties of compact clays. I. Conductivity and permeability. J. Colloid Interface Sci., 240, 498-508 (2001).

Marry V., Dubois E., Malikova N., Durand-Vidal S., Longeville S., Breu J. Water dynamics in hectorite clays: Influence of temperature studied by coupling neutron spin echo and molecular dynamics. Environ. Sci. Technol., 45, 2850-2855 (2011).

Marry V., Rotenberg B., Turq P. Structure and dynamics of water at a clay surface from molecular dynamics simulation. Phys. Chem. Chem. Phys., 10, 4802-4813 (2008).

Marry V., Turq P. Microscopic simulations of interlayer structure and dynamics in bihydrated heteroionic montmorillonites. J. Phys. Chem. B, 107, 1832-1839 (2003).

Mazo M.A., Manevitch L.I., Gusarova E.B., Berlin A.A., Balabaev N.K., Rutledge G.C. Molecular dynamics simulation of thermomechanical properties of montmorillonite crystal. II. Hydrated montmorillonite crystal. J. Phys. Chem. C, 112, 17056-17062 (2008).

Mazzieri, F.; Di Emidio, G.; Van Impe, P.O., (Van Impe, Peter O.), Diffusion of Calcium Chloride in a Modified Bentonite: Impact on Osmotic Efficiency and Hydraulic Conductivity, Clays and Clay Minerals, 58, 351-363 (2010).

McKinley, J.P., Zachara, J.M., Smith, S.C., and Turner, G.D., The influence of uranyl hydrolysis and multiple site-binding reactions on adsorption of U(VI) to montmorillonite, Clays Clay. Min., 1995, 43, 586-598.

Medina J.S., Prosmiti R., Villarreal P., Delgado-Barrio G., Winter G., Gonzalez B., Aleman J.V., Collado C. Molecular dynamics simulations of rigid and flexible water model: Temperature dependence of viscosity. Chem. Phys., 388, 9-18 (2011).

Melkior T., Gaucher E.C., Brouard C., Yahiaoui S., Thoby D., Clinard C., Ferrage E., Guyonnet D., Tournassat C., Coelho D. Na+ and HTO diffusion in compacted bentonite: effect of surface chemistry and related texture. J. Hydrol., 370, 9-20 (2009).

Mermut, A.R., A.F. Cano, Baseline studies of the Clay Minerals Society source clays: Layer-charge determination and characteristics of those minerals containing 2:1 layers, Clays and Clay Minerals, 49, 393-397 (2001).

Mitchell, J. K. & Soga, K. (2005). Fundamentals of soil behaviour, 3rd edn. Hoboken, NJ, USA: Wiley.

Molera M., Eriksen T. Diffusion of 22Na+, 85Sr2+, 134Cs+ and 57Co2+ in bentonite clay compacted to different densities: Experiments and modeling. Radiochim. Acta, 90, 753-760 (2002).

Molera M., Eriksen T., Jansson M. Anion diffusion pathways in bentonite clay compacted to different dry densities. Appl. Clay Sci., 23, 69-76 (2003).

Muurinen, A., Diffusion of uranium in compacted sodium bentonite. Eng. Geol. 1990, 28, (3-4), 359-367.

Nakashima T. Diffusivity measurement of heavy ions in Wyoming montmorillonite gels by X-ray computed tomography. J. Contam. Hydrol., 61, 147-156 (2003).

Nakazawa T., Takano M., Nobuhara A., Torikai Y., Sato S., Ohashi H. Activation energies of diffusion of tritium and electrical conduction. Radioact. Waste Manag. Environ. Rem., 1999, 8-12 (1999).

Norrish K. The swelling of montmorillonite. Disc. Faraday Soc. 18, 120 (1954).

Nutt, M., Used Fuel Disposition Campaign Disposal Research and Development Roadmap (FCR&D-USED-2011-000065 REV0), U.S. DOE Used Fuel Disposition Campaign, 2011.

Ochs, M.; Lothenbach, B.; Wanner, H.; Sato, H.; Yui, M., An integrated sorption-diffusion model for the calculation of consistent distribution and diffusion coefficients in compacted bentonite. J. Contam. Hydrol. 2001, 47, (2-4), 283-296.

OECD, Engineering barrier systems and the safety of deep geological repositories (State-of-the-art Report), ISBN 92-64-18498-8, 2003.

Parsegian V.A. Van der Waals forces: a handbook for biologists, chemists, engineers, and physicists. Cambridge University Press (2006).

Pitman M.C., van Duin A.C.T. Dynamics of confined reactive water in smectite clay-zeolite composites. J. Am. Chem. Soc., 134, 3042-3053 (2012).

Placzek G., Nijboer B., Hove L. Effect of short wavelength interferences on neutron scattering by dense systems of heavy nuclei. Phys. Rev., 82, 392-403 (1951).

Plimpton S. Fast parallel algorithms for short-range molecular dynamics. J. Comput. Phys., 117, 1-42 (1995).

Pousada, P.E. Deformabilidad de arcillas expansivas bajo succión controlada. Ph. D. Thesis, Technical University of Madrid, Spain (1984).

Pusch, R., Use of bentonite for isolation of radioactive-waste products. Clay Min. 1992, 27, (3), 353-361.

Rotenberg B., Marry V., Vuilleumier R., Malikova N., Simon C., Turq P. Water and ions in clays: Unraveling the interlayer/micropore exchange using molecular dynamics. Geochim. Cosmochim. Acta, 71, 5089-5101 (2007a).

Rotenberg B., Marry V., Dufrêche J.-F., Malikova N., Giffaut E., Turq P. Modelling water and ion diffusion in clays: A multiscale approach. C.R. Chim., 10, 1108-1116 (2007b).

Rutqvist, J., Ijiri, Y. Yamamoto, H. Implementation of the Barcelona Basic Model into TOUGH-FLAC for simulations of the geomechanical behavior of unsaturated soils. Computers & Geosciences, 37, 751-762 (2011).

Rutqvist, J., Steefel, C., Davis, J., Bourg, I., Tinnacher, R., Galindez, J., Holmboe, M., Birkholzer, J., Liu, H.H. Investigation of Reactive Transport and Coupled THM Processes in EBS: FY12 Report, Lawrence Berkeley National Laboratory, DOE Used Fuel Disposition Campaign, FCRD-UFD-2012-000125. (2012).

Rutqvist, J., Zheng, L., Chen, F., Liu, H.-H., Birkholzer, J. Modeling of Coupled Thermo-Hydro-Mechanical Processes with Links to Geochemistry Associated with Bentonite-Backfilled Repository Tunnels in Clay Formations. Rock Mechanics and Rock Engineering, (In Press, January 2013).

Ryckaert J.-P., Ciccotti G., Berendsen H.J.C. Numerical integration of the Cartesian equations of motion of a system with constraints: Molecular dynamics of n-alkanes. J. Comput. Phys., 23, 327-341 (1977).

Safran S.A. Statistical thermodynamics of surfaces, interfaces, and membranes. Addison-Wesley, Reading, MA (1994).

Saiyouri N., Tessier D., Hicher P.Y.Y. Experimental study of swelling in unsaturated compacted clays. Clay Miner., 39, 469-479 (2004).

Sánchez, M., Gens, A., Guimarães, L. do N., Olivella, S. A double structure generalized plasticity model for expansive materials. Int. J. Numer. Anal. Meth. Geomech., 29, 751-787. (2005).

Sato H. Fundamental study on the effect of an orientation of clay particles on diffusion pathway in compacted bentonite. Appl. Clay Sci., 23, 51-60 (2003).

Schoch R.B., Han J., Renaud P. Transport phenomena in nanofluidics. Rev. Mod. Phys., 80, 840-883 (2008).

Selim, H. M.; Amacher, M. C., Reactivity and transport of heavy metals in soils. CRC Press, Inc.: Boca Raton, 1997; p 201.

Shackelford, C. D., Laboratory diffusion testing for waste disposal - a review. J. Contam. Hydrol. 1991, 7, (3), 177-218.

Shackelford, C. D.; Daniel, D. E., Diffusion in saturated soil. I: Background. J. Geotech. Eng.-ASCE 1991, 117, (3), 467-484.

Shackelford, C. D.; Lee, J.-M., The destructive role of diffusion on clay membrane behavior. Clays and Clay Minerals, 51, 186-196 (2003).

SKB (Swedish Nuclear Fuel and Waste Management Co) Thermal dimensioning of the deep repository. SKB Technical Report TR-03-09 (2009).

Skipper N.T., Chang F.-R.C., Sposito G. Monte Carlo simulation of interlayer molecular structure in swelling clay minerals. 1. Methodology. Clays Clay Miner., 43, 285-293 (1995).

Skipper N.T., Refson K., McConnell J.D.C. Computer simulation of interlayer water in 2:1 clays. J. Chem. Phys., 94, 7434-7445 (1991).

Sposito G., Prost R. Structure of water adsorbed on smectites. Chem. Rev., 82, 553-573 (1982).

Sposito G., Skipper N.T., Sutton R., Park S., Soper A.K., Greathouse J.A. Surface geochemistry of the clay minerals. Proc. Natl. Acad. Sci. U.S.A., 96, 3358-3364 (1999).

Stumm, W. Chemistry of the Solid-Water Interface: Processes at the Mineral-Water Particle-Water Interface in Natural Systems, John Wiley & Sons, 428 p., 1992.

Suzuki S., Sato H., Ishidera T., Fujii N. Study on anisotropy of effective diffusion coefficient and activation energy for deuterated water in compacted sodium bentonite. J. Contam. Hydrol., 68, 23-37 (2004).

Svensson P.D., Hansen S. Freezing and thawing of montmorillonite - A time-resolved synchrotron X-ray diffraction study. Appl. Clay Sci., 49, 127-134 (2010).

Tachi Y., Nakazawa T., Ochs M., Yotsuji K., Suyama T., Seida Y., Yamada N., Yui M. Diffusion and sorption of neptunium(V) in compacted montmorillonite: Effects of carbonate and salinity. Radiochim. Acta, 98, 711-718 (2010).

Talekar S.V. Temperature dependence of activation energies for self-diffusion of water and of alkali ions in aqueous electrolyte solutions. Int. J. Quantum Chem. Biol. Symp., 4, 459-469 (1977).

Tanaka S., Noda N., Sato S., Kozaki T., Sato H. Electrokinetic study of migration of anions, cations, and water in water-saturated compacted sodium montmorillonite. J. Nucl. Sci. Technol., 48, 454-462 (2011).

Tazi S., Botan A., Salanne M., Marry V., Turq P. Rotenberg B. Diffusion coefficient and shear viscosity of rigid water models. J. Phys.: Condens. Matter, 24, 284117 (2012).

Teppen B.J., Rasmussen K., Bertsch P.M., Miller D.M., Schaefer L. Molecular dynamics modeling of clay minerals. 1. Gibbiste, kaolinite, pyrophyllite, and beidellite. J. Phys. Chem. B, 101, 1579-1587 (1997).

Tinnacher, R. M., Davis, J. A. Effects of Chemical Solution Conditions on Uranium(VI) Diffusion in Clays, Proceedings to IHLRWM Conference, 2013.

Tokunaga, T. K.; Wan, J. M.; Pena, J.; Sutton, S. R.; Newville, M., Hexavalent uranium diffusion into soils from concentrated acidic and alkaline solutions. Environ. Sci. Technol. 2004, 38, (11), 3056-3062.

Tournassat C., Appelo C.A.J. Modelling approaches for anion-exclusion in compacted Na-bentonite. Geochim. Cosmochim. Acta, 75, 3698-3710 (2011).

Tournassat C., Chapron Y., Leroy P., Bizi M., Boulahya F. Comparison of molecular dynamics simulations with Triple Layer and Modified Gouy-Chapman models in a 0.1 M NaCl-montmorillonite system. J. Colloid Interface Sci., 339, 533-541 (2009).

Van Loon, L. R.; Glaus, M. A.; Mueller, W., Anion exclusion effects in compacted bentonites: Towards a better understanding of anion diffusion. Appl. Geochem. 2007, 22, (11), 2536-2552.

Van Loon, L. R.; Soler, J. M. Diffsion of HTO, 36Cl-, 125I- and 22Na+ in Opalinus Clay: Effect of Confining Pressure, Sample Orientation, Sample Depth and Temperature. Paul Scherrer Institut Report Nr. 04-03, 2004.

Van Loon, L. R.; Soler, J. M.; Bradbury, M. H., Diffusion of HTO, 36Cl- and 125I- in Opalinus Clay samples from Mont Terri - Effect of confining pressure. J. Contam. Hydrol. 2003, 61, (1-4), 73-83.

Vega C. Sanz E., Abascal J.L.F. The melting temperature of the most common models of water. J. Chem. Phys., 122, 114507 (2005).

Wakim, J., F. Hadj-Hassen and L. De Windt 2009. Effect of aqueous solution chemistry on the swelling and shrinkage of the Tournemire shale. International Journal of Rock Mechanics and Mining Sciences 46(8): 1378-1382.

Wang X., Tan X., Chen C., Chen L. The concentration and pH dependent diffusion of 137Cs in compacted bentonite using capillary method. J. Nucl. Mater., 345, 184-191 (2005).

Wersin P., Curti E. Appelo C.A.J. Modelling bentonite-water interactions at high solid/liquid ratios: swelling and diffuse double layer effects. Applied Clay Sci., 26, 249-257 (2004).

Wilson J., Cuadros J., Cressey G. An in situ time-resolved XRD-PSD investigation into Na-montmorillonite interlayer and particle rearrangement during dehydration. Clays Clay Miner., 52, 180-191 (2004).

Yeh I.C., Hummer G. System-size dependence of diffusion coefficients and viscosities from molecular dynamics simulations wither periodic boundary conditions. J. Phys. Chem. B, 108, 15873-15879 (2004a).

Yeh I.C., Hummer G. Diffusion and electrophoretic mobility of single-stranded RNA from molecular dynamics simulations. Biophys. J., 86, 681-689 (2004b).

Zachara, J.M. and Smith, S.C., Edge complexation reactions of cadmium on specimen and soil-derived smectite, Soil Sci. Soc. Amer. J., 1994, 58, 762-769.

Zeebe R.E. On the molecular diffusion coefficients of dissolved CO2, HCO3-, and CO32- and their dependence on isotopic mass. Geochim. Cosmochim. Acta, 75, 2483-2498 (2011).

Zhang Z.Z., Low P.F. Relation between the heat of initial water content of Li-, Na-, and K-montmorillonite. J. Colloid Interface Sci., 133, 461-472 (1989).